ROBUST DESIGN OF A BREAST SCINTIGRAPHY COLLIMATOR USING MONTE CARLO SIMULATIONS AND RESPONSE SURFACE METHODOLOGY

by

Sinem Balta

B.S., Electrical and Electronic Engineeering, Boğaziçi University, 2004

Submitted to Institute of Biomedical Engineering
in partial fulfillment of the requirements
for the degree of
Master of Science
in
Biomedical Engineering

Boğaziçi University
June 2007

ROBUST DESIGN OF BREAST SCINTIGRAPHY COLLIMATOR USING MONTE CARLO SIMULATIONS AND RESPONSE SURFACE METHODOLOGY

APPROVED BY:

Assoc. Prof. Albert GÜVENİŞ .....
(Thesis Supervisor)

Prof. Yorgo ISTEFANOPULOS .....

Prof. Ahmet ADEMOĞLU .....

DATE OF APPROVAL: 12.June.2007

ACKNOWLEDGEMENTS

I would like to thank my thesis supervisor Assoc. Prof. Albert Güveniş for his academic support and guidance during my study. Also, I am very grateful to Prof. Yorgo Istefanopulos for his recommendations. He helped me to find my way.

Very special thanks to Umut Alpay Alp for his invaluable assistance and encouragement throughout this work. I would not be able to accomplish this work without his support.

This study is dedicated to the breast cancer patients.

ABSTRACT

ROBUST DESIGN OF BREAST SCINTIGRAPHY COLLIMATOR USING MONTE CARLO SIMULATIONS AND RESPONSE SURFACE METHODOLOGY

Breast Scintigraphy, a nuclear medicine breast imaging technique, is a supplemental breast exam that is used in patients to investigate a breast abnormality. It is not a primary investigative tool for breast cancer but it is used as a complementary technique in cases where conventional x-ray mammography has some limitations in breast cancer diagnosis. However, studies show that breast scintigraphy does not give successful results when breast abnormality is less than 1cm. The collimator plays an important role in image construction. This study aims to make a robust design of the breast scintigraphy system collimator to obtain a better image quality in small breast lesions (<1cm) by the optimization of the collimator parameters such as hole length (collimator length), hole size and septal thickness while keeping the lesion detectability less susceptible to patient variations such as breast and lesion dimensions. The breast and the lesion were modeled as a cylinder and a sphere, respectively. Monte Carlo Simulation is utilized for simulating the imaging system and Response Surface Methodology is applied for robust optimization. The first part of the study deals with a typical case of breast and lesion dimensions whereas the second part inserts variance to the parameters. Our results show that a hole length of 1.74cm, a hole size of 0.14cm and a septal thickness of 0.02cm are the dimensions of a robust collimator.

Keywords: Breast Scintigraphy, collimator, Monte Carlo Simulation, Response Surface Method, robust design

ÖZET

MONTE CARLO BENZETİMİ VE TEPKİ YÜZEY YÖNTEMİ KULLANILARAK GÜRBÜZ MEME SİNTİGRAFİSİ KOLİMATÖRÜ TASARIMI

Meme sintigrafisi, bir nükleer tıp meme görüntüleme tekniği olup, hastalarda meme anormalliği incelemek amacıyla tamamlayıcı bir meme tetkiki olarak kullanılır. Meme kanseri için öncelikli tetkik yöntemi olmayıp, bilinen röntgen mamografinin meme kanseri tanısında bazı sınırları olan durumlarda yardımcı yöntem olarak kullanılabilir. Ancak, çalışmalar, meme sintigrafisinin meme anormalliğinin 1cm'den küçük olduğu durumlarda başarılı sonuçlar vermediğini göstermektedir. Kolimatör, görüntü oluşturmada önemli bir rol oynar. Bu çalışmanın amacı, 1cm'den küçük meme anormalliklerinde daha iyi bir görüntü kalitesi elde ederken, lezyon farkedilebilirliğini meme ve lezyon değişimlerine daha az hassas tutarak, meme sintigrafi kolimatörünün gürbüz tasarımını yapmaktır. Bu amaç doğrultusunda, sistemin tepkisini eniyileştirecek delik uzunluğu (kolimatör kalınlığı), delik boyu ve septal kalınlıktan oluşan kolimatör parametreleri kümesi bulunmaya çalışılmıştır. Meme ve lezyon sırasıyla bir silindir ve bir küre olarak modellenmiştir. Görüntüleme sisteminin benzetimi için Monte Carlo Benzetimi ve gürbüz eniyileme için Yüzey Tepki Yöntemi kullanılmıştır. Çalışmanın ilk bölümü tipik meme ve lezyon değerleriyle uğraşırken, ikinci bölüm bu değişkenlere değişinti eklemiştir. Sonuçlarımız göstermektedir ki, 1.74cm delik uzunluğu, 0.14cm delik boyu ve 0.02cm septal kalınlık dayanıklı bir kolimatörün boyutlarını vermektedir.

Anahtar Sözcükler: Meme Sintigrafisi, kolimatör, Monte Carlo Benzetimi, Tepki Yüzey Yöntemi, gürbüz tasarım

TABLE OF CONTENTS

LIST OF FIGURES

LIST OF TABLES

LIST OF SYMBOLS

R_s	Overall system resolution
R_i	Inherent spatial (intrinsic) resolution
R_c	Collimator resolution
R_o	Counting rate over normal tissue
R_l	Counting rate over a lesion
C_l	Contrast of the lesion
ΔR_l	Change in counting rate over the lesion
R_b	Uniform background counting rate
A_l	Lesion area
No	The number of counts in a background area
t	Time
d_l	Diameter of the lesion
σ_{No}	Statistical variations of the counts in background areas
C_{noise}	Noise contrast
CNR_l	Contrast-to-noise ratio of lesion
ID_o	Background information density of the image
T(x)	Real valued function
$\langle T \rangle$	Mean value of T(x)
f(x)	Frequency function
N	Number of samples
σ^2	Variance
P(x)	Probability of event x
U	Random Numbers Generator
F(x)	The cumulative distribution function of f(x)
p(x)	The probability density function
d	Distance
R	Uniform random number
w	Weight factor of photon

θ_{max}	Maximum acceptance angle
d_{λ}	The distance to the interaction number of mean free paths
ε	Statistical error
ζ	Input variable
y	Response
β_i	Regression coefficients
x_s	Stationary point
y	Response at the stationary point
E	Mean value
Var	Variance
Cps	Counts per second
Ci	Curie

LIST OF ABBREVIATIONS

SM	Scintimammography
SPECT	Single-Photon Emission-Computed Tomography
NaI(Tl)	Thallium Activated Sodium Iodide
LEHR	Low-Energy-High-Resolution
SNR	Signal-to-Noise Ratio
LEUHS	Low-Energy-Ultra-High-Sensitivity
LEUHR	Low-Energy-Ultra-High-Resolution
RSM	Response Surface Methodology
FNAB	Fine Needle Aspiration Biopsy
MX	Mammography
US	Ultrasonography
MR	Magnetic Resonance
Pgp	P-glycoprotein
MDR	Multi-Drug Resistance
DCIS	Ductal Carcinoma In Situ
MRI	Magnetic Resonance Imaging
PMT	Photomultiplier Tube
PHA	Pulse Height Analyzer
CRT	Cathode Ray Tube
CNR	Contrast-to-Noise Ratio
PDFs	Probability Density Functions
RNG	Random Numbers Generator
LCRNG	Linear Congruential Random Numbers Generator
LFRNG	Lagged Fibonacci Random Numbers Generator
MLCRNG	Multiplicative Linear Congruential Random Numbers Generator
ALFRNG	Additive Lagged-Fibonacci Random Numbers Generator
PET	Positron Emission Tomography
CB	Cone Beam

PH	Parallel Hole
MIRD	Medical Internal Radiation Dose
SG	Simple Geometry
SB	Shape-Based
VB	Voxel-Based
SGB	Solid Geometry-Based
MCAT	The Mathematical Cardiac Torso
RSM	Response Surface Methodology
CCC	Circumscribed Central Composite
CCI	Inscribed Central Composite
CCF	Faced Central Composite
RPD	Robust Parameter Design
DoE	Design of Experiments
ANOVA	Analysis of Variance
POE	Propagation of Error

1. INTRODUCTION

1.1 Background and Motivation

Breast carcinoma is the most common malignancy in women. In USA, it represents 32% of all invasive tumors in the female population, and it is the second leading cause of death for women following lung cancer, accounting for 15% of all cancer deaths. In 2004, the American Cancer Society estimated in the USA 215,990 new cases of breast cancer among women and 40,110 female deaths from this disease [1]. According to the cancer statistics of the Ministry of the Health of Turkey in 1999, 2,390 of 9,919 cancer cases are cases of breast cancer in females. This means 24.1% of female population experiences breast cancer [2]. In Turkey, the mortality of females because of breast cancer has been increased since 1980 and breast cancer has become the second cause of death after lung cancer [3].

Trends in incidence and mortality show that there has been a small but steady annual increase in breast cancer incidence over the last 30 years, whereas the mortality rate declined steadily since the beginning of the nineties [1]. This benefit is attributed to earlier detection of breast cancer by mammographic screening [4].

Mammography is currently the best imaging modality for early identification of breast cancer: its findings are based on anatomic changes in the breast and it is the method of choice in screening asymptomatic women [5] but this technique has some limitations that reduce its sensitivity and specificity. In fact, not all breast carcinomas are evident on mammograms, especially in dense or dysplastic breasts [6]. Moreover, its specificity and positive predictive value are low: the main limitation is that it cannot always differentiate benign lesions from malignant ones [7]. This is especially the case in women with dense breasts, or those who have architectural distortion of their breasts following radiation therapy or surgery, or those with breast implants [6]. Therefore, abnormalities detected

during mammography frequently result in biopsy, and the outcome is that many women without cancer are biopsied [8]. The drawbacks of mammography have led to the development of complementary modalities for breast cancer imaging, including scintimammography [7].

Breast Scintigraphy (Scintimammography) is a nuclear medicine imaging technique that uses radionuclides to image malignant breast tumors; it requires the administration of a single photon emitting radiotracer to the patient and a gamma-camera for imaging. Currently, the most widely used radiotracers for Breast Scintigraphy are ^{99m}Tc-sestamibi and ^{99m}Tc-tetrofosmin.

Scintimammography (SM) is very sensitive and is able to improve the specificity of mammography, thereby being potentially useful in reducing the high rates of negative biopsies performed [4].

Nevertheless, it is of the utmost importance to highlight that the sensitivity of scintimammography is strictly dependent on the size of lesions. In particular, sensitivity was significantly different between malignant lesions ≤1 cm (46.5%) and those >1 cm (96%) [9]. Waxman et al. [10] showed that lesions greater than 12mm are visualized by scintigraphy in more than 92% of cases, whereas smaller tumors are detected only in 50% of cases.

Instrumentation of a breast scintigraphy is a single- or multiple-head gamma camera, which is needed to acquire planar images, and a specially designed imaging table. The energy window for image collection should be 10% (±5%) centered over the 140-keV photopeak of ^{99m}Tc. The gamma camera should be equipped with a low energy, high-resolution collimator [11] which allows the gamma camera to localize accurately the radionuclide in the patient's body. Collimators perform this function by absorbing and stopping most radiation except that arriving almost perpendicular to the detector face [12].

The collimator plays an important role in the resolution and sensitivity of breast scintigraphy, thus directly affects its performance in lesion detectability.

1.2 Literature Review

Anger, in 1964, designed the original parallel-hole collimators by first specifying a geometric radius of resolution in a given source plane and then finding the combination of hole diameter and collimator length that gave the maximum geometric efficiency for the desired radius of resolution. The septal thickness was chosen to give 95% attenuation when a photon traveled the minimum distance through the collimator (excluding hole edge effects) [13].

Keller, in 1968, optimized the geometric solid angle of acceptance about a point source and showed that the optimum collimator length for a given energy is independent of the geometric radius of resolution. Keller also used the 95% attenuation criterion for determining septal thickness [14].

Walker, in 1969, defined a figure of merit equal to the ratio of the geometric efficiency of the collimator and the square of the overall radius of resolution RT, where RT, is the square root of the sum of squares of the geometric and detector resolutions. Walker programmed a digital computer to generate curves of figure of merit against each design parameter individually holding all other parameters fixed. Walker's calculations verify Keller's analytical results; the optimum collimator thickness is independent of the radius of resolution [15].

These methods result in satisfactory collimator designs for static imaging. However, they do not necessarily produce the best collimators for rapid sequential imaging and quantitative dynamic function studies where the goal is to obtain images that correspond to the instantaneous dynamic distribution of the radioisotope. G.H. Simmons, in 1975,

introduced a new method for optimizing the design of multi-aperture parallel-hole collimators for the gamma scintillation camera. The method takes into account the frequency spectrum of a plane source object distribution as well as the energy of the radiation. A frequency dependent statistical figure of merit is calculated and combined with a weighted object distribution frequency spectrum to obtain an objective function which, when maximized, yields the optimum collimator design according to the chosen criteria. For a given gamma camera system, the detector response is fixed and the design procedure is to vary the collimator parameters to maximize the objective function by means of a sequential pattern search technique that results in the optimum collimator design for the system. The range of object dimensions, the energy of the radiation, the collimator material (lead) and the collimator-to-object distance are all held constant, and the three collimator geometric parameters, length (or thickness), hole diameter and septum thickness, are optimized simultaneously by the pattern search optimization program. The optimization is performed by means of a sequential pattern search technique [16].

G. L. Zeng et al., in 2002, investigated a new single-photon emission-computed tomography (SPECT) collimator design technique. The collimator hole diameter is the only design variable changed in that study. Other collimator parameters are fixed to a low-energy-high-resolution (LEHR) design. This task-based technique distinguishes itself from other collimator designs by considering reconstructed images and using an image reconstruction algorithm that models the collimator point-spread function [17].

Zeitler er al., in 2001, with the help of Monte Carlo simulation, designed active collimators to both collimate the tagged photon beam and suppress the background of secondary photons [18].

Lowe et al., in 2002, dealt with optimization of the design of round-hole parallel collimators for compact nuclear medicine gamma cameras. Analytical derivations of sensitivity and resolution functions were combined with the functionality of Matlab in

order to generate four groups of three collimator characteristic plots that can be employed in the collimator design optimization process [19].

Yamamura et al., in 2003, developed a novel multi-pinhole-type gamma camera for imaging low-energy gamma-ray emitters. The gamma camera consists of Imaging Plates and multi-pinhole collimators made of a lead plate with many pinholes in lattice arrangement. The shape of the collimator was determined by the parametric survey calculation so that a good spatial resolution was obtained [20].

Giokaris et al., in 2004, performed studies in order to optimize the collimator and the crystal of a gamma -camera based on a position sensitive photomultiplier with respect to its efficiency, its spatial resolution and its cost. Several parallel hole collimators of different thicknesses have been tested and compared to each other [21].

Moore et al., in 2005, described a new approach to the problem of collimator optimization in nuclear medicine; their methodology is illustrated for gallium-67 imaging. They aimed to design and compare parallel-hole collimators that are optimal for two different clinically important tasks: lesion detection and activity estimation. The design procedures were based on data from a realistic Monte Carlo simulation of photon transport through a phantom, collimator, and detector. The performance of each simulated collimator design was first evaluated for the tumor detection task using a channelized Hotelling "observer". They also evaluated performance in activity estimation by computing signal-to-noise ratio (SNR) [22]. More et al., in 2006, compared the performances of high resolution and high efficiency collimators and concluded that high-resolution collimator is best suited for imaging breast tumors [23].

Hruska et al., in 2006, investigated the effect of collimation on the detection of small (<1cm) breast tumors with dedicated nuclear breast imaging systems A breast phantom modeling tumors 4–9 mm in diameter was imaged with three dedicated systems (GE Medical Prototype CZT, Gamma Medica LumaGEM 3200 s, and Digirad 2020 tc),

and a conventional gamma camera (Elscint Helix) using a variety of system-specific and generic collimators ranging from LEUHS to LEUHR. Tumors depths and tumor-to-background activity ratio was varied. Tumor signal-to-noise ratio (SNR) was measured and compared. SNR measurements showed that an all-purpose or high sensitivity collimator is optimal for the detection of small tumors close to the collimator face [24].

1.3 Objectives

The collimator allows the gamma camera to localize accurately the radionuclide in the patient's body. Collimators perform this function by absorbing and stopping most radiation except that arriving almost perpendicular to the detector face [12]. The collimator plays an important role in the resolution and sensitivity of breast scintigraphy, thus directly affects its performance in lesion detectability. In nuclear medicine imaging, collimator design is determined by parameters such as hole size, hole length, and septal thickness.

The performance of breast scintigraphy dramatically declines in detection of lesions smaller than 1cm. Furthermore, breast dimensions have influences on recognition of abnormalities.

Mainly, the objective of this study is to improve the lesion detectability of the breast scintigraphy in breast cancer diagnosis by the optimization of the collimator. A new parallel hole collimator design that will be introduced, not only provide better image quality for a range of lesions smaller that 1cm, but also make the system more robust to the varying patient parameters (lesion size and breast dimensions).

Response Surface Methodology (RSM), which has a wide usage in many industries like pharmaceutical design and electrical device design but is not applied in nuclear medicine imaging area before, is a statistical tool that approximates the unknown relation between the inputs and the response of a system that can not be modeled using a

deterministic approach. Robust optimization will be accomplished by employing this technique which depends on performance of physical experiments. The experiments, which would be impractical if actual patient breast scintigraphy scans were used, will be realized with Monte Carlo simulation software.

1.4 Outline

Chapter 1 introduces the background, motivation and objectives of the study with an overview of the literature about the subject.

Chapter 2 gives comprehensive information about the theory of this study. Breast cancer diagnosis techniques, theory and instrumentation of breast scintigraphy imaging, collimator characteristics and image quality concept are described. Monte Carlo Method and its applications in nuclear medicine imaging are explained. Detailed information about Response Surface Methodology is presented.

Chapter 3 gives a systematic description about the materials and methods used in the thesis.

Chapter 4 presents the results of the study.

The conclusions and future work are discussed in Chapter 5.

2. THEORY

2.1 Diagnosis of Breast Cancer

The diagnosis of breast cancer is based on the utilization of physical examination, mammography and/or ultrasonography, and fine needle aspiration biopsy (FNAB) or core biopsy in accordance with the palpability and characteristics of the lesion, the age of the patient, and the density of the mammary gland [25, 26].

Even though clinical examination (inspection and palpation) is not a very sensitive test and its specificity is low, in particular for small lumps (less than 1 cm), it should be stressed that it remains the first and fundamental approach in the diagnosis of palpable breast cancer. However, during the past two decades, mammography has been completely transformed into a sophisticated technological method, with greatly improved image quality; it not only allows the recognition of very small, frequently non-palpable lesions, but also has become the method of choice for identifying breast carcinomas. The increasing use of screening mammography has resulted in an increase in the rate of detection of non-palpable lesions, and consequently in an increased demand for needle localizations and biopsies. In fact, in some cases the presence of microcalcifications at mammography is the only sign of breast cancer. It is possible to localize the position of this type of lesion with various methods: generally, a needle is positioned under mammographic control, leaving either a colored substance or a hook wire that provides a guide for the surgeon. In this way, the surgeon is able to remove the portion of the mammary gland that includes the lesion; the specimen should be submitted to radiography for confirmation of the complete removal of microcalcifications [27, 28].

It is important to point out that ultrasonography has very good ability to differentiate between cystic and solid masses, but its sensitivity for the detection of small carcinomas is not high. Its ideal use is in young women with full glandular breasts, owing

to their intrinsic radiopacity, while it can also be used for guidance in obtaining aspiration material for cytology [29].

Cytology entails the microscopic examination of cells obtained from nipple secretion, cystic fluids or fine needle biopsy of solid nodules, guided by ultrasonography or mammography in the case of non-palpable lesions. Cytology is particularly useful for breast lesions that cannot be clinically and/or mammographically defined as benign or malignant. The positive predictive value of this examination is extremely high but, unfortunately, there is a possibility of false-negative diagnosis, especially for small tumors. In such cases cytology should not be considered if clinical and/or mammographic suspicion of malignancy exists, rather, a biopsy of the lesions should be performed [30].

Figure 2.1 presents a flow chart in respect of these standard procedures for the diagnosis of palpable or non-palpable lesions of the breast.

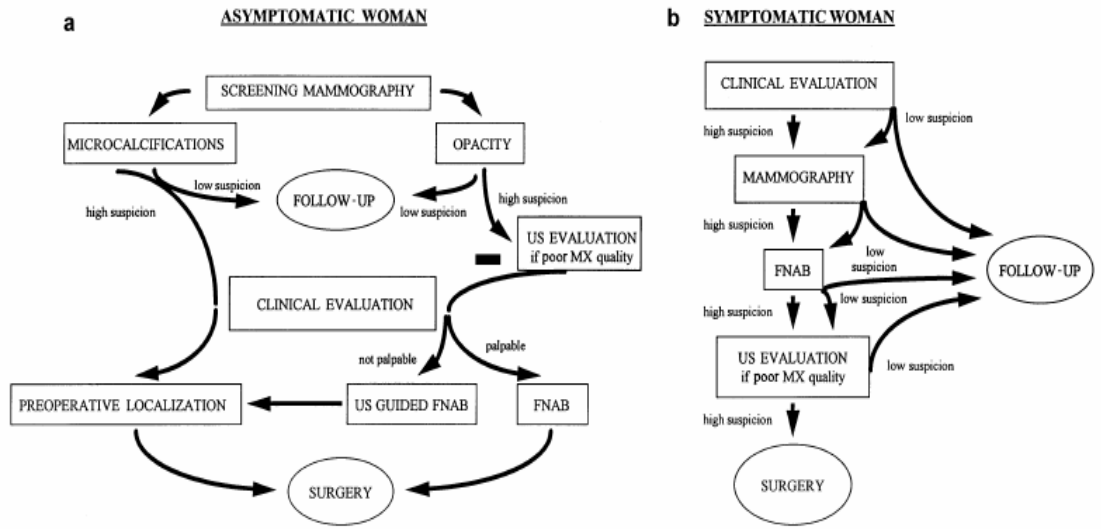

Figure 2.1 Flow chart of diagnostic procedures currently adopted at the National Cancer Institute in Milan in subjects without breast signs (a) and in patients with breast diseases (b). Fine-needle aspiration biopsy (FNAB) is preferred to core biopsy, which is often adopted in other centres. The routinely performed imaging procedures are mammography (MX) and ultrasonography (US). Other techniques such as digital mammography, computed tomography and magnetic resonance imaging are under evaluation in limited specific clinical trials [33].

2.1.1 Radiological Techniques

Obviously, new radiological methods are under evaluation, such as digital mammography and magnetic resonance (MR) imaging. Considering the former, digital technology may provide several advantages over film/screen mammography, including wider variation in exposures, easier and more efficient storage of imaging on optical disks, and the possibility of transmitting these images over distances by the use of teleradiology. This evolution of the mammographic technique also significantly decreases the duration of needle localization procedures without reducing their accuracy. However, it seems that there are no differences between conventional and digital images with regard to the detectability of microcalcifications and masses [31, 32].

MR imaging provides an interesting advantage over conventional mammography in terms of three-dimensional imaging. Three-dimension imaging is suitable for thin-slice studies, allowing the detection of small enhancing lesions that might be missed if thicker slices were used. A number of potential roles for MR imaging in the study of breast cancer have been identified, including increasing the sensitivity and specificity of breast cancer detection by comparison with mammography, identifying recurrences, and monitoring response to chemotherapy. However, to date, MR imaging remains at the investigational stage and should not be used as a routine diagnostic tool [33].

2.1.2 Nuclear Medicine Techniques

Nuclear imaging involves the injection of pharmaceutical compounds that have been labelled with radioisotopes. The compounds are selected such that they couple to some sort of biological process such as blood flow, metabolic activity or enzyme production, or such, that they tend to accumulate at specific locations in the body, e.g. binding to certain cell receptor sites. Thus the relative concentration of these radiotracers in various areas of the body gives information about the relative degree to which these biological activities are occurring. Measurement of this concentration distribution therefore provides functional information very different from the structural information supplied by

modalities such as X-ray mammography and US. For this reason, nuclear medicine techniques are being explored as adjunct imaging approaches to the structurally oriented X-ray mammography [34].

The study of breast cancer is currently one of the most interesting areas of application of nuclear medicine. The reasons for this are (a) the recent technological progress that has occurred and (b) the introduction of new radiotracers which have not only allowed the production of images visualizing the site of the lesion, but also have provided biological and functional parameters that can characterize particular aspects of the tumor (vascularization, proliferative activity, metabolic activity, receptor status etc.). The importance of these parameters resides in the fact that they could be considered as prognostic indicators or as predictive indicators of the response to therapy, and thus be of great value in treatment planning and monitoring [33].

2.2 Breast Scintigraphy

Breast scintigraphy (or scintimammography) is nuclear medicine imaging of the breast using a single gamma emitting tracer and an imaging gamma detector fitted with a collimator [34].

In the past, various gamma-emitting tracers have been studied that could be useful in the diagnosis of breast lumps in cases where mammography is inconclusive, and, more generally, could complement the diagnostic sensitivity and specificity of mammography and other radiological procedures [33]. The early studies did not, however, yield the desired results, showing a sensitivity of 75% and a specificity of 91% in the most favorable case series, but figures generally lower than mammography for palpable tumors [35]. These poor results were partly due to the inadequate performance of the first-generation gamma cameras and more generally to a variety of factors such as the testing technique, the image acquisition time, and the projections used [33].

The problem of detecting small tumors is critical for the future development and clinical acceptance of scintimammography (SM), given that the other breast imaging modalities are increasingly used for the early identification of small suspicious lesions.

Currently, SM is usually performed with the standard Anger camera, which is limited by its relatively poor intrinsic spatial resolution and by the sub-optimal detection geometry, because of the distance between the detector and the imaged breast [36].

The use of new high-resolution dedicated cameras built for breast imaging is expected to improve the detection of small lesions: these devices might be able to increase spatial resolution without sacrifices in count sensitivity and to eliminate the image-degrading effects of high uptake in some nearby tissues, like the liver and the myocardium [37]. These dedicated small field of view (from 10×10 to 20×20 cm^2) detectors add maneuverability and allow greater flexibility in patient positioning, with an increased number of available views. The patient positions comparable with those of mammography (craniocaudal and true lateral) improve breast imaging, particularly in the medial portion, and reduce image contamination from other organs, by limiting the field of view to only the breast. Moreover, using a breast-specific gamma camera, patients can be imaged seated with the arms positioned comfortably, the detector can be placed directly against the chest wall, so reducing the distance between collimator and lesion, and breast compression is allowed, increasing the target-to-background ratio and the sensitivity of the device [38].

The first preliminary clinical data in a limited number of patients indicate a higher sensitivity of these breast dedicated detectors compared with standard, large field of view cameras, and suggest that in the future such devices may be useful in routine practice [39].

2.2.1 Radiopharmaceuticals

The ideal radiopharmaceutical for scintimammography (SM) will show high tumor uptake which is cancer specific and minimal activity within the normal breast [40, 41].

Currently, the most widely used radiotracers for SM are ^{99m}Tc-sestamibi and ^{99m}Tc-tetrofosmin, which are small cationic complexes of technetium. Both these radiopharmaceuticals were introduced for myocardial perfusion imaging, and then proposed as tumor-seeking agents [42]. They both have significant dosimetric and physical advantages over the more traditional radiopharmaceuticals employed for tumor imaging, such as ^{67}Ga citrate and ^{201}Tl chloride: patients can be imaged earlier, they are available in a commercial kit form and they are also particularly suitable for single-photon emission computed tomography (SPECT) [36].

The evaluation of the tracer 2-hexakis-2-methoxyisobutyl-isonitrile (sestamibi) labeled with ^{99m}Tc for the scintigraphic examination of breast lesions is perhaps one of the most intensively studied sectors of diagnostic nuclear medicine in recent years (Fig. 2.2). Sestamibi, originally developed as a tracer for myocardial perfusion scintigraphy, is a cationic, lipophilic tracer that accumulates in the cell and mitochondria due to a negative transmembrane potential; this occurs especially in cells with a high energy metabolism (and thus rich in mitochondria), including neoplastic cells. For this reason ^{99m}Tc-sestamibi is being extensively studied as a tumor- seeking tracer [43].

^{99m}Tc-sestamibi uptake and retention in neoplastic cells depends on several factors such as regional blood flow, plasma and mitochondrial membrane potential, angiogenesis and tissue metabolism, with about 90% of tracer activity being concentrated in the mitochondria [44, 45, 46, 47]. Piwnica-Worms et al. [48] observed that ^{99m}Tc-sestamibi is a transport substrate for the P-glycoprotein (Pgp), a 170-kDa plasma membrane protein encoded by the multi-drug resistance (MDR) gene. This mechanism functions as an energy-dependent efflux pump for many drugs that are lipophilic and cationic at physiological pH. It has been suggested that the uptake and retention mechanisms for ^{99m}Tc-tetrofosmin are similar to those for ^{99m}Tc-sestamibi; however, Arbab et al. [49] showed in tumor cell lines that tetrofosmin uptake depends on both cell membrane and mitochondrial potentials, with only a small fraction accumulating inside the mitochondria. Ballinger [50] reported that ^{99m}Tc-tetrofosmin shares with ^{99m}Tc-sestamibi the property of being a substrate for Pgp. Both radiopharmaceuticals have also proved to be suitable

transport substrates for functional MDR-related protein 1, suggesting their potential usefulness in detecting the in vivo presence of multi-drug resistance in neoplasia, which can help in predicting response to chemotherapy and in the selection of proper management for patients [51].

2.2.2 Sensitivity

The sensitivity of breast scintigraphy depends on the lesion size. Waxmann et al. [52] showed that the smallest tumor visualized measured 1.3×1.1×0.9 cm, and concluded that the sensitivity of the test was reliable for tumors with a diameter >1.5 cm. In any case these are dimensions easily detectable by mammography. On the basis of these findings the test would seem more appropriate for the differential diagnosis of palpable lesions, giving useful indications for the selection of biopsy candidates, than for preoperative staging [52].

Reported values for sensitivity and specificity for planar scintimammography performed under these conditions vary according to several factors, a principle one being the distribution of lesion sizes represented in the particular study. In a three-centre European trial, sensitivities of 26%, 56%, 95% and 97% were reported for category pT1a(<0.5 cm), pT1b (0.5–1.0 cm), pT1c (1.0–2.0 cm) and pT2(>2 cm) cancers, respectively [53]. A recent clinical trial of 134 women scheduled for open breast biopsy investigated the use of prone ^{99m}Tc-sestamibi scintimammography for pT1 tumors (4.7% pT1a, 46.7% pT1b and 48.6% pT1c) and reported sensitivity, positive predictive value, negative predictive value and accuracy of 81.3%, 97.6%, 55.6% and 83.6%, respectively [54]. The corresponding values for X-ray mammography were 83.2%, 89.9%, 48.6% and 79.1%. A European multicenter trial evaluating palpable and nonpalpable breast lesions demonstrated an overall sensitivity and specificity of 80% and 73%, respectively [55]. These and other early studies reveal that while scintimammography has excellent sensitivity for tumors larger than about 1 cm, sensitivity is generally poor for smaller, nonpalpable, or medially located lesions [34].

Favorable results with this technique convinced Khalkhali [56] to conduct two multicenter clinical trials in 42 institutions in the United States and Canada. A total of 673 patients were enrolled in these two multicenter prospective trial studies; one study included 286 patients with palpable abnormalities, and the other 387 patients with non-palpable, mammographically detected abnormalities. The data were analyzed for the ability to detect malignancy in the breast, and for the ability to identify a specific abnormality as malignant. The results were similar for both analyses. Institutional analyses revealed sensitivity, specificity and positive and negative predictive values for palpable lesions of 95%, 74%, 77% and 94% respectively. For nonpalpable lesions these values were 72%, 86%, 70% and 87%, respectively. Non palpable lesions were generally less than 1 cm in diameter. The lower sensitivity observed for non-palpable versus palpable abnormalities confirmed the initial observation by Khalkhali that ^{99m}Tc sestamibi imaging has a low sensitivity for detecting cancers less than 1 cm in diameter [56].

2.2.3 Specificity

The specificity of SM is high for both palpable and nonpalpable lesions owing to the low number of false positive results, which are mainly due to focal areas of radiopharmaceutical uptake in local inflammation, fibroadenomas and fibrocystic changes [36].

The main clinical role for scintimammography is in the evaluation of indeterminate mammographic lesions or for further investigation of patients with a palpable abnormality but negative mammography [57]. False positive uptake can occur with fibroadenomas and fibrocystic disease [58] and false negative examinations have been reported with invasive lobular cancers [59]. Axillary lymph node metastases can also show increased uptake of^{99m}Tc MlBI with sensitivities of 64% to 84% and specificities of 90% to 91% [60, 61].

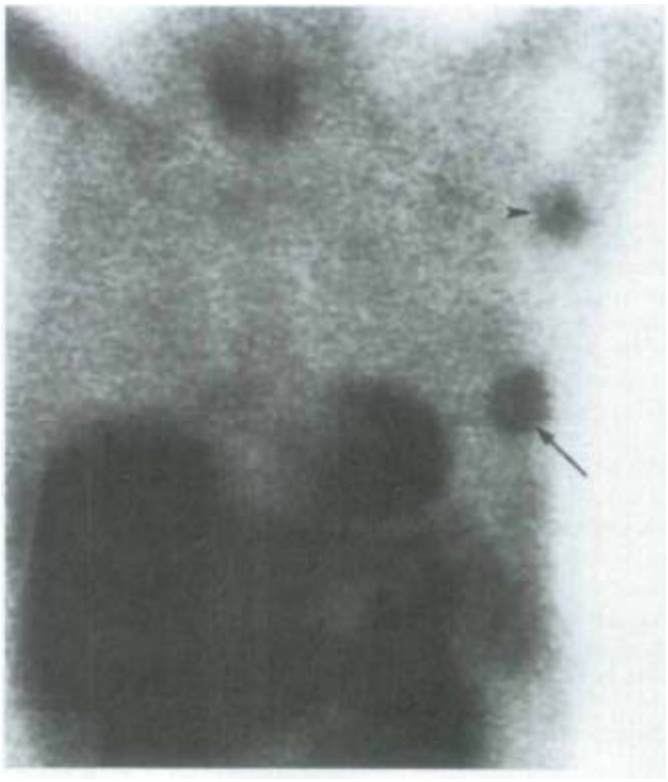

Figure 2.2 ^{99m}Tc-MIBI scintimammography (supine and prone left lateral views) showing a primary tumor in the left breast (arrow) and axillary lymph node metastases (arrow head) [57].

2.2.4 Clinical Applications of Scintimammography

In any patient for whom there is doubt about the results of mammography or other diagnostic test, scintimammography might provide added value [62]. Because radiopharmaceuticals' uptake is independent of the breast density, scintimammography can be very useful in the subgroup of population with mammographically dense breasts [63]. Moreover, scintimammography is particularly useful in patients with doubtful microcalcifications or parenchymal distortions, in the presence of scar tissue in the breast following surgery or biopsy, and in breasts with implants [64]. It is well known that mammography is less accurate in evaluating breasts that have been previously submitted to surgery, biopsy, radiation therapy or chemotherapy. Patients who have a scar within the breast due to these iatrogenic interventions are often difficult for mammographic interpretation, whereas scintimammography is not affected by these morphologic changes. Some considerations regarding the possible role of scintimammography in the

identification of multifocal–multicentric breast cancer and in the detection of the possible primary breast tumor in patients with metastatic axillary lymphnode involvement. The detection of multicentric lesions is of the utmost importance, because it can determine the surgical management of the patient (i.e. total mastectomy instead of quadrantectomy). It has been reported that scintimammography is able to assess the presence of a multifocal–multicentric disease, detecting bilateral breast cancers, with higher sensitivity when compared to mammography/ ultrasound [65].

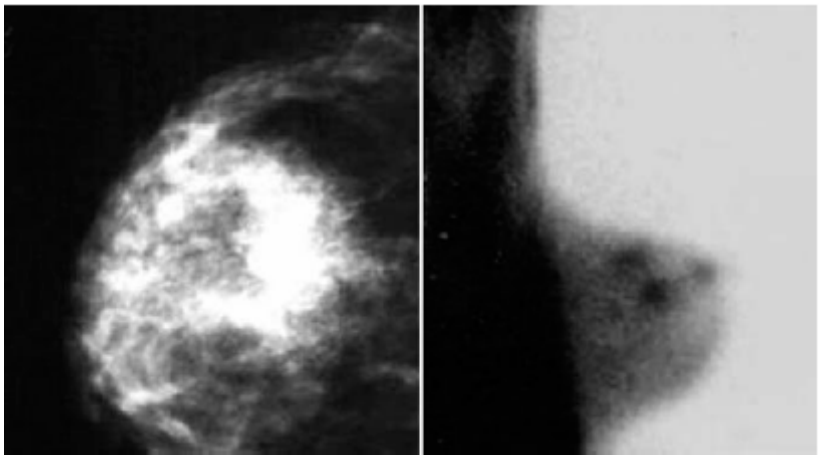

Figure 2.3 A 44-year-old patient with very dense breast tissue in the right breast. Little can be seen on mammography (left-hand image); however, scintimammography (right-hand image) clearly reveals a 25-mm ductal carcinoma with two adjacent sites of DCIS. (Note that the transmission mammogram points in the opposite direction to the emission SM images) [36].

However, due to the limited data available in this specific application along with the low sensitivity of scintimammography in visualizing small additional malignant lesions [66], this potential indication deserves further studies in larger series; moreover, the good performance of MRI in this field should be taken into account. In patients with axillary lymph-node metastases due to adenocarcinoma with negative mammography and ultrasound, scintimammography may be useful for detecting the possible primary tumor in the breast. Nevertheless, also for this application, until now there is not sufficient evidence to recommend a routine clinical use of breast scintigraphy.

Scintimammography in patients with locally advanced breast cancer can be useful both for monitoring and predicting response to neoadjuvant chemotherapy. In a study

protocol including two scintigraphies before and after neoadjuvant chemotherapy, scintimammography proved accurate in predicting tumor presence or absence after treatment, and useful for the in vivo detection of intrinsic and acquired resistant cancers, a very important factor for planning the best therapeutic strategy [67].

Scintimammography can be a useful complement to non-diagnostic mammography in some specific indications and is able to potentially reduce the number of unnecessary biopsies [68].

2.2.5 Clinical Results

On the basis of these data it is evident that scintimammography can be proposed as a complementary examination in those patients in whom mammography is difficult to interpret, as is most often the case in patients with high breast density. In a small group of 48 patients with palpable breast lesions, not clearly interpreted by mammography, Khalkhali et al. reported a 93.7% sensitivity and a 90.6% specificity for scintimammography, while the sensitivity and the specificity of mammography were 82.2% and 46.1%, respectively [69].

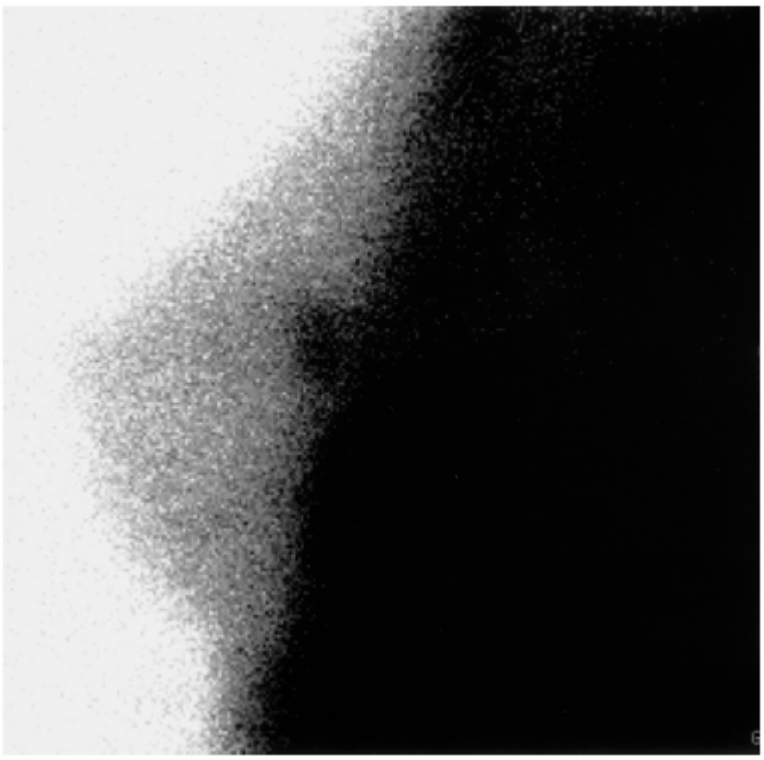

Figure 2.4 A 40-year-old female with a deep indefinite palpable mass (1.5×1 cm) noted in the upper outer quadrant of the left breast. Mammography demonstrated suspicious microcalcifications. ^{99m}Tc-sestamibi scintimammography demonstrated an area of increased focal uptake in the left breast corresponding to clinical and mammographic findings, mainly evident in the lateral projection, suggestive of breast carcinoma. The patient underwent quadrantectomy, and histology confirmed the presence of ductal carcinoma [33].

It is unquestionable that mammography is still to be considered the reference method for the study of breast masses; in fact, its application in clinical practice has substantially reduced the mortality due to breast cancer [70, 71]. Nevertheless, at present some issues in breast cancer are not satisfactorily solved by conventional imaging, and new information provided by alternative techniques can be of interest. These obscure fields concern situations such as dense breast tissue, the presence of microcalcifications without a palpable mass, severe scarring after surgery with or without radiation therapy, the exclusion or early detection of malignancy around silicone implants, and other selected problem cases like the detection of internal quadrant tumors. In addition, the evaluation of local and regional lymph nodal involvement represents a very important problem, and monitoring of the effects of therapy on cancer lesions is another area of great relevance. In this scenario, the nuclear medicine techniques can integrate the diagnostic information deriving from the clinical evaluation and from other imaging procedures. It has been

demonstrated that mammoscintigraphy with ^{99m}Tc-sestamibi is somewhat more complex to perform than mammography, but can yield useful information in situations where the mammographic picture is difficult to interpret (patients with so-called radio-opaque breasts and controversial clinical test results). In these cases it could also provide important morphological information for the surgeon who is planning a biopsy or a surgical intervention. Scintigraphy with ^{99m}Tc-MDP can give prognostic information and could therefore be employed for different purposes, in combination with mammography [33].

2.3 Instrumentation of Breast Scintigraphy

A single- or multiple-head gamma camera is needed to acquire planar and/or tomographic (SPECT) images. This gamma camera should be equipped with a low energy, high-resolution collimator. An imaging table (mattress) with specially designed breast cutouts to allow the breast to be fully dependent or with a foam cushion with a lateral semicircular aperture is required. The energy window for image collection should be 10% (±5%) centered over the 140-keV photopeak of ^{99m}Tc [72].

2.3.1 Gamma Camera

The purpose of radionuclide imaging is to obtain a picture of the distribution of a radioactively labeled substance within the body after it has been administered to a patient. The first attempts at radionuclide imaging occurred in the late 1940s. An array of radiation detectors was positioned on a matrix of measuring points around the head. A significant advance occurred in the early 1950s with the introduction of the rectilinear scanner. With this instrument, the detector was scanned mechanically in a raster-like pattern over the area of the interest.

The first gamma-ray “camera” capable of recording at all points in the image at one time was described by Hal Anger in 1953. He used a pinhole aperture in a sheet of lead to

project a γ-ray image of the radioactive distribution onto a radiation detector comprised of a NaI(Tl) screen and a sheet of x-ray film. The film was exposed by the scintillation light flashes generated by the γ rays in the NaI(Tl) (thallium-activated sodium iodide) screen. This detection system (especially the film component) was so inefficient that hour-long exposures and therapeutic levels of administrated radioactivity were needed to obtain satisfactory images [73].

In the late 1950s, Anger replaced the film-screen combination with a single, large area, NaI(Tl) crystal and a photomultiplier tube (PMT) assembly to greatly increase the detection efficiency [73]. This camera, which is called as a gamma camera (Anger camera) converts photons emitted by the radionuclide in the patient into a light pulse and subsequently into a voltage signal. This signal is used to form an image of the distribution of the radionuclide [74].

The basic components of a gamma camera system are the collimator, the scintillation crystal, an array of photomultiplier tubes (PMTs), a pulse height analyzer (PHA), a cathode ray tube (CRT), and the control console. A computer is also an integral part of the system [73].

2.3.1.1 Image formation. Firstly, an imaging collimator is used to define the direction of the detected γ rays. The collimator most commonly consists of a lead plate containing a large number of holes. By controlling which γ rays are accepted, the collimator forms a projected image of the γ-ray distribution on the surface of the scintillation NaI(Tl) crystal.

The gamma camera employs a single, large area, NaI(Tl) crystal, usually 6 to 12.5mm thick x 25 to 50cm in diameter. Rectangular crystals, with sizes of up to 60 x 40cm also are available. This crystal has an optical glass window on the back surface of the casing which permits the scintillation light to reach the PM tubes [73].

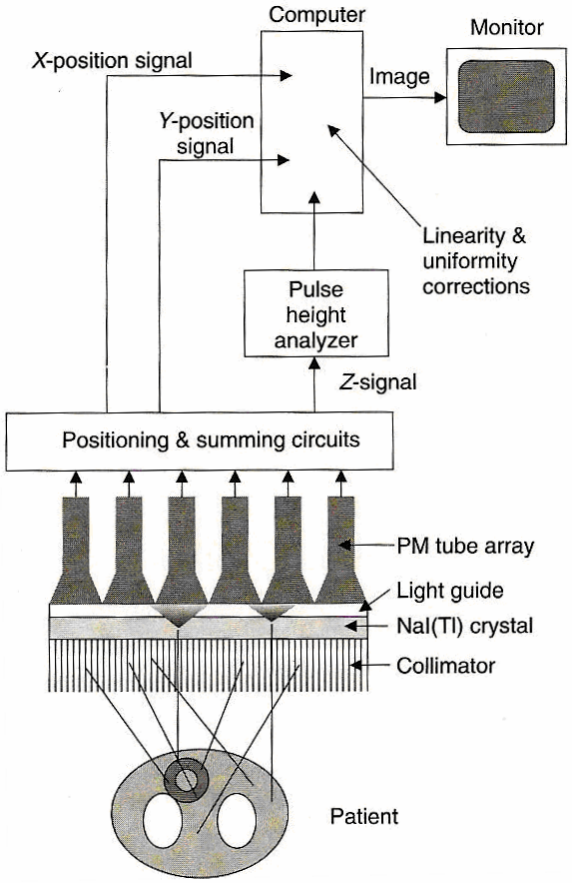

Figure 2.5 Basic principles and components of the gamma camera. In a fully digital gamma camera, the individual photomultiplier (PM) tube outputs are digitized. The positioning and summing circuitry, and the pulse-height analyzer, are replaced by software running on a computer [73].

Radiation emerging from the patient and passing through the collimator may interact with the crystal. Interaction of the gamma ray with the crystal may result in ejection of an orbital electron (photoelectric absorption), producing a pulse of fluorescent light (scintillation event) proportional in intensity to the energy of the gamma ray.

The second is that the scintillation crystal is viewed by an array of photomultiplier tubes (PM tubes), rather than a single PM tube. PMTs situated along the posterior crystal face detect this light and amplify it. A scintillation event occurring in the crystal is recorded by one or more PMTs. Localization of the event in the final image depends on the amount of light sensed by each PMT and thus on the pattern of PMT voltage output. The summation signal for each scintillation event is then formed by weighing the output of

each tube. This signal has three components: spatial coordinates on X and Y axes as well as a signal (Z) related to intensity.

The basic principle of the Pulse-Height-Analyzer (PHA) circuit is to discard signals from background and scattered radiation from interfering isotopes, so that only photons known to come from the photopeak of the isotope being imaged are recorded. The PHA discriminates between events occurring in the crystal that will be displayed or stored in the computer and events that will be rejected. The PHA can make this discrimination because the energy deposited by a scintillation event in the crystal bears a linear relation to the voltage signal emerging from the PMTs [74].

The X and Y values are binned into a discrete two-dimensional array of image elements, or pixels, and an image formed from a histogram of the number of events at each possible X, Y location. Large numbers of events are required to form an interpretable image because each pixel must have a sufficient number of counts to achieve an acceptable signal-to-noise level. Since images often are formed in 64x64-pixel or 128x128-pixel arrays, the counting requirements are some 103 to 104 times higher than for a simple counting detector.

Images are displayed on a computer monitor, where image brightness and contrast may be manipulated and different color tables may be employed. Although nuclear medicine, like other disciplines in radiology, is gradually moving toward a “filmless” environment, many physicians still prefer to look directly at film images on a light box. Thus, dedicated film recorders that can capture the image shown on a computer monitor onto photographic film still are widely used [73].

2.3.1.2 Sensitivity. In a typical imaging situation, only a small fraction of the gamma camera photons emitted by the radioactive material contribute to the formation of the image. The only photons that contribute to the image are the ones passing through the appropriate collimator hole and absorbed in the crystal. Photons from the source that are not absorbed in the crystal wasted and do not contribute to image formation. This characteristic of a gamma camera is generally referred to as sensitivity. The sensitivity of a camera can be described in terms of photons detected and used in the image for each unit of radioactivity.

Camera sensitivities are generally in the range of 100 to 1000 cps/μCi. Since 1μCi typically yields 37000 photons per second, this means less than 3% of the emitted photons are used for image formation [75].

2.3.1.3 Resolution. Resolution is one of the common performance parameters for gamma cameras. Resolution usually refers to either spatial or energy resolution. Spatial resolution is the ability to display discrete but contiguous sources of radioactivity [76]. It refers to the sharpness or detail of the image, or to the ability of the imaging instrument to provide such sharpness or detail. The spatial resolution of various gamma camera systems is usually given in terms of either inherent of overall resolution [73].

Intrinsic resolution (inherent spatial resolution) is the ability of the crystal PMT detector and accompanying electronics to record the exact location of the light pulse on the sodium iodide crystal. Marked improvements in gamma cameras have allowed an intrinsic resolution of about 3mm.

Statistical variability is particularly important in resolution. An event occurring exactly between two PMTs does not always give the same number of photons to each tube; thus, for any single event, the distribution of photons is statistically variable. Statistical variation is relatively greater when fewer light photons are available. In other words, the intrinsic resolution of a system or its ability to localize an event is directly related to the

energy of the isotope being imaged. When radioisotopes with low-energy gamma rays are used, the camera has less inherent spatial resolution.

Another factor that affects inherent (intrinsic) resolution to a minor extent is Compton scatter. When the gamma ray interacts with the crystal, there is usually photoelectric absorption, which results in a light pulse at the point of interaction. With high-energy gamma rays, however, the initial event may be a Compton interaction or scatter (i.e., a collision between a gamma ray and a loosely bound orbital electron). This results in scattered photons with light coming from several points, even though only a single gamma ray interacted with the crystal initially [76].

Collimator resolution is perhaps the principal limiting factor when absorptive collimators are used for spatial localization. Because collimator hole diameters must be relatively large (to obtain reasonable collimator efficiency), there is blurring of the image by an amount at least as great as hole diameters. Collimator resolution also depends on source-to-detector distance [73].

Overall spatial resolution is the resolution capacity of the entire camera system, including such factors as the collimator resolution, septal penetration and scattered radiation. When the overall spatial resolution of the system with high-energy isotopes is considered, the limiting resolution is that of the collimator. When low-energy isotopes are imaged, the intrinsic resolution becomes more important than the collimator resolution. As the energy of the incident gamma ray decreases, the intrinsic resolution of the crystal decreases markedly because the lower-energy gamma rays provide less light for the PMTs to record; thus, there is more statistical uncertainty regarding the origin of the gamma ray. Although the intrinsic resolution is very important, the overall resolution determines the quality of the image because it is a combination of the resolutions of each of the components in the imaging chain, including the collimator, the inherent resolution, septal penetration and scatter.

The overall system resolution (Rs) is:

$$R_s = \sqrt{R_i^{\,2} + R_c^{\,2}} \tag{2.1}$$

where R_i is inherent spatial (intrinsic) resolution and R_c is collimator resolution [76].

2.3.1.4 <u>Contrast.</u> Image contrast refers to differences in intensity in parts of the image corresponding to different levels of radioactive uptake in the patient. In nuclear medicine, a major component of image contrast is determined by the properties of the radiopharmaceutical. In general, it is desirable to use an agent having the highest lesion-to background uptake or concentration ratio. Physical factors involved in image formation also can affect contrast. In general, factors that affect contrast in nuclear medicine also affect the statistical noise levels in the image. More specifically, they affect the contrast-to-noise ratio (CNR).

A general definition of contrast is that it is the ratio of signal change of an object of interest, such as a lesion, relative to the signal level in surrounding parts of the image. Thus, if R_o is the counting rate over normal tissue and R_l is the counting rate over a lesion, the contrast of the lesion, C_l, is defined as,

$$C_l = \frac{R_l - R_o}{R_o}$$
$$C_l = \frac{\Delta R_l}{R_o} \tag{2.2}$$

where ΔR_1 is the change in counting rate over the lesion relative to the surrounding background.

Perhaps the major factor affecting contrast is added background counting rates that are superimposed more or less uniformly over the activity distribution of interest. For example, in the absence of background counts, a certain object (e.g., a lesion) has intrinsic

contrast defined by Eq. 2.2. Suppose that a uniform background counting rate R_b is superimposed on the image. Then the lesion contrast becomes

$$
\begin{aligned}
C_l' &= \frac{(Rl + Rb) - (Ro + Rb)}{Ro + Rb} \\
&= \frac{\Delta R_l}{R_o + R_b} \\
&= \frac{\Delta R_l}{R_o}\left[\frac{1}{1 + (R_b / R_o)}\right] \\
&= C_l\left[\frac{1}{1 + (R_b + R_o)}\right]
\end{aligned}
\tag{2.3}
$$

From Eq. 2.3., it can be seen that contrast is decreased by the additional factor R_b in the denominator. This illustrates that added background can reduce image contrast.

Background counting rates can arise from a number of sources. Septal penetration and scattered radiation are two examples. Septal penetration is avoided by using a collimator that is appropriately designed for the radionuclide of interest. Scattered radiation can be minimized by pulse-height analysis; however, NaI(Tl) systems cannot reject all scatter, and rejection becomes especially difficult for γ-ray energies below about 200keV. Using a narrower analyzer window for scatter rejection also decreases the recorded counting rate and increases the statistical noise in the image. A reasonable tradeoff between counting efficiency and scatter rejection for imaging systems using NaI(Tl) detectors is obtained with a 15% energy window centered on the γ-ray photopeak [73].

2.3.1.5 <u>Noise.</u> Image noise generally can be characterized as either random or structured. Random noise refers to the mottled appearance of nuclear medicine images caused by random statistical variations in counting rate. Random noise, also called statistical noise or quantum mottle, is present everywhere in a nuclear medicine image. Even when the size of an object is substantially larger than the limiting spatial resolution of the image, statistical noise can impair detectability, especially if the object has low contrast.

Structured noise refers to nonrandom variations in counting rate that are superimposed on and interfere with perception of the object structures of interest. Some types of structured noise arise from the radionuclide distribution itself. Structured noise also can arise from imaging system artifacts (e.g., nonuniformities in Anger camera images) [73].

2.3.1.6 <u>Contrast-to-noise ratio.</u> The critical parameter for detectability is the CNR of the object in the image.

Suppose that a 2-D image contains a circular lesion of area A_l having contrast C_l (Eq. 2.2.) against a uniform background counting rate, R_o (cps/cm^2). The number of counts recorded in a background area of the same size as the lesion during an imaging time, t, is

$$\begin{aligned} No &= R_o \times A_l \times t \\ &= R_o \times \frac{\pi}{4} d_l^{\,2} \times t \end{aligned} \tag{2.4}$$

where d_l is the diameter of the lesion. The statistical variation of the counts in background areas of size A_l is

$$\begin{aligned} \sigma_{No} &= \sqrt{N_o} \\ &= \sqrt{R_o \times \frac{\pi d_l^{\,2}}{4} \times t} \end{aligned} \tag{2.5}$$

Thus, the fractional standard deviation of counts due to random statistical variations is

$$\begin{aligned} C_{noise} &= \frac{\sigma_{No}}{N_o} \\ &= \frac{1}{\sqrt{R_o \times \frac{\pi d_l^{\,2}}{4} \times t}} \end{aligned} \tag{2.6}$$

As indicated by the notation in Eq. 2.6., this factor can be considered as the "noise contrast" for a circular area of diameter d_l in background areas of the image. The ratio of lesion-contrast to noise-contrast is defined as its contrast-to-noise ratio, CNR_l.

$$\begin{aligned} CNR_l &= \frac{|C_l|}{C_{noise}} \\ &\approx |C_l| \times d_l \times \sqrt{R_o \times t} \\ &\approx |C_l| \times d_l \times \sqrt{ID_o} \end{aligned} \tag{2.7}$$

In Eq. 2.7, we have used the approximation $\sqrt{\pi/4} \approx 1$. The quantity $ID_o = (R_o \times t)$ is the background information density of the image and has units (counts/cm^2).

To detect a lesion or other object in an image, the observer must be able to distinguish between the lesion or object and noise-generated contrast patterns in background areas of the same size in the image [73].

2.3.2 Collimators

The collimator is made of perforated or folded lead and it is interposed between the patient and the scintillation crystal. It allows the gamma camera to localize accurately the radionuclide in the patient's body. Collimators perform this function by absorbing and stopping most radiation except that arriving almost perpendicular to the detector face. Most radiation striking the collimator at oblique angles is not included in the final image. Of all the photons emitted by an administered radiopharmaceutical, more than 99% are "wasted" and not recorded by the gamma camera. Less then 1% are used to generate the desired image [74].

The two basic types of collimators are pinhole and multihole.

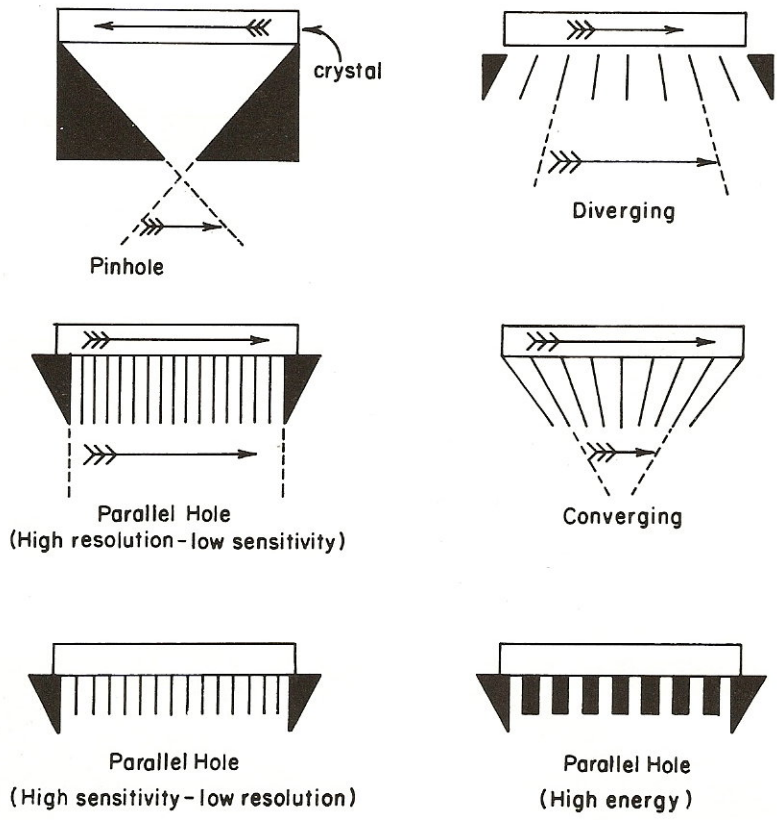

Figure 2.6 Types of gamma camera collimators [74].

2.3.2.1 <u>Pinhole collimator.</u> A pinhole collimator operates in a manner similar to that of a box camera. Radiation must pass through the pinhole aperture to be imaged, and the image is always inverted on the scintillation crystal. Collimator sensitivity refers to the percentage of incident photons that pass through the collimator. Because little of the radiation coming from the object of interest is allowed to pass through the pinhole over a given time period, the pinhole collimator has very poor sensitivity. The poor sensitivity of a pinhole collimator makes placement near the organ of interest critical, and bringing the object of interest close to the pinhole magnifies the image. Because magnification is a function of distance, if the object of interest is not relatively flat or thin, the image may be distorted. Pinhole collimators are routinely used for very high-resolution images of small organs, such as the thyroid, and for certain skeletal regions, such as hips or wrists [74].

2.3.2.2 Multihole collimator. The holes in a multihole collimator may be aligned in a diverging, parallel or converging manner. The parallel-hole collimator is probably the most widely used in nuclear medicine laboratories. It consists of parallel holes with a long axis perpendicular to the plane of the scintillation crystal. The lead walls between the holes are referred to as septa. The septa absorb gamma rays that do not emanate from the direction of interest; therefore, a collimator for high-energy gamma rays has much thicker septa than a collimator for low-energy rays. The septa are generally designed so that septal penetration by unwanted gamma rays does not exceed 10% to 25% [74].

Parallel hole collimator

A parallel hole collimator should be chosen to correspond to the energy of the isotope being imaged. Low-energy collimators generally refer to a maximum energy of 150 keV, whereas medium-energy collimators have a maximum suggested energy of about 400 keV. Collimators are available with different lengths and different widths of septa. In general, the longer the septa, the better the resolution. But, longer septa cause lower count rate (sensitivity) for a given amount of radionuclide. If the length of the septa is decreased, the detected count rate increases, and resolution decreases.

The difference between typical low-energy, general purpose collimators and low-energy, high-sensitivity collimators is that high-sensitivity collimators may allow about twice as many counts to be imaged, although the spatial resolution is usually degraded about 50%. Thus, a high resolution, low-energy collimator has about three times the resolving ability of a high-sensitivity, low-energy collimator.

Most collimators are designed with hexagonal rather than round holes. Because they have overall thinner septa, they have greater sensitivity but more septal penetration than collimators with square or round holes.

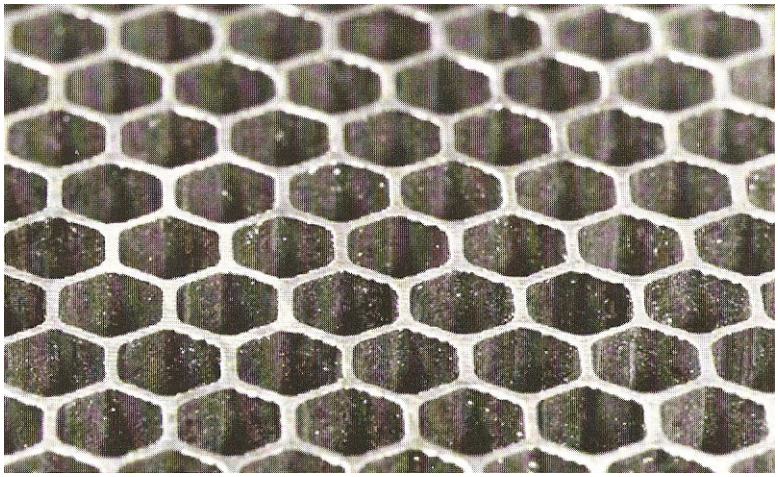

Figure 2.7 Close-up view of a typical parallel-hole collimator showing the hole structure [73].

With a parallel-hole collimator, neither the size of the image nor the count rate changes significantly with the distance of the object of interest from the collimator. This is because as the object is moved small distances away from the crystal, the inverse square law reduces the number of counts. However, this is compensated for by the increased viewing area of the collimator. On the other hand, resolution is the best when the object of interest is as close to the collimator surface as possible and scans with multihole collimators are usually obtained with the collimator in contact with or as close as possible to the patient (Figure 2.8) [73].

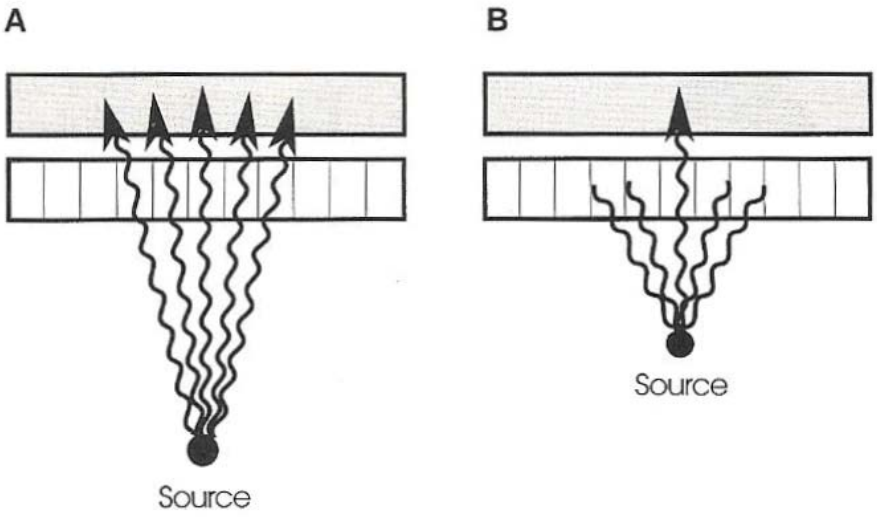

Figure 2.8 Effect of different source-to-camera distances. (A) With the source a long distance from the camera head, a large number of photons can reach the crystal in an almost perpendicular fashion. The large area of impact on the crystal increases uncertainty about the exact location of the source. (B) As the source is brought closer to the camera head, the correspondence of the scintillation event in the crystal with the actual location is much better, and resolution is improved [73].

Scattered photons emitted from the patient perpendicular to the crystal face may be imaged by a parallel-hole collimator and these photons and those that penetrate the septa cause degradation of spatial resolution (Figure 2.9). Both septal penetration and photon scattering within the patient's body cause events to be recorded in locations other than their true positions [73].

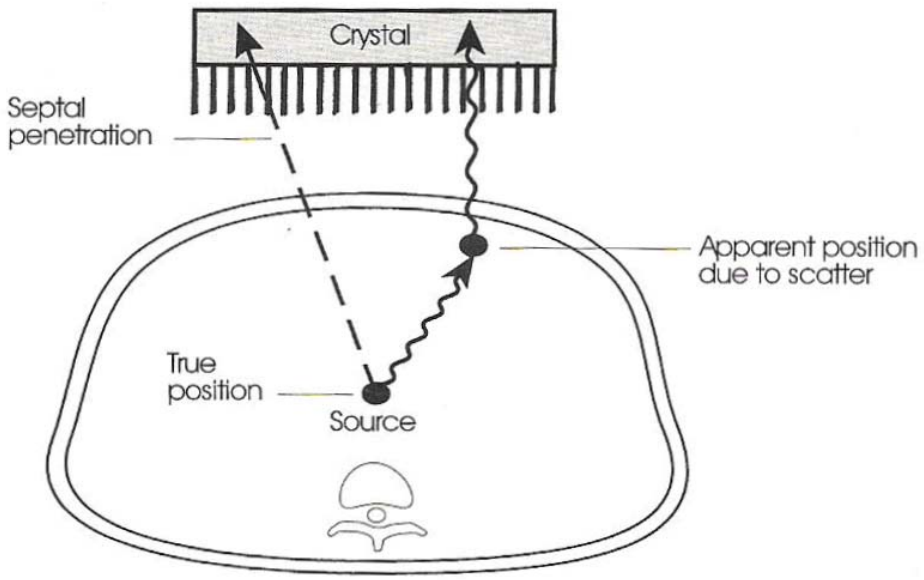

Figure 2.9 Scintillation events that degrade images. Both septal penetration and photon scattering within the patient's body cause events to be recorded in locations other than their true positions [73].

Diverging hole collimator

A diverging collimator has holes and septa that begin to diverge from the crystal face. Generally, use of diverging collimator increases the imaged area by about 30% over that obtained with parallel-hole collimator. The image itself, however, is slightly minified. With a diverging collimator, both the sensitivity and resolution worsen as the object of interest moves away from the collimator. The sensitivity worsens because the area being imaged gets larger, but the object imaged does not get larger and the inverse square law predominates. Diverging collimators are used particularly on cameras with small crystal faces to image large organs, such as the lungs [73].

Converging hole collimator

A converging collimator has holes that converge toward a point (usually 50cm) in front of the collimator. This convergence results in the formation of a magnified image in the crystal. Sensitivity increases as the object of interest moves away from the collimator face until it reaches the focal point, beyond which sensitivity begins to decrease.

Resolution, however, decreases with distance. A converging collimator may be used for examination of small areas [73].

2.3.3 Collimator Characteristics and Image Quality

The performance of a collimator is measured by three quantities: Resolution, efficiency and septum penetration, which are determined by the three collimator dimensions: hole length, hole diameter, and septal thickness. The only additional variable is the hole shape such as round, hexagonal, square, triangular, and straight or tapered.

Resolution is the quantity most directly related to the amount of detail visible in the image. Sensitivity is the measure of the counting efficiency of a system and includes the detector efficiency as well as the collimator geometric efficiency. Further, the efficiency is defined for a collimator depends on whether the source distribution it is viewing is a point source, line source, area source, or volume source. Collimator sensitivity refers to the percentage of incident photons that pass through the collimator [77]. A collimator that yields maximum sensitivity usually produces maximum image blur.

The lead walls between the holes are referred to as septa. The purpose of the collimator septa is to prevent photons from penetrating from one hole to another. When selecting a collimator, it is necessary to consider the energy of the gamma rays. The ability of a photon to penetrate a given material generally increases with photon energy. Therefore, it takes a thicker piece of material to absorb high-energy photons than it does to absorb low-energy photons. As a result, a collimator for high-energy gamma rays has much thicker septa than a collimator for low-energy rays.

The septa are generally designed so that septal penetration by undesirable gamma rays does not exceed 10%-25%. With low-energy photons, relatively thin septa are adequate. The advantage of thin septa is that more holes can be located in a given area, and that makes the sensitivity higher. However, thicker septa must be used with high-energy

photons in order to prevent photons from crossing over from one hole to another (Figure 2.10).

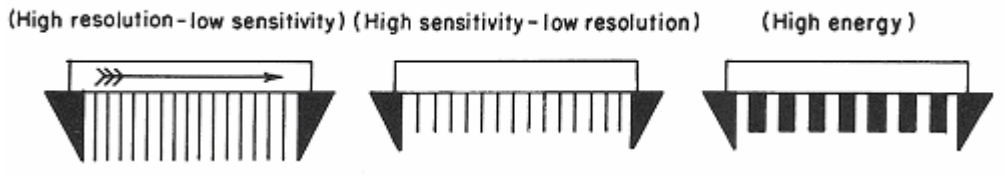

Figure 2.10 Comparison of low-energy and high-energy parallel-hole collimators [74].

If a low energy collimator is used with high-energy photons, significant septal penetration will occur, and the image will be abnormally blurred. If a high-energy collimator is used with low-energy photons, an image of normal quality will be obtained, but the camera will be operating with less than optimum sensitivity.

Collimators are available with different lengths and widths of septa. In general, the longer the septa, the better the resolution. But, longer septa causes lower count rate (sensitivity) for a given amount of radionuclide. The count rate is inversely proportional to the square of the collimator hole length. If the length of the septa is decreased, the detected count rate increases and resolution decreases (Figure 2.11) [74].

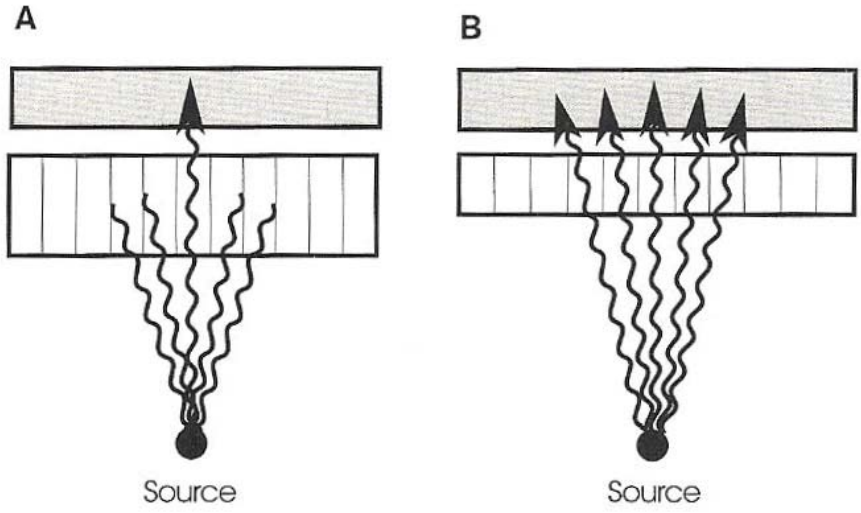

Figure 2.11 Effect of septal length on collimator sensitivity and resolution (A) Longer septa in the collimator attenuate most photons, except those exactly perpendicular to the crystal face. This increase in selectivity increases the resolution and decreases the count rate detected. (B) Shortening the length of the septa allows more photons to reach the crystal; thus, the count rate is higher. The spatial resolution, however, is decreased because the photons coming through a hole in the collimator are from a larger area [74].

2.4 Monte Carlo Method and Its Use In Nuclear Medicine

The Monte Carlo method is utilized in a very broad area of science, in which many processes, physical systems and phenomena are simulated by statistical methods employing random numbers. The general idea of Monte Carlo analysis is to create a model, which is as similar as possible to the real physical system of interest, and to create interactions within that system based on known probabilities of occurrence, with random sampling of the probability density functions (PDFs). As the number of individual events (called histories) is increased, the quality of the reported average behavior of the system improves, meaning that the statistical uncertainty decreases. Almost any complex system can in principle be modeled; perhaps there is a desire to model the number of cars passing a particular intersection during certain times of the day, to optimize traffic management, or to model the number of people that will make transactions in a bank, to evaluate the advantages of different queuing systems. If the distribution of events that occur in a system

is known from experience, a PDF can be generated and sampled randomly to simulate the real system [78].

Monte Carlo techniques have become one of the most popular tools in different areas of medical physics following the development and subsequent implementation of powerful computing systems for clinical use [79]. In particular, they have been extensively applied to simulate processes involving random behavior and to quantify physical parameters that are difficult or even impossible to calculate analytically or to determine by experimental measurements. The applications of the Monte Carlo method in medical physics cover almost all topics, including radiation protection, diagnostic radiology, radiotherapy and nuclear medicine, with an increasing interest in exotic and new applications, such as intravascular radiation therapy, boron neutron capture therapy and synovectomy. With the rapid development of computer technology, Monte Carlo based treatment planning for radiation therapy is becoming practicable [78].

2.4.1 History of Monte Carlo Method

The method is called after the city in the Monaco principality, because of the roulette, a simple random number generator. The name and the systematic development of Monte Carlo methods date back to about 1944. There is however a number of isolated and undeveloped instances on much earlier occasions. For example, in the second half of the nineteenth century a number of people performed experiments, in which they threw a needle in a haphazard manner onto a board ruled with parallel straight lines and inferred the value of π= 3.14… from observations of the number of intersections between needle and lines.

In 1899, Lord Rayleigh showed that a one-dimensional random walk without absorbing barriers could provide an approximate solution to a parabolic differential equation. In 1931, Kolmogorov showed the relationship between Markov stochastic processes and certain integro-differential equations.

In the early part of the twentieth century, British statistical schools indulged in a fair amount of unsophisticated Monte Carlo work. Most of this seems to have been of didactic character and rarely used for research or discovery. Only on a few rare occasions was the emphasis on original discovery rather than comforting verification. In 1908, Student (W.S. Gosset) used experimental sampling to help him towards his discovery of the distribution of the correlation coefficient. In the same year Student also used sampling to bolster his faith in his so-called t-distribution, which he had derived by a somewhat shaky and incomplete theoretical analysis.

The real use of Monte Carlo methods as a research tool stems from work on the atomic bomb during the Second World War. This work involved a direct simulation of the probabilistic problems concerned with random neutron diffusion in fissile material; but even at an early stage of these investigations, von Neumann and Ulam refined this particular "Russian roulette" and "splitting" methods. However, the systematic development of these ideas had to await the work of Harris and Herman Kahn in 1948. About 1948, Fermi, Metropolis, and Ulam obtained Monte Carlo estimates for the eigen values of Schrodinger equation.

In about 1970, the newly developing theory of computational complexity began to provide a more precise and persuasive rationale for employing the Monte Carlo method. The theory identified a class of problems for which the time to evaluate the exact solution to a problem within the class grows, at least, exponentially with a constant, M. The question to be resolved was whether or not the Monte Carlo method could estimate the solution to a problem in this intractable class to within a specified statistical accuracy in time bounded above by a polynomial in M. Numerous examples now support this contention. Karp (1985) shows this property for estimating reliability in a planar multiterminal network with randomly failing edges. Dyer (1989) establish it for estimating the volume of a convex body in M-dimensional Euclidean space. Broder (1986) and Jerrum and Sinclair (1988) establish the property for estimating the permanent of a matrix or, equivalently, the number of perfect matchings in a bipartite graph [80].

2.4.2 Principles of Monte Carlo Method

Consider the problem of computing the mean value of a real-valued function T(x) defined over a space Σ:

$$\langle T \rangle = \int_{\Sigma} T(x) f(x) dx \tag{2.8}$$

Each value x is a possibly multidimensional quantity characterizing the state of the system. The function f is a probability density function (PDF) giving the probability that the state of the system lies between x and x+dx.

A Monte Carlo estimate, ⟨T⟩ of is obtained by randomly drawing N samples from the distribution f. Sampling from f means that the probability of choosing a sample from the interval (x, x+Δx) is f(x)Δx. The Monte Carlo estimate is given by:

$$\hat{T} = \frac{1}{N} \sum_{i=1}^{N} T(x_i) \tag{2.9}$$

Thus, the intractable integral, Eq. 2.8, is replaced by a finite sum [81].

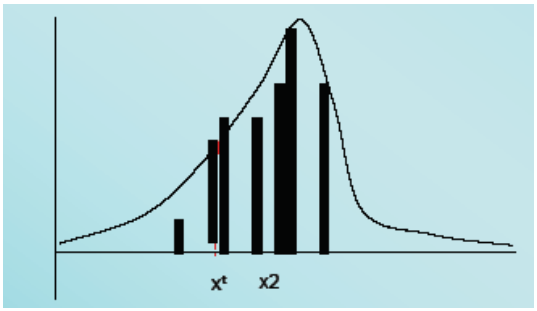

Figure 2.12 Given a very large set X and a distribution f(x) over it. We draw independent and identically distributed set of N samples and we can then approximate the distribution using these samples [82].

The statistical goodness or reliability of the estimate depends on both sample size N and the variability of the estimator which is described by the variance:

$$\sigma^2 = \int_{\Sigma} \left[\langle T \rangle - T(x) \right]^2 f(x) dx \tag{2.10}$$

Under sufficient general conditions, the central limit theorem shows that for large N, $\left(\hat{T} - \langle T \rangle \right) / \left(\sigma / \sqrt{N} \right)$ is approximately normally distributed with a mean of zero and a variance of one. Symbolically:

$$\lim_{N \to \infty} \hat{T} = \langle T \rangle$$

$$P\left(\left| T - \langle T \rangle \right| < \frac{n\sigma}{\sqrt{N}} \right) \cong \frac{1}{\sqrt{2\pi}} \int_{-n}^{n} e^{-x^2/2} dx \tag{2.11}$$

P(x) denotes the probability of event x. For example, the probability that $\hat{T}$ lies within the interval $\left(\langle T \rangle - 2\sigma / \sqrt{N}, \langle T \rangle + 2\sigma / \sqrt{N} \right)$ is 0.95.

Eq. 2.11 implies that the precision of the estimate increases with the square root of the number of histories. Thus, for each additional digit of significance, the number of histories must be increased a hundredfold [81].

Assuming that the behavior of the imaging system can be described by probability density functions (pdf's), then the Monte Carlo simulation can proceed by sampling from these pdf's, which necessitates a fast and effective way to generate random numbers uniformly distributed on the interval [0,1]. Photon emissions are generated within the phantom and are transported by sampling from pdf's through the scattering medium and detection system until they are absorbed or escape the volume of interest without hitting the crystal. The outcomes of these random samplings, or trials, must be accumulated or tallied in an appropriate manner to produce the desired result, but the essential characteristic of Monte Carlo is the use of random sampling techniques to arrive at a solution of the physical problem [77].

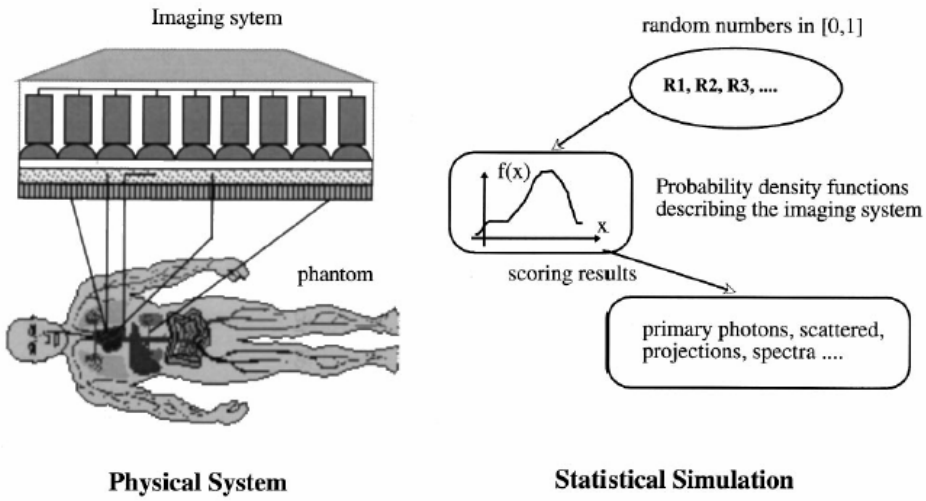

Figure 2.13 Principles of Monte Carlo simulation of an imaging system [77].

The primary components of a Monte Carlo simulation method include the following;

i) Probability density functions (pdf's): the physical system must be described by a set of pdf's.

ii) Random number generator: a source of random numbers uniformly distributed on the unit interval must be available.

iii) Sampling rule: a prescription for sampling from the specified pdf's.

iv) Scoring: the outcomes must be accumulated into overall tallies or scores for the quantities of interest.

v) Error estimation: an estimate of the statistical error (variance) as a function of the number of trials and other quantities must be determined.

vi) Variance reduction techniques: methods for reducing the variance in the estimated solution to reduce the computational time for Monte Carlo simulation.

vii) Parallelization and vectorization algorithms to allow Monte Carlo methods to be implemented efficiently on advanced computer architectures [77].

2.4.3 Random Numbers Generation

Monte Carlo methods make extensive use of random numbers to control the decision making when a physical event has a number of possible results. The Random Numbers Generation (RNG) is always one of the most crucial subroutines in any Monte Carlo-based simulation code. A large number of generators are readily available [83], and many of these are suitable for the implementation on any computer system, since today there is no significant distinction in floating point processing capabilities between a modern desktop and a mainframe computer.

A typical simulation uses from 107 to 1012 random numbers, and subtle correlations between these numbers could lead to significant errors. The largest uncertainties are typically due more to approximations arising in the formulation of the model than those caused by the lack of randomness in the RNG. Mathematically speaking, the sequence of random numbers used to affect a Monte Carlo model should possess the following properties [84].

i) Uncorrelated sequences: The sequences of random numbers should be serially uncorrelated. Most especially, n-tuples of random numbers should be independent of one another.

ii) Long period: Ideally, the generator should not repeat; practically, the repetition should occur only after the generation of a very large set of random numbers.

iii) Uniformity: The sequence of random numbers should be uniform, and unbiased. Suppose we define n-tuples $\mu_i^{\,n} = (u_{i+1},...,u_{i+n})$ and divide the n-dimensional unit hypercube into many equal subvolumes. A sequence is uniform if in the limit of an infinite sequence all the sub-volumes have an equal number of occurrences of random n-tuples.

iv) Reproducibility: When debugging programs, it is necessary to repeat the calculations to find out how the errors occurred. The feature of reproducibility is also helpful while porting the program to a different machine.

v) Speed: It is of course desirable to generate the random numbers fast.

vi) Parallelization: The generator used on vector machines should be vectorizable, with low overhead. On massively parallel architectures, the processors should not have to communicate among themselves, except during initialization [77].

The most commonly used generator is the linear congruential RNG (LCRNG). Recently, Monte Carlo researchers have become aware of the advantages of lagged Fibonacci series (LFRNG). With extremely long periods, they are generally faster than LCRNG and have excellent statistical properties [77].

2.4.3.1 Linear congruential generators. The LCRNG has the form [85]

$$u_{n+1} = a(u_n + c) \bmod(m) \tag{2.12}$$

where m is the modulus, a is the multiplier and c is the additive constant or addend. The size of the modulus constrains the period, and is usually chosen to be either prime or a power of 2 [86].

An important subset of LCRNG is obtained by setting c=0 in Eq. 2.12 which defines the multiplicative linear congruential RNG (MLCRNG). This generator (with m a power of 2 and c=0) is the de facto standard included with FORTRAN and C compilers [87].

One of the biggest disadvantages to using a power of modulus 2 is that the least significant bits of the integers produced by these LCRNGs have extremely short periods. For example, μnmod(2j) will have a period of 2j [86]. In particular, this means the least-significant bit of the LCRNG will alternate between 0 and 1.

2.4.3.2 Lagged-Fibonacci generators. The lagged-Fibonacci series RNG (LFRNG) have the following general form [88]:

$$u_n = U_{n-l} \otimes u_{n-k} \bmod(m)\text{, } 1>k \tag{2.13}$$

where $\otimes$ may be one of the following binary arithmetic operators +, -, x, l and k are the lags and m is a power of 2 ($m=2^P$). In recent years the additive lagged-Fibonacci RNG (ALFRNG) has become a popular generator for serial as well as scaleable parallel machines [89] because it is easy to implement, it is cheap to compute and it does well on standard statistical tests, especially when the lag k is sufficiently high (such as k=51279). The maximal period of the ALFRNG is (2k-1)(p-1) and has 2(k-1)(p-1) different fullperiod cycles [90]. Another advantage of the ALFRNG is that one can implement these generators directly in a floating-point to avoid the conversion from an integer to a floating-point that accompanies the use of other generators. However, some care should be taken in the implementation to avoid floating-point round-off errors [77].

2.4.4 Sampling

Some information about the process to be simulated is needed in all Monte Carlo calculations. This information is expressed as probability distribution functions, pdfs, for the different processes [91]. These pdf's, supplemented by additional computations; describe the evolution of the overall system, whether in space, energy, time or even some higher dimensional phase space. The goal of the Monte Carlo method is to simulate the imaging system by random sampling from these pdf's and by performing the necessary supplementary computations needed to describe the system evolution. In essence, the physics and mathematics are replaced by random sampling of possible states from pdf's that describe the system. Thus, it is frequently necessary to sample some physical event, the probability of which is described by a known pdf [77].

A pdf is defined over the range of [a,b]. The function is ideally integrable so that the function can be normalized by integration over its entire range. A stochastic variable, X, that follows a particular pdf, can be sampled from a known frequency function f(x) by the use of uniformly distributed random numbers R in the range [0-1]. The cumulative distribution function F(x) of the frequency function f(x) gives the probability that the random variable X is less or equal to x. It is defined as:

$$F(x) = probability(X \leq x) = \int_{a}^{x} f(\tau) d\tau \tag{2.14}$$

where a≤x≤b. Three different methods can be used to obtain a stochastic value x [77, 91].

2.4.4.1 Direct (distribution function) method. This method can be used if the inverse of the cumulative distribution function $F^{-1}(x)$ is easily obtainable. Since F(x) is uniformly distributed in [0–1], the sampled value of x could be obtained by substituting F(x) in Eq. 2.15 by a uniform random number R, that is,

$$x = F^{-1}(R) \tag{2.15}$$

A practical example of using this technique is the calculation of the distance to the next interaction vertex. The inversion is not always possible, but in many important cases the inverse is readily obtained [77].

2.4.4.2 The rejection method. Another method of performing this when it is too complicated to obtain the inverse of the distribution function is to use the rejection technique [92], which follows the following steps:

i) define a normalized function f '(x)=f (x)/ f max(x), where f max(x) is the maximum value of f(x);

ii) sample two uniformly distributed random numbers R_1 and R_2;

iii) calculate x using the equation $x=x_{min}+R1(x_{max}-x_{min})$; and

iv) if R_2 is less than or equal to f '(x), then x is accepted as a sampled value; otherwise a new value of x is sampled.

Over a large number of samples, this technique will yield a set of values of x within the required distribution. It does, however, require two random numbers per trial and many trials may be required depending on the area under of the curve of f(x).

A typical example of using this technique is the photon energy and scattering angle resulting from incoherent scattering [77].

2.4.4.3 <u>Mixed methods.</u> When the previous two methods are impractical, the mixed method that combines the two may be used [93]. Assume that the pdf can be factored as follows:

$$f(x) = h(x).g(x) \tag{2.16}$$

where h(x) is an invertible function and g(x) is relatively flat but contains most of the mathematical complexity.

The method consists of the following steps:

i) normalize h(x) producing h'(x) such that $\int_{x_{min}}^{x_{max}} h'(x)dx = 1$;

ii) normalize g(x) producing g'(x) such that $g'(x) \leq 1$ for x in $[x_{min}, x_{max}]$;

iii) use the direct method to select an x using h'(x) as the pdf;

iv) use x and apply the rejection method using g'(x), i.e., choose a random number R, if $g'(x) \leq R$, accept x; otherwise back to step (iii) [77].

2.4.5 Variance Reduction Techniques (Nonanalog Sampling)

A direct Monte Carlo simulation using true probability functions may require an unacceptable long time to produce statistically relevant results. Photons emission is isotropic, so directional parameters may be sampled uniformly within their individual ranges. Nuclear imaging systems have a low geometrical efficiency because of the small solid angle defined by the collimator and/or the small axial aperture. Therefore, the calculation would be very ineffective in terms of required computing time [94]. It is thus desirable to bias the sampling (nonanalog sampling) by introducing different types of importance sampling and other variance reduction techniques to improve the computational efficiency of the Monte Carlo method [95].

A particle history weight, W, is introduced, which describes the probability of the particle following the current path. This weight is calculated for each particle history, and used in the calculation of the results. If an event occurs, the weight W is added to the counter rather than incrementing the counter by one unit [77].

Bielajew and Rogers [93] divided variance reduction techniques in three categories: those that concern photon transport only, those that concern electron transport only, and other more general methods. Photon-specific methods are interaction forcing [93], stratification [96], exponential transform [93], Russian roulette [93], and Particle Sampling [93

2.4.6 The Monte Carlo Method in Nuclear Medicine Imaging

There has been an enormous increase and interest in the use of Monte Carlo techniques in all aspects of nuclear imaging, including planar imaging, SPECT, PET and multimodality imaging devices. However, due to computer limitations, the method has not yet fully lived up to its potential. With the advent of high speed supercomputers the field

has received increased attention, particularly with parallel algorithms, which have much higher execution rates.

Figure 2.14 illustrates the principles and main components of Monte Carlo or statistical simulation as applied to a cylindrical PET imaging system [97]. Assuming that the behavior of the imaging system can be described by PDFs, then the Monte Carlo simulation can proceed by sampling from these PDFs, which necessitates a fast and effective way to generate uniformly distributed random numbers. Photon emissions are generated within the phantom and are transported by sampling from PDFs through the scattering medium (transmission image) and detection system until they are absorbed or escape the volume of interest without hitting the crystal matrices. The outcomes of these random samplings, or trials, must be accumulated or tallied in an appropriate manner to produce the desired result, but the essential characteristic of the Monte Carlo method is the use of random sampling techniques to arrive at a solution of the physical problem.

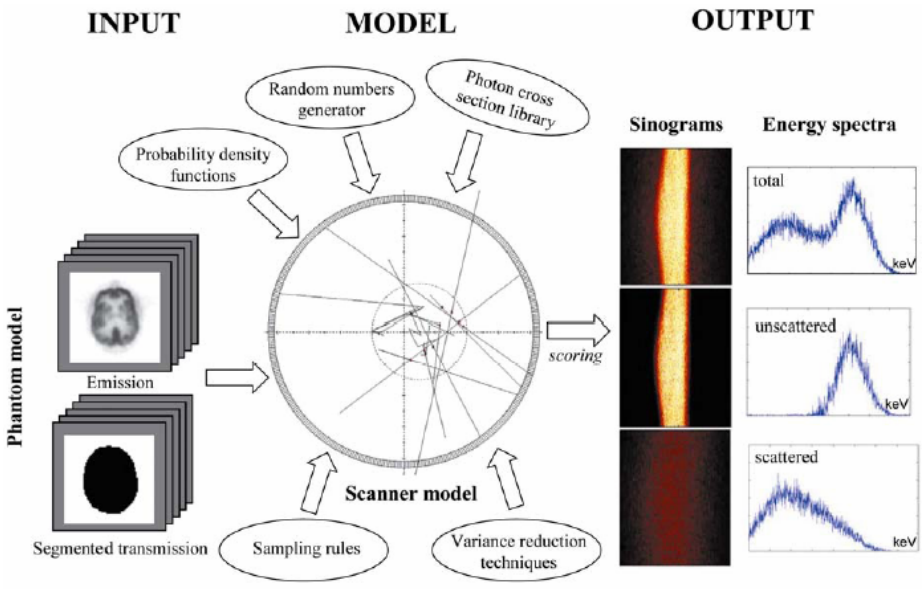

Figure 2.14 Principles and main components of a Monte Carlo simulation environment for a cylindrical multiring PET imaging system [78].

The Monte Carlo method is a widely used research tool for different areas of diagnostic nuclear imaging, such as detector modeling and systems design, image correction and reconstruction techniques, internal dosimetry and pharmacokinetic

modeling. The method has proven to be very useful for solving complex problems that cannot be modeled by computer codes using deterministic methods or when experimental measurements may be impracticable. The design of SPECT and PET systems using the Monte Carlo method has received considerable attention, and a large number of applications were the result of such investigations. During the past two decades, the simulation of scintillation camera imaging using both deterministic and Monte Carlo methods has been developed to assess qualitatively and quantitatively the image formation process and interpretation and to assist in the development of collimators. Several researchers have also used Monte Carlo simulation methods to study potential designs of dedicated small animal positron tomographs.

Another promising application of Monte Carlo calculations is the development and evaluation of image reconstruction algorithms and correction methods for photon attenuation and scattering in nuclear medicine imaging, since the user has the ability to separate the detected photons into their components: primary events scatter events, contribution of down scatter events, etc. Monte Carlo modeling thus allows a detailed investigation of the spatial and energy distribution of Compton scatter, which would be difficult to perform using present experimental techniques, even with very good energy resolution detectors [77, 91].

2.4.6.1 Detector modeling. Monte Carlo simulation of detector responses and efficiencies is one of the areas which received considerable attention. The critical component is the scintillation detector. Increased light per gamma ray interaction, faster rise and decay times, greater stopping power and improved energy resolution are the desired characteristics. Improvements in these characteristics enable detectors to be divided into smaller elements, thus increasing resolution and minimizing dead-time losses [77].

2.4.6.2 Imaging systems and collimators design. Simulations of gamma camera imaging to assess qualitatively and quantitatively the image formation process and interpretation and to assist development of collimators using deterministic methods and simplifying approximations have been developed mainly to improve speed of operation.

In gamma camera imaging, there is a compromise between sensitivity and spatial resolution in collimator selection. In 1988, Hahn et al. evaluated the properties of a cone beam (CB) collimator and three dimensional filtered back projection algorithms. For this purpose, the noise characteristics of this collimator configuration were determined and comparisons with a parallel hole (PH) collimator were made. They have used Monte Carlo simulation to gather the data used for the measurements [98]. Dye (1988) highlighted the need for an improved strategy for decision-making in equipment design and other practical issues in nuclear medicine [99].

In 1990, Gantet et al. presented a computer simulation of photon interaction with collimator septa, which allows the point spread function of scintillation camera collimators to be calculated. The method simulates photon attenuation along their propagation direction in a determinist way. Using this simulation, the spatial resolution, geometric efficiency and penetration index of collimators may be easily assessed [100].

To that end, in addition to its quantitative clinical applications, Monte Carlo simulation may be a useful research tool for tasks such as evaluating collimator design and optimizing gamma camera motion [77].

2.4.6.3 Image reconstruction algorithms. Monte Carlo simulations have been shown to be very useful for validation and comparative evaluation of image reconstruction techniques since it is possible to obtain a reference image to which reconstructed images should be compared [77].

2.4.6.4 Attenuation and scatter correction techniques. The presence of scatter and attenuation in the images limits the accuracy of quantification of activity [101]. With no corrections, the uncertainty could be as high as 50–100% [102].

Scatter does not produce major artifacts comparable to attenuation but reduces image contrast by including a low frequency blur in the image. The impact of scatter generally depends on the photon energy, camera energy resolution, and energy window settings, besides the object shape and the source distribution [103]. Many of these parameters are nonstationary, which implies a potential difficulty when developing proper scatter and attenuation correction techniques. However, correction for scatter remains essential, not only for quantification, but also for lesion detection and image segmentation.

Monte Carlo simulations have been found to be powerful tools to quantify and correct for photon attenuation and scattering in nuclear medicine imaging since the user has the ability to separate the detected photons into their components: primary events, scatter events, contribution of down-scatter events, etc. Monte Carlo modeling thus allows a detailed investigation of the spatial and energy distribution of Compton scatter which would be difficult to perform using present experimental techniques, even with very good energy resolution detectors [104].

In gamma camera imaging and SPECT, simulation programs have been used to obtain information on the different processes occurring within the phantom and the detectors. For example, energy pulse-height distribution, point-spread function and the scatter fraction can be obtained [105]. The scattered events in the energy–pulse-height distribution can be separated according to the number of scattering events in the phantom (Figure 2.15). It is clearly shown that a significant number of scattered events will be accepted by the photopeak energy window. The scatter fraction which is defined as the ratio between the number of scattered photons and the total number of photons (scattered and unscattered), is of great importance for quantitative estimation of the scattering contribution.

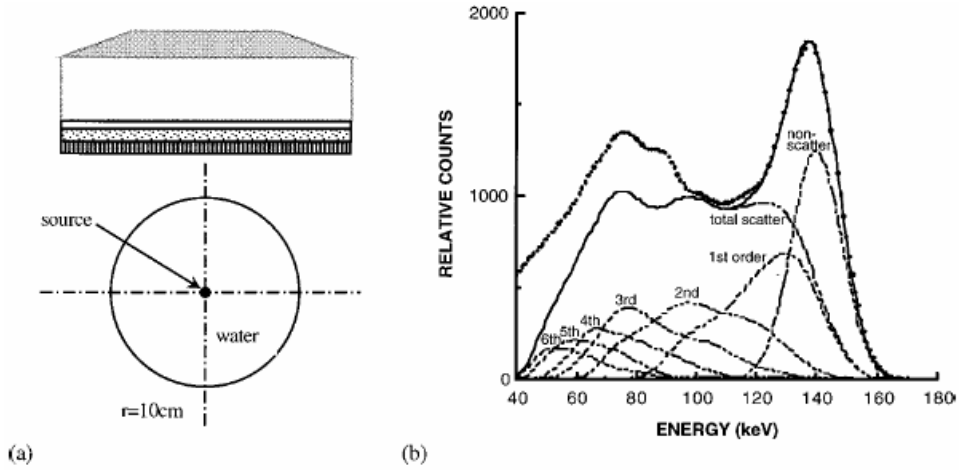

Figure 2.15 (a) Schematic view of a ^{99m}Tc line source placed at the centre of a water-filled cylinder to a scintillation camera. (b) A comparison between calculated (solid line) and experimental (dots) energy spectra for a line source on the axis of a water-filled cylinder. Distribution of the various orders of scattered and nonscattered photons is shown by broken lines [105].

2.4.6.5 Dosimetry and treatment planning. The area where early Monte Carlo simulations in the field have been performed is dosimetry modeling and computations [106]. The approach adopted by the Medical Internal Radiation Dose (MIRD) committee was first proposed in 1968 and published in a series of supplements to the Journal of Nuclear Medicine as different pamphlets [107, 108, 109]. Some of these pamphlets made extensive use of Monte Carlo calculations to derive specific absorbed fractions for electron and photon sources uniformly distributed in organs of mathematical phantoms [77].

2.4.6.6 Pharmacokinetic modeling. Pharmacokinetic modeling is a useful component for the estimation of cumulated activity in various source organs in the body. A few applications of Monte Carlo techniques have been reported in the field of pharmacokinetic modeling [77].

2.4.7 Object Model and Software Phantoms

Mathematical descriptions of human bodies and anthropomorphic phantoms are useful in radiation transport calculations. They are widely used in computer calculations of

doses delivered to the entire body and to specific organs, and are valuable tools in the design and assessment of image reconstruction algorithms.

Software phantoms modeled in imaging situations were historically limited to simple point, rod, and slab shapes of sources and attenuating media. Such simple geometries are useful in studying fundamental issues of scatter and attenuation, but clinically realistic distributions can not be evaluated by such simple geometries. A precise modeling of the human body requires appropriate information on the location, shape, density and elemental composition of the organs or tissues [77].

2.4.7.1 Object modeling. Object modeling is fundamental for performing photon and electron transport efficiently by means of a Monte Carlo method. It consists of a description of the geometry and material characteristics for an object. The material characteristics of interest include density and energy-dependent cross-sections. The modeling includes simple geometry (SG), shape-based (SB), and voxel-based (VB) approaches. The three approaches use a piecewise uniform distribution of object characteristics to model an object.

With the SG model, an object is composed of a simple combination of primitives such as cylinders and spheres. The SB approach represents the boundaries of shapes by mathematical equations. Regular shapes such as sphere, cylinder, rectangular solid, etc. have been used to approximate irregularly-shaped regions. The VB approach discretizes an object into tiny cubes (voxels) with uniform characteristics. An object is thus represented by a union of voxels of the same size.

Extensions of SG and SB models such as the solid geometry-based (SGB) approach [110] includes more primitives (ellipsoids, elliptic cylinders, tapered elliptic cylinders, rectangular solids, and their subsets: half, quarter, and eighth) and uses an inclusion tree data structure to provide relationships between primitives. These extensions provide simple irregular shape modeling. To allow anthropomorphic modeling the composite model which

is an extension to the SGB approach adds to the primitives a voxelized rectangular solid primitive [111].

2.4.7.2 Anthropomorphic phantoms. Modeling of imaging and other medical applications is best done with phantom models that match the gross parameters of an individual patient. Computerized anthropomorphic phantoms can either be defined by mathematical (analytical) functions, or digital volume arrays.

The mathematical specifications for phantoms that are available assume a specific age, height and weight. However, people exhibit a variety of shapes a. In the first MIRD pamphlets, several organs including the skeletal system were represented schematically using geometric forms (cylinders, cones and ellipsoids). The representation of internal organs with this mathematical phantom is very crude since the simple equations can only capture the most general description of the organ's position and geometry. The most studied phantom is defined as the reference man weighing 70 kg.

Mathematical phantoms are still evolving and are being constantly improved. The heterogeneity of the body has been taken into account by including soft tissues, bone and lungs with different compositions and densities. For certain organs such as the stomach and the bladder, a distinction should be made between the organ contents and the organ wall. A revised head and brain model in which the neck and head are treated as two separate compartments was developed by Bouchet in 1996. The trunk region of the Snyder–Fisher phantom without its internal organs is incorporated into the model. Based on the atlas of sectional human anatomy, a 3D computer model of a human torso, including four cavities of the heart, two lobes of the lung and the body surface and a 3D model of the myocardium was developed by Sui and Shen in 1990.

The Mathematical Cardiac Torso (MCAT) phantom is an anthropomorphic phantom, developed at the University of North Carolina at Chapel Hill, that has been used in emission computed tomography imaging research. Using mathematical formulas, the

size, shape and configurations of the major thoracic structures and organs such as the heart, liver, breasts and rib cage are realistically modeled for imaging purposes [77].

2.4.8 Monte Carlo Computer Codes

Many Monte Carlo programs have been in use in the field of nuclear imaging and internal dosimetry with many of them available in the public domain. EGS4 [112], ITS [113], MCNP [114], GEANT [115], SIMSET [116], SIMIND [117], SIMSPECT [118], MCMATV [119], PETSIM [120] and EIDOLON [121] are some of the Monte Carlo codes widely used. Key features are summarized briefly in Figure 2.16. Since SIMIND is utilized in this study, it will be described in more detail.

MC code	General description
EGS4 (Ref. 262)	Coupled photons/electrons transport in any material through user specified geometries. Simulation of imaging systems not specifically included and requires an extensive amount of user programming in MORTRAN.
ITS including TIGER, CYLTRAN, and ACCEPT (Ref. 263)	Coupled photons/electrons transport in any material through slabs, cylinders or combinatorial. Simulation of imaging systems not specifically included and requires an extensive amount of user programming in FORTRAN.
MCNP (Ref. 264)	Coupled neutrons/photons/electrons transport in any material through user generalized geometry. Simulation of imaging systems not specifically included and requires an extensive amount of user programming in FORTRAN.
GEANT (Ref. 43)	Coupled photons/electrons transport in any material through combinatorial geometry. Simulation of imaging systems not specifically included and requires an extensive amount of user programming in FORTRAN.
SIMSET (Ref. 21)	Photons transport in any material through voxel-based phantoms. Simulation of SPECT and PET imaging systems included. User modules written in C could be linked.
SIMIND (Ref. 15)	Photons transport in any material through voxel-based phantoms. Simulation of SPECT imaging systems included. User modules written in FORTRAN could be linked.
SIMSPECT (Ref. 265)	Coupled photons/electrons transport in any material through voxel-based phantoms. Simulation of SPECT imaging systems included. User modules written in FORTRAN/C could be linked.
MCMATV (Ref. 266)	Photons transport in any material through voxel-based phantoms. Simulation of SPECT imaging systems included. User modules written in FORTRAN could be linked.
PETSIM (Ref. 20)	Photons transport in any material through shape-based phantoms. Simulation of PET imaging systems included. User modules written in FORTRAN could be linked.
EIDOLON (Ref. 135)	Photons transport in any material through shape-based or voxel-based phantoms. Simulation of 3D PET imaging systems included. User modules written in C/Objective-C could be linked.

Figure 2.16 Key features of Monte Carlo codes used in nuclear medical imaging [77].

2.4.8.1 SIMIND. The SIMIND code simulates a clinical SPECT scintillation camera and can easily be modified for almost any type of calculation or measurement encountered in SPECT imaging, including transmission imaging.

The entire code has been written in FORTRAN-90 and includes versions that are fully operational on VAX-VMS, most UNIX platforms and on MS-DOS (Lahey LF90 compiler). In summary, the code works as follows: photons emitted from simulated decay in the phantom are followed step by step towards the scintillation camera. SIMIND includes an accurate treatment of photon interaction in the phantom, a protecting layer and in the crystal of the detector. The simulation of back-scattering from light guides and photomultipliers is also included. Different types of collimators can be selected. SIMIND can take advantage of anthropomorphic voxel-based phantoms developed for simulating realistic imaging situations.

The program has been shared among several groups and has been found a very useful research tool. The SIMIND code has been widely used for collimators design [122] and to evaluate attenuation and scatter correction techniques.

2.5 Response Surface Methodology

Response Surface Methodology (RSM) explores the relationships between several explanatory (independent) variables and one or more response (dependent) variables. The method was introduced by G. E. P. Box and K. B. Wilson in 1951. The main idea of RSM is to use a set of designed experiments to obtain an optimal response.

Box and Wilson suggest using a first-degree polynomial model to do this. They acknowledge that this model is only an approximation, but use it because such a model is easy to estimate and apply, even when little is known about the process. An easy way to estimate a first-degree polynomial model is to use a factorial experiment or a fractional factorial design. This is sufficient to determine which explanatory variables have an impact on the response variable(s) of interest. Once it is suspected that only significant explanatory variables are left, and then a more complicated design, such as a central composite design can be implemented to estimate a second-degree polynomial model,

which is still only an approximation at best. However, the second-degree model can be used to optimize (maximize, minimize, or attain a specific target for) a response [123].

The most extensive applications of RSM are in the industrial world, particularly in situations where several input variables potentially influence some performance measure or quality characteristic, which is called response of the product or process [124].

Figure 2.17 shows graphically the relationship between the response variable (y) and the two process variables (or independent variables) ξ_1 and ξ_2. For each value of ξ_1 and ξ_2, there is a corresponding value of y, and that we may view these values of the response as a surface lying above the ξ_1-ξ_2 plane, as in Figure 2.17(a). It is this graphical perspective of the problem environment that has led to the term response surface methodology. It is also convenient to view the response surface in the two-dimensional ξ_1-ξ_2 plane, as in Figure 2.17(b). In this presentation, we are looking down at the ξ_1-ξ_2 plane and connecting all points that have the same response (y) to produce contour lines of constant response. This type of display is called a contour plot [124].

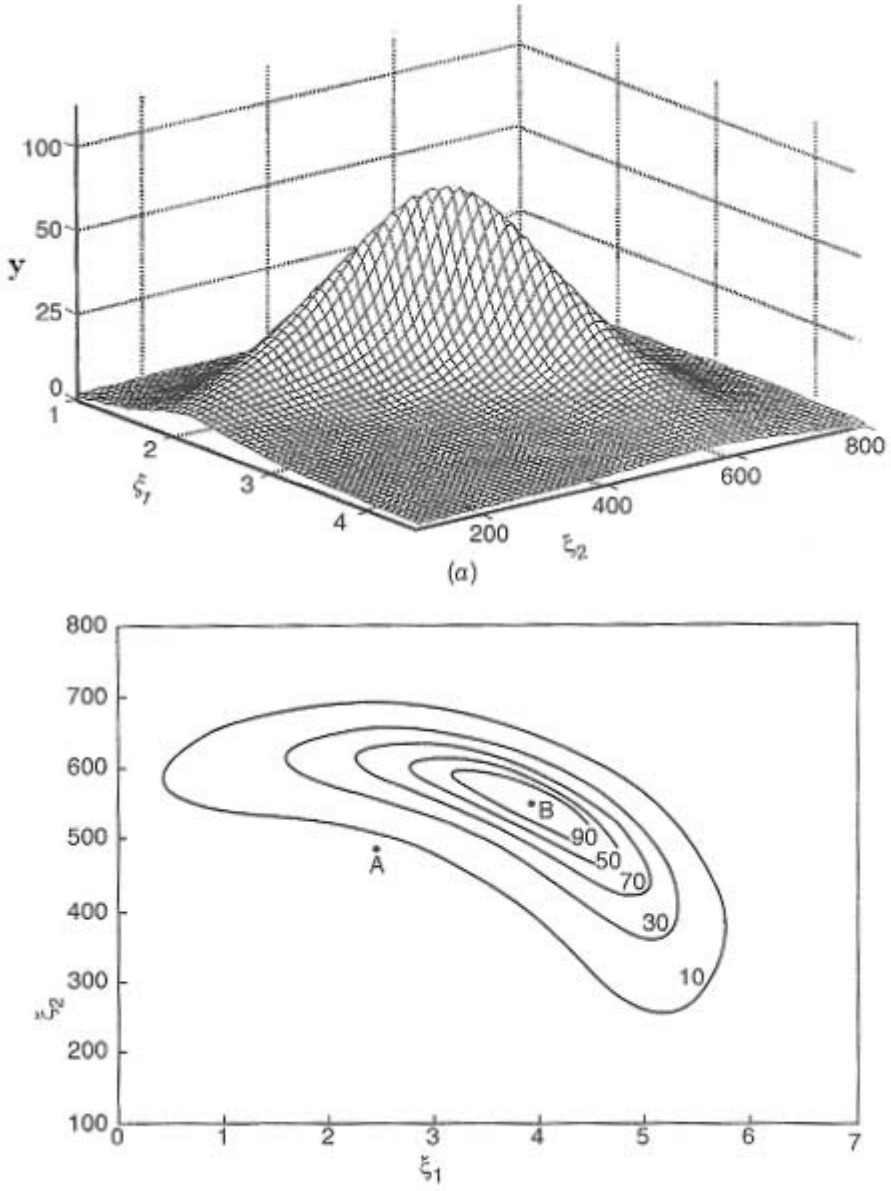

Figure 2.17 a) A theoretical response surface showing the relationship between response (y) and the process variables (ξ_1 and ξ_2). b) A contour plot of the theoretical response surface [5].

2.5.1 Dependent and Independent Variables

Independent variables, also called predictor variables, regressors, controlled variables, manipulated variables, or explanatory variables, are those whose values are controlled or selected by the experimenter to determine its relationship to an observed phenomenon (the dependent variable). In such an experiment, an attempt is made to find

evidence that the values of the independent variable determine the values of the dependent variable (that which is being measured, also known as response variable, responding variable, explained variable, or regressand). The independent variable can be changed as required, and its values do not represent a problem requiring explanation in an analysis, but are taken simply as given. The dependent variable on the other hand, usually cannot be directly controlled.

More generally, the independent variable is the thing whose value one actively controls and can change, while the dependent variable is the thing whose value then changes as a result [125].

Response Surface Methodology involves:

i) Statistical experimental design,

ii) Regression modeling, and

iii) Optimization

2.5.2 Design of Experiments

Design of experiments includes the design of all information-gathering exercises where variation is present, whether under the full control of the experimenter or not. (The latter situation is usually called an observational study.) Often the experimenter is interested in the effect of some process or intervention (the 'treatment') on some objects (the 'experimental units') [126].

The two most common designs generally used in response surface modeling are central composite designs and Box-Behnken designs. In these designs the inputs take on three or five distinct values (levels), but not all combinations of these values appear in the design. The functions described here produce specific response surface designs:

i) Central Composite Designs

ii) Box-Behnken Designs [127]

2.5.2.1 Central composite designs. Central composite designs are response surface designs that can fit a full quadratic model. To picture a central composite design, imagine you have several factors that can vary between low and high values. For convenience, suppose each factor varies from -1 to +1. One central composite design consists of cube points at the corners of a unit cube that is the product of the intervals [-1, 1], star points along the axes at or outside the cube, and center points at the origin.

Central composite designs are of three types. Circumscribed (CCC) designs are as described above. Inscribed (CCI) designs are as described above, but scaled so the star points take the values -1 and +1, and the cube points lie in the interior of the cube. Faced (CCF) designs have the star points on the faces of the cube. Faced designs have three levels per factor, in contrast with the other types, which have five levels per factor. The following figure shows these three types of designs for three factors [127].

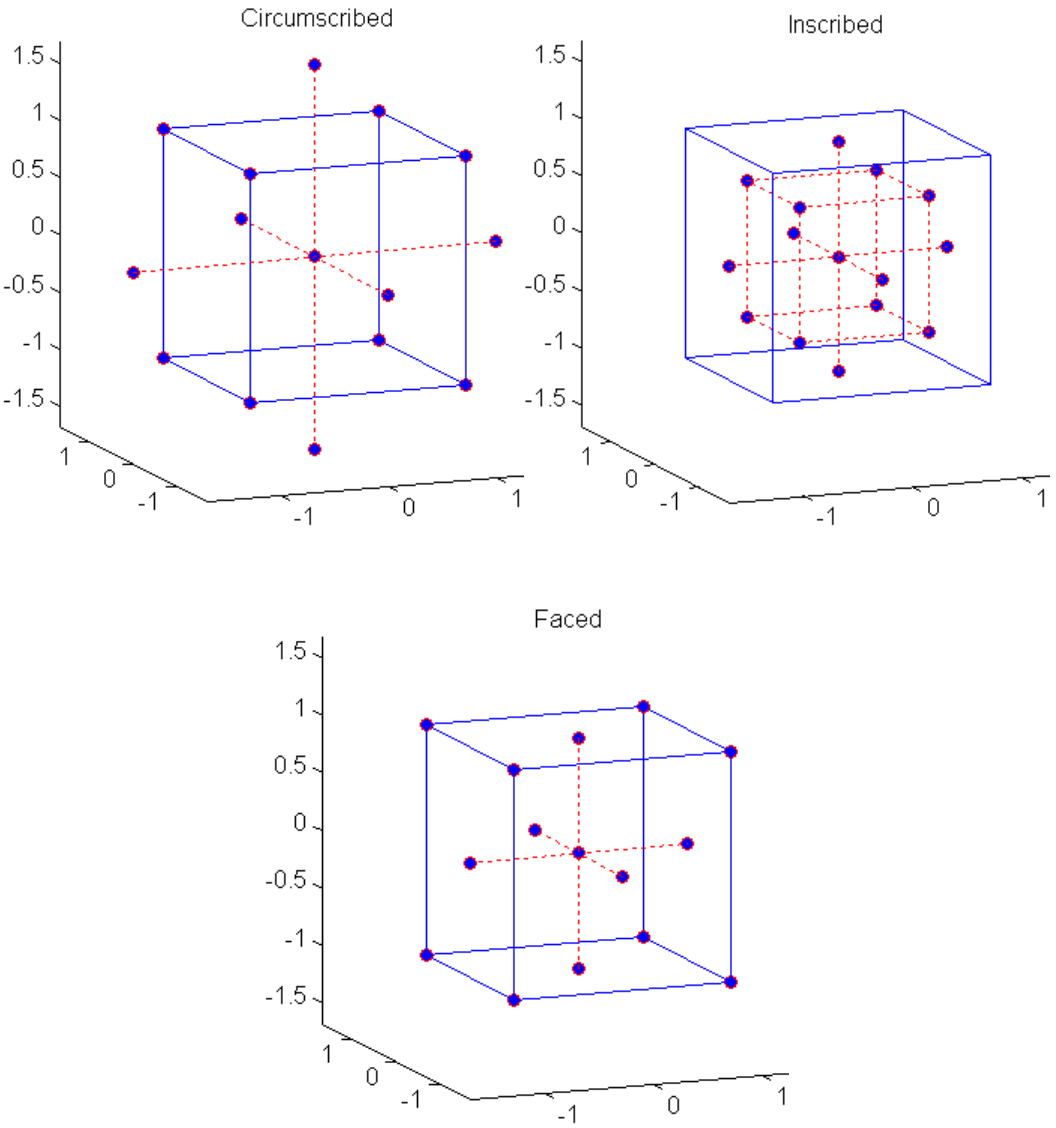

Figure 2.18 Types of Central Composite Designs: Circumscribed (CCC) Inscribed (CCI) and Faced (CCF) Designs.

2.5.2.2 <u>Box-Behnken designs.</u> Like central composite designs, Box-Behnken designs are response surface designs that can fit a full quadratic model. Unlike most central composite designs, Box-Behnken designs use just three levels of each factor. This makes them appealing when the factors are quantitative but the set of achievable values is small.

Central composite faced (CCF) designs also use just three factor levels. However, they are not rotatable as Box-Behnken designs are. On the other hand, Box-Behnken designs can be expected to have poorer prediction ability in the corners of the cube that

encloses the design, because unlike CCF designs they do not include points at the corners of that cube.

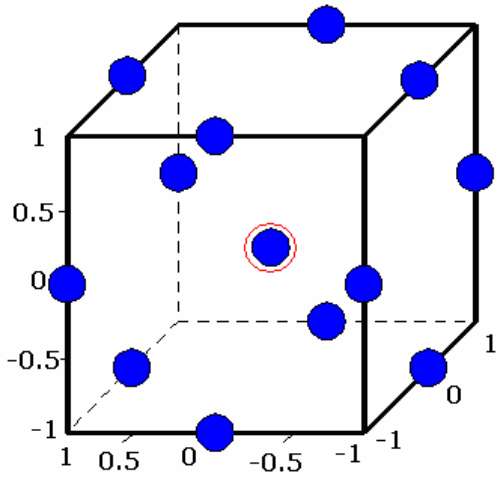

Figure 2.19 Box-Behnken Designs.

The above figure shows a Box-Behnken design for three factors, with the circled point appearing at the origin and possibly repeated for several runs. A repeated center point makes it possible to compute an estimate of the error term that does not depend on the fitted model. For this design all points except the center point appear at a distance from the origin. That does not hold true for Box-Behnken designs with different numbers of factors [127].

2.5.3 Approximating Response Functions and Model Building

In general, the experimenter is concerned with a product, process or system involving a response y that depends on the controllable input variables ξ_1, ξ_2,…, ξ_k. The relationship is

$$y = f(\xi_1, \xi_2, ..., \xi_k) + \varepsilon \tag{2.17}$$

where the form of the true response function f is unknown and perhaps very complicated, and ε is a term that represents other sources of variability not accounted for in f. Thus ε includes effects such as measurement error on the response, other sources of variation that are inherent in the process or system (background noise, or common cause of variation in the language of statistical process control), and the effect of other variables. 'ε' will be treated as a statistical error assuming it to have a normal distribution with mean zero and variance σ^2. Then,

$$E(y) \equiv \eta = E\left[f\left(\xi_1, \xi_2, ...\xi_k\right)\right] + E(\varepsilon)$$
$$= f(\xi_1, \xi_2, ..., \xi_k) \tag{2.18}$$

The variables ξ_1, ξ_2,…, ξ_k are usually called natural variables. In RSM, it is convenient to transform the natural variables to coded variables x_1, x_2,…, x_k which are usually defined to be dimensionless with mean zero and the same spread or standard deviation. In terms of the coded variables, the true response is:

$$\eta = f(x_1, x_2, ..., x_k) \tag{2.19}$$

Because of the form of the function f is unknown, we must approximate it. In fact, successful use of RSM is critically dependent upon the experimenter's ability to develop a suitable approximation for f. Usually, a low-order polynomial in some relatively small region of the independent variable space is appropriate. In many cases, either a first-order or a second-order model is used. For the case of two independent variables, the first-order model in terms of the coded variables is

$$\eta = \beta_0 + \beta_1 x_1 + \beta_2 x_2 \tag{2.20}$$

The first order model is likely to be appropriate when the experimenter is interested in approximating the true response surface over a relatively small region of the independent variable space in a location where there is a little curvature in f.

The form of the first-order model in Eq. 2.20 is sometimes called a main effects model, because it includes only the main effects of the two variables x_1 and x_2. If there is an interaction between these variables, it can be added to the model easily as follows:

$$\eta = \beta_0 + \beta_1 x_1 + \beta_2 x_2 + \beta_{12} x_1 x_2 \tag{2.21}$$

Often, the curvature in the true response is strong enough that the first-order model (even with the interaction term included) is inadequate. A second-order model is likely to be required in these situations. For the case of two variables, the second-order model is

$$\eta = \beta_0 + \beta_1 x_1 + \beta_2 x_2 + \beta_{11} x_1^2 + \beta_{22} x_2^2 + \beta_{12} x_1 x_2 \tag{2.22}$$

The second order model is widely used in response surface methodology for several reasons.

i) The second-order model is very flexible. It can take on a wide variety of functional forms, so it will often work well as an approximation to the true response surface.

ii) It is easy to estimate the parameters (the β's) in the second order model. The method of least squares is used for this purpose.

iii) There is a considerable practical experience indicating that second order models work well in solving real response surface problems.

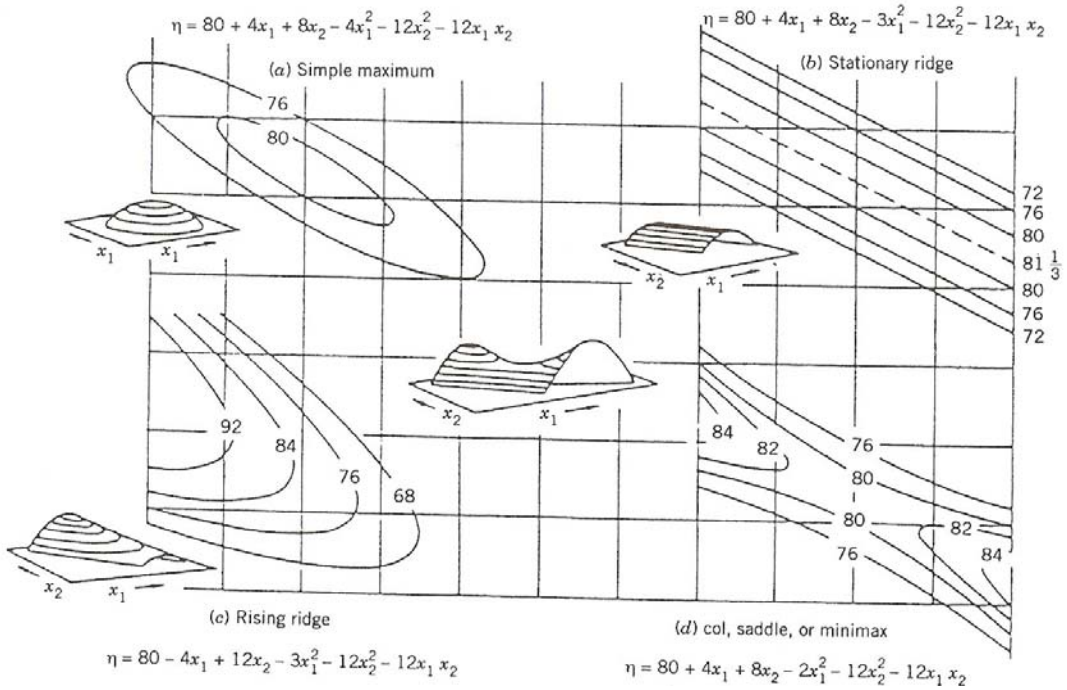

Figure 2.20 Some examples of types of surfaces defined by the second-order model in two variables x_1 and x_2 [128].

In general, the first-order model is

$$\eta = \beta_0 + \beta_1 x_1 + \beta_2 x_2 + ... + \beta_k x_k \tag{2.23}$$

and the second-order model is

$$\eta = \beta_0 + \sum_{j=1}^{k} \beta_j x_j + \sum_{j=1}^{k} \beta_{jj} x_j^2 + \sum \sum_{i<j=2}^{k} \beta_{ij} x_i x_j \tag{2.24}$$

There is a close connection between RSM and linear regression analysis. The β's in Eq. 2.23 and 2.24 are a set of unknown parameters. To estimate the values of these parameters, we collect data on the system by the help of experimental design techniques. Regression analysis is a branch of statistical model that uses these data to estimate the β's [124].

2.5.4 Sequential Nature of RSM

Most applications of RSM are sequential in nature. That is, at first some ideas are generated concerning which factors or variables are likely to be important in the response surface study. This usually leads to an experiment designed to investigate these factors with a view toward eliminating the unimportant ones. This type of experiment is usually called a screening experiment. Screening experiment is phase zero of a response surface study.

Once the important independent variables are identified, phase one of the response study, at which the experimenter's objective is to determine if the current levels or settings of the independent variables result in a value of the response that is near the optimum, or if the process is operating in some other region that is remote from the optimum. This phase of response surface methodology makes considerable use of the first-order model and an optimization technique called the method of steepest ascent.

Phase two of a response surface study begins when the process is near the optimum. At this point, the experimenter usually wants a model that will accurately approximate the true response function within a relatively small region around the optimum. Because the true response surface usually exhibits curvature near the optimum, a second-order model will be used. Once an appropriate approximating model has been obtained, this model may be analyzed to determine the optimum conditions for the process [124].

2.5.5 The Method of Steepest Ascent

In most of the RSM problems, the initial estimate of the optimum operating conditions for the system is far from the actual optimum. In such circumstances, the objective of the experimenter is to move rapidly to the general vicinity of the optimum. When we are remote from the optimum we usually assume that a first-order model is an adequate approximation to the true surface in a small region of the x's.

The method of the steepest ascent is a procedure for moving sequentially along the path of steepest ascent, that is, in the direction of the maximum increase in the response. Of course, if minimization is desired, then we call this technique the method of the steepest descent. The fitted first-order model is:

$$y = \beta_0 + \sum_{i=1}^{k} \beta_i x_i \tag{2.25}$$

and the first-order response surface, that is, the contours of y, is a series of parallel lines such as that shown in Figure 2.21. The direction of the steepest ascent is the direction in which y increases most rapidly. This direction is parallel to the normal to the fitted response surface. We usually take as the path of steepest ascent the line through the center of the region of interest and normal to the fitted surface. Thus, the step along the path is proportional to the regression coefficients (β_i). The experimenter based on process knowledge or other practical considerations determines the actual step size.

Experiments are conducted along the path of steepest ascent until no further increase in response is observed. Then a new first-order model may be fit, a new path of steepest ascent determined, and the procedure continued. Eventually, the experimenter will arrive in the vicinity of the optimum. This is usually indicated by lack of fit of a first-order model. At that time additional experiments are conducted to obtain a more precise estimation at the optimum [129].

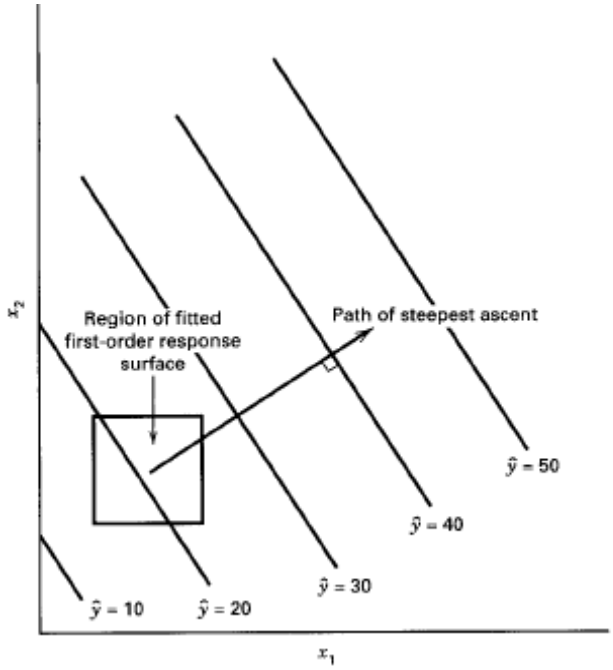

Figure 2.21 First-order response surface and path of steepest ascent [129].

2.5.6 The Analysis of Second-Order Response Surfaces

In most attempts at product improvement through the gradient technique, called steepest ascent, the investigator will encounter situations where the lack of fit attributable to curvature from these pure second-order terms is found to be quite significant. In these cases, it is likely that the model containing first order terms and two factor interaction terms β_{12}, β_{13},…, $\beta_{k-1,k}$ are inadequate.

A Taylor series expansion of Eq. 2.17 through second-order terms would result in a model of type

$$y = \beta_0 + \sum_{j=1}^{k} \beta_j x_j + \sum_{j=1}^{k} \beta_{jj} x_j^2 + \sum \sum_{i<j=2}^{k} \beta_{ij} x_i x_j \tag{2.26}$$

The geometric nature of the second-order function is displayed in Figure 2.20. In Figure 2.20 (a), the center of the system, or stationary point, is a point of maximum response. The response picture displays concentric ellipses. In Figure 2.20 (b) and (c),

stationary and rising ridge behaviors are shown. In Figure 2.20 (d), a hyperbolic system of contours is displayed. The center is neither a maximum nor a minimum point. In this case, the stationary point is called a saddle point and the system of contours is called a saddle or minimax system.

The detection of the nature of the system and the location of the stationary point are an important part of the second-order analysis. The nature of the response surface system (maximum, minimum, or saddle point) depends on the signs and magnitudes of the coefficients in the model of Eq. 2.26. The second-order coefficients (interaction and pure quadratics terms) play a vital role.

One must keep in mind that the coefficients used are estimates of the β's of Eq. 2.26. As a result, the contours represent contours of estimated response. Thus, even the system itself (saddle, maximum or minimum points) is part of the estimation process.

Consider the second-order response surface model in Eq. 2.26 in matrix notation

$$\hat{y} = b_0 + x'b + x'\hat{B}x \tag{2.27}$$

where b_0, b and $\hat{B}$ are the estimates of the intercept , linear and second-order coefficients, respectively.

$$x' = [x_1, x_2, ..., x_k]$$
$$b' = [b_1, b_2, ..., b_k]$$
$$\hat{B} = \begin{bmatrix} b_{11} & b_{12}/2 & \dots & b_{1k}/2 \\ & b_{22} & \dots & b_{2k}/2 \\ & & . & . \\ & & & . \\ sym. & & & b_{kk} \end{bmatrix} \tag{2.28}$$

It is straightforward to give a general expression for the location of the stationary point, say x_s. Eq. 2.27 is differentiated with respect to x:

$$\partial \hat{y} / \partial x = b + 2\hat{B}x \tag{2.29}$$

Setting the derivative equal to 0, one can solve for the stationary point of the system:

$$x_s = -\frac{1}{2}\hat{B}^{-1} b \tag{2.30}$$

The predicted response at the stationary point is

$$\begin{aligned} \hat{y}_s &= b_0 + x'_s b + x'_s \hat{B} x_s \\ &= b_0 + \frac{1}{2} x'_s b \end{aligned} \tag{2.31}$$

The nature of the stationary point is determined from the signs of the eigenvalues of the matrix $\hat{B}$. If the eigenvalues are all negative, then the stationary point is a point of maximum response. If they are all positive, the stationary point is a point of minimum response. If they are mixed in sign, the stationary point is a saddle point [124].

2.5.7 Robust Design

The variation, the amount of change or difference from expected results, in key performance characteristics can result in poor product and process quality. In the 1980s, Genichi Taguchi [130,131] introduced new ideas on quality improvement in the United States. He proposed an innovative parameter-design approach for reducing variation in products and process. This methodology was developed for using experimental design, specifically for the following:

i) For designing products or processes so that they are robust to environment conditions.

ii) For designing and developing products so that they are robust to component variation.

iii) For minimizing variability in the output response of a product around a target value.

By robust, we mean that the product or process performs consistently on target and is relatively insensitive to factors that are difficult to control.

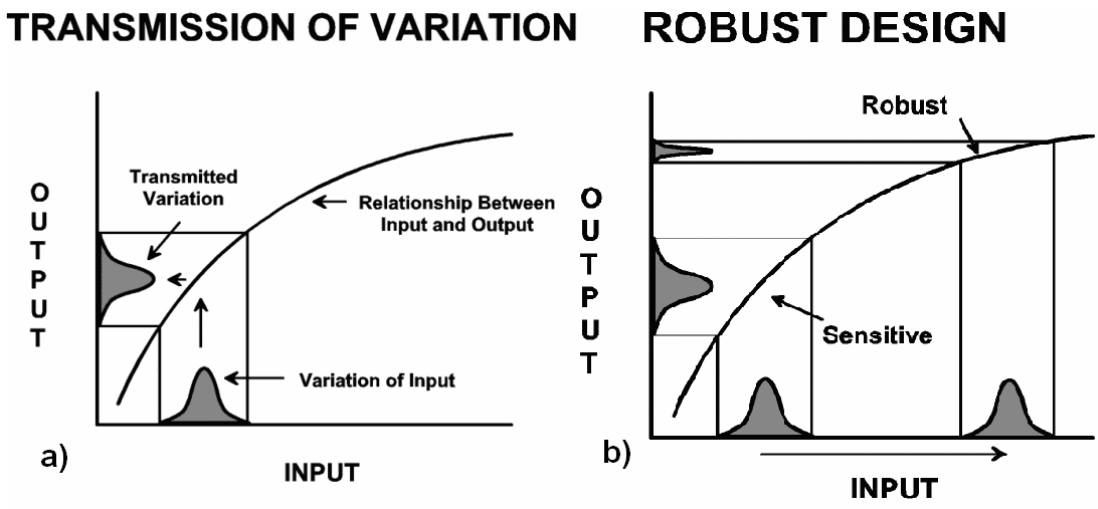

Figure 2.22 a) Transmission of variation. Variation of the output is caused by variation of the inputs. b) Robust design works by selecting targets for the inputs that make the outputs less sensitive (more robust) to the variation of the inputs. The result is less variation and higher quality but without the added costs. [132].

The techniques generated much debate and controversy in the statistical community-not about Taguchi's philosophy, but rather about its implementation and the technical nature of data analysis. As a result, the response surface approach has been suggested as a collection of tools that allow one to adopt Taguchi's robust design concept while providing a more statistically sound and efficient approach to analysis.

Professor Genichi Taguchi used the term robust parameter design (or RPD) to describe his approach to this important class of industrial problems. Essentially, RPD methodology prefers to reduce product or process variation by choosing levels of controllable factors that make the system insensitive (or robust) to changes in a set of uncontrollable factors that represent most of the sources of variability. Taguchi referred to these uncontrollable factors as noise factors. Prior to Taguchi, researchers certainly were aware that certain uncontrollable factors provide major sources of variability. However, Taguchi encouraged the formal use of noise variables in the experimental design and, as a result, allowed the subject of the analysis to involve process variability. We usually assume that these noise factors are uncontrollable in the field, but can be controlled during product or process development for purposes of a designed experiment. As a result, the term robust parameter design entails designing (not in the sense of experimental design) the system (selecting the levels of the controllable variables) so as to achieve robustness (insensitively) to inevitable changes in the noise variables. Often an RPD study in a manufacturing process is called a prpcess robustness study.

A model that contains main effects and interactions involving both control and noise variables, which is the modeling of both x (controllable parameters) and z (uncontrollable parameters) in the same model has been called a response model approach. A response surface for the process mean and a response surface for the process variance is called a dual response surface. A dual response approach to the RPD problem offers specifically:

i) It provides an estimate of the mean and standard deviation at any location on interest in the control design variables.

ii) The engineer or scientist can gain insight regarding the roles of these variables in controlling the process mean and variance.

iii) It provides a ready source of process optimization via the use of a squared error loss criterion.

iv) It allows the use of a wide variety of constrained optimization techniques.

The quadratic response model is

$$y(x,z) = \beta_0 + x'\beta + x'Bx + z'\gamma + x'\Delta z + \varepsilon \tag{2.32}$$

In this model we assume linear effects in x and z, two factor interaction and pure quadratic terms in x (the term x'Bx, and the very important two-factor interactions involving control and noise variables, the term x'Δz).

We assume that in the experiment, the natural levels of z_j are centered at the mean that zj experiences in the process and that the ± 1 level are at $\mu_{z_j} \pm \sigma_{z_j}$. As a result, the mean of the z's in coded metric is at 0 and ± 1 levels are one standard deviation from the mean.

$$\begin{aligned} E(z) &= 0 \\ Var(z) &= \sigma_z{}^2 I_{r_z} \end{aligned} \tag{2.33}$$

The response surface model for the mean is

$$E_z[y(x,z)] = \beta_0 + x'\beta + x'Bx \tag{2.34}$$

The conditional variance operator, $Var_z[y(x,z)]$ plus the error variance around Eq. 2.32 gives

$$Var_z[y(x,z)] = Var_z(\gamma' + x'\Delta)z + \sigma^2 \tag{2.35}$$

Here the quantity $\gamma' + x'\Delta = a'$ is a vector of constants. Rules for applying variance operator give

$$Var_z(a'z) = a'Var(z)a \tag{2.36}$$

where $Var(z) = \sigma_z{}^2 I$ is the variance-covariance matrix of z. As a result we have

$$Var_z[y(x,z)] = \sigma_z^{\,2}(\gamma' + x'\Delta)(\gamma + \Delta' x) + \sigma^2$$
$$= \sigma_z^{\,2} I'(x) I(x) + \sigma^2 \tag{2.37}$$

where

$$I(x) = \gamma + \Delta' x \tag{2.38}$$

$I(x)$ is simply the vector of partial derivatives of y(x,z) with respect to z. In other words,

$$I(x) = \frac{\partial y(x,z)}{\partial z} \tag{2.39}$$

Eq. 2.34 is the response surface for the process mean, while Eq. 2.37 is the response surface for the process variance [124]. Robust design is achieved by optimization of (minimization, maximization or setting the response at a target value) response surface model for the mean (Eq. 2.34) and minimization of variance of the model (Eq. 2.37).

2.5.7.1 Propagation of error (POE). Propagation of error (POE) is used as a mathematical tool for reducing transmitted variance. The variation transmitted to the response can be modeled by taking the partial derivatives of the polynomial with respect to the controllable factors. It is calculated by substituting the variance in the independent factor, the residual variance (noise) and taking the square root.

Using propagation of error adds a new dimension -robust design- to response surface methods. Not only we learn to make the right product (achieve the targets for the responses), we also simultaneously minimize the variation in the product. By making the process more robust to variation in the controllable factors, we improve product quality and reliability [133].

2.5.8 Design-Expert® Software

Design-Expert® Software is a Windows-based program which provides many statistical tools such as two-level factorial screening designs, general factorial studies, Response Surface Methods (RSM), mixture design techniques and combinations of process factors, mixture components and categorical factors [134].

Design Expert makes experimental designs of various techniques and does the numerical optimization of maximum desirability for many responses simultaneously. Design Expert also does robust optimization by reducing the transmitted variance to the response. It offers rotatable 3D plots and 2D contour graphs.

3. MATERIALS AND METHODS

This thesis consists of two main parts. In the first part, optimization of a collimator with typical patient parameters is dealt with. In the second part robust design of the breast scintigraphy collimator is achieved.

The first part is a process made up of a chain of operations which seeks for a typical optimization for the problem domain. The methodology of the typical optimization is explained in the Figure 3.1.

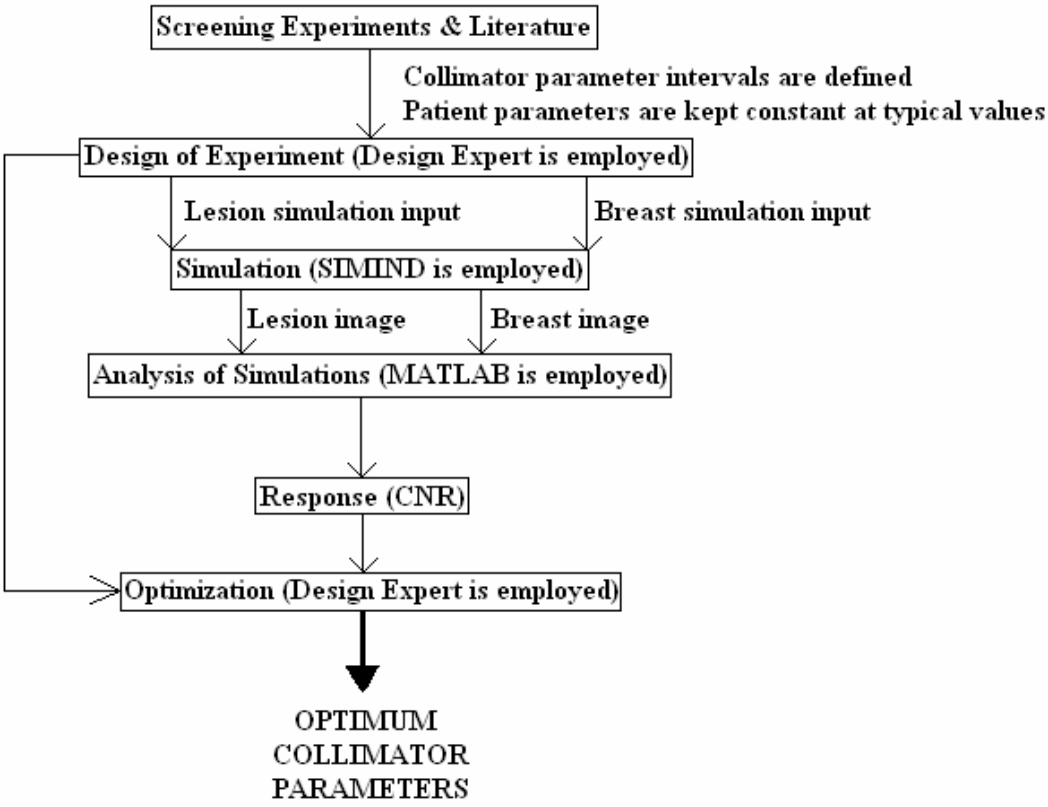

Figure 3.1 Summary of methods and materials used in typical optimization.

For the first part, called typical optimization, the methodology is:

i) Screening experiments: In this part, the effects of collimator parameters (hole length, hole size and septa) on the performance (CNR) are examined. For this purpose, one of the collimator parameters is changed while keeping the others constant. These screening experiments give an idea about the choice of collimator parameter intervals for the Design of Experiments. Also the images gained after each experiment show the change in lesion detectability for different CNR values.

ii) Design of Experiments (DoE): The experiments are designed by using Box-Behnken design method. The intervals for DoE of control variables (collimator parameters) are determined with the help of the screening experiments and the parameters of commercial collimators. Patient parameters are kept constant at their typical values.

iii) Simulations: Breast scintigraphy is simulated via SIMIND with varying collimator parameters created by DoE. For each experiment, two simulations are done; one for lesion phantom and one for breast phantom. In the end of each simulation, a matrix image is created by SIMIND (*.bim file).

iv) Calculation of the response: The output of each simulation is created by superimposing the two separate *.bim files. The response, which is the contrast-to-noise (CNR), is calculated by a MATLAB code for each experiment. This code can also generate the resultant image and a file that shows the distribution of counts of the simulation.

v) Optimization: The independent variables (collimator parameters-hole length, hole size and septal thickness) and the dependent variable (CNR) are computed via a Response Surface Method software (Design Experiment 7.1) to get the optimum collimator parameters.

The second part is an enhanced process composed of a chain of operations which seeks for a robust solution less susceptible to the variations on the breast and lesion parameters.

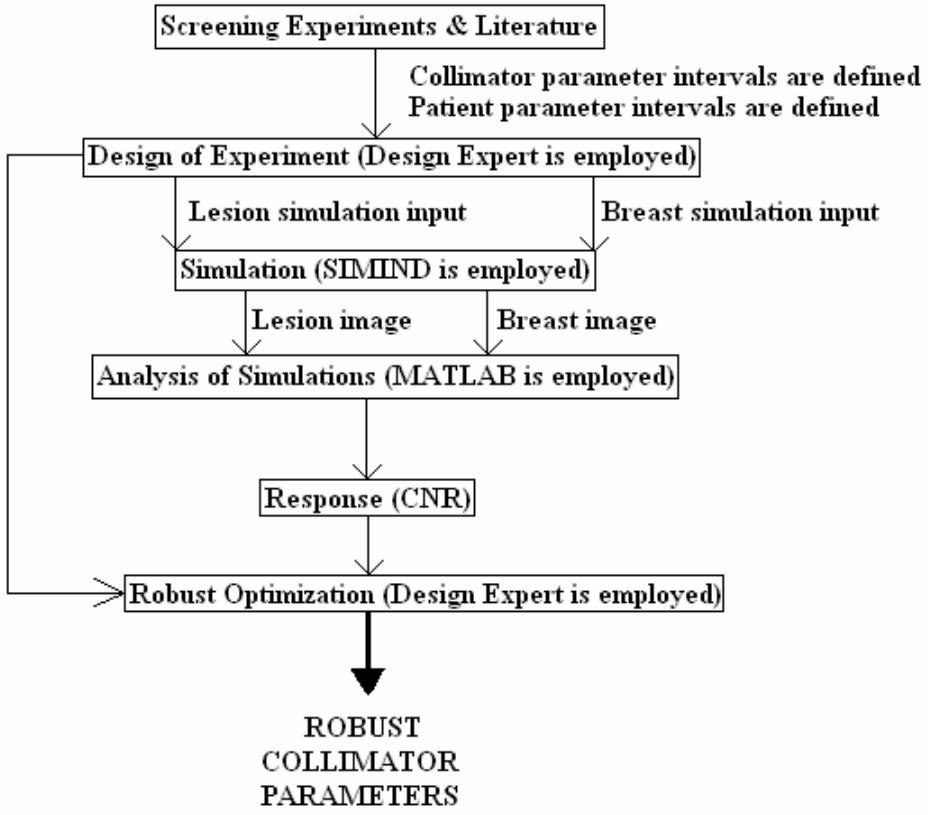

Figure 3.2 Summary of methods and materials used in robust optimization.

For the robust optimization, the methodology is:

i) Screening experiments: In this part, the interaction between controllable factors (collimator parameters-hole length, hole size and septa) and uncontrollable factors (patient parameters-breast diameter, breast thickness, lesion size) are examined. For this purpose, one of the patient parameters is varied while keeping the others constant, so two different phantoms are generated. Then, these two different phantoms are simulated in two different scintigraphy environments: one of the collimator parameters is varied while keeping the other collimator parameters constant.

ii) Design of Experiments (DoE): The experiments are designed by using Box-Behnken design method. The intervals for DoE of control variables (collimator parameters) and noise parameters (patient parameters) are determined with the help

of the screening experiments, the parameters of commercial collimators and typical brast and lesion dimensions.

iii) Simulations: Breast scintigraphy is simulated via SIMIND with varying collimator and patient parameters created by DoE. For each experiment, two simulations are done; one for lesion phantom and one for breast phantom. In the end of each simulation, a matrix image is created by SIMIND (*.bim file).

iv) Calculation of the response: The output of each simulation is created by superimposing the two separate *.bim files. The response, which is the contrast-to-noise (CNR), is calculated by a MATLAB code for each experiment. This code can also generate the resultant image and a file that shows the distribution of counts of the simulation.

v) Robust optimization: The independent variables (collimator parameters-hole length, hole size and septal thickness and patient parameters-breast diameter, breast thickness and lesion diameter), and the dependent variable (CNR) are computed via a Response Surface Method software (Design Experiment 7.1) to get the robust collimator parameters.

3.1 Model of the Breast and the Lesion

The breast is modeled as a cylinder filled with ^{99m}Tc with a density of 100μCi/cc which has the dimensions of 6cm height and 10cm diameter. And the lesion is modeled as a sphere located at the center of the cylinder breast model. The lesion is assumed to be composed of ^{99m}Tc with a density of 564μCi/cc and have a diameter of 0.6cm. The reason why this Tc-99m concentration ratio (5.64:1) is used for the breast and the lesion models is, the studies showing that the typical radioactivity ratio of malignant lesion to the radioactivity of the breast tissue is of this measure [135].

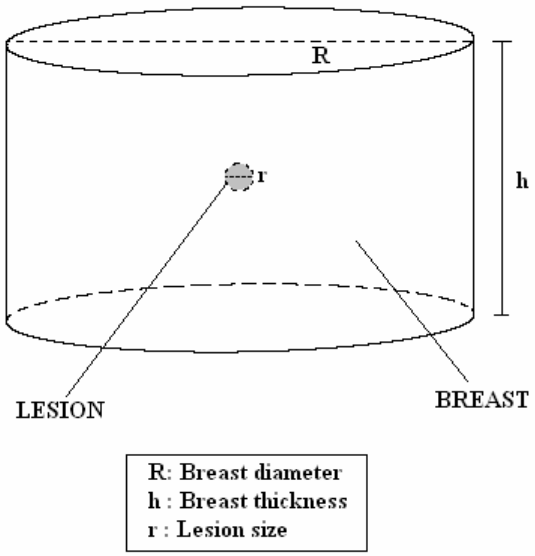

Figure 3.3 Model of the phantom.

In this study, breast and lesion sizes are selected by judgmental sampling and they are conformable with literature. The cylindrical breast geometry with diameters ranging from 6 to 16cm, which span the range of breast sizes that probably would be encountered clinically [136]. Scintimammographic images were acquired in the axial view; each breast was compressed to a thickness of 3-6cm [137]. This mild compression improves lesion contrast and background uniformity by minimizing breast thickness and providing a constant column height of tissue over the collimator [138]. The average lesion, which has a size of 2.1cm [139] is big enough to be observed via gamma camera with any low energy high resolution collimator (Figure 3.4). For this reason, a lesion with size of 0.6cm, which is smaller than 1cm, is selected in this study because of its challenging lesion detectability.

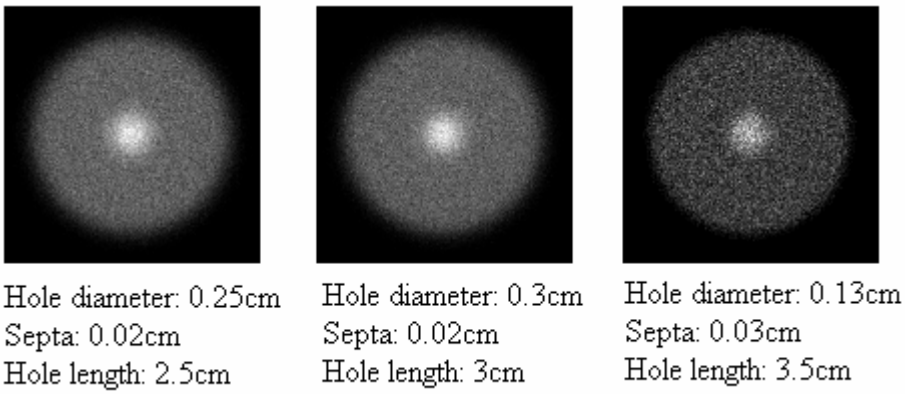

Figure 3.4 Images of a 2.1cm diameter lesion with various collimator configurations.

In the first part of the study, this phantom with these typical values is used. For the second part, where patient variation is taken into account, a standard deviation of 1.34cm is added to the breast diameter. The breast thickness and lesion size is varied at a standard deviation of 0.67cm and 0.067cm respectively.

3.2 Methods for Typical Optimization

3.2.1 Screening Experiments

Screening experiments are one of the powerful steps of Design of Experiments techniques that give useful opinions about the parameters that affect the performance of the analyzed system response. Before the construction of experiment design, a few experiments are done to observe how the output responds to the changes in input parameters.

As the gamma camera for breast scintigraphy should be equipped with a low-energy, high-resolution collimator; the commercial collimator parameters have been investigated. As a result, hole diameter seems to be in in the range of 0.15cm to 0.30cm;

septal thickness ranges from 0.02cm to 0.03cm; and hole length ranges from 2.00cm to 5.00cm [140].

In this stage of the study, to investigate the influences of changes in collimator parameters to the system response CNR, which represents lesion detectability concept, screening experiments are implemented. For this purpose, one of the collimator parameter is varied inside an interval that covers typical range (with a realistic approach seeking for manufacturable range), while the other two are kept constant at normal values. By this way, the stand alone effects of the parameters on CNR are studied. Phantom parameters are kept constant: breast diameter is 10cm, breast thickness is 6cm and lesion diameter is 0.6cm.

3.2.1.1 Hole length. In order to see the effect of hole length change on CNR, six experiment points are selected (Table 3.1). Hole size and septal thickness are kept at 0.2cm and 0.02cm respectively.

Table 3.1
Screening experiment of hole length.

Experiment no	Hole Length(cm)	CNR
1	1.00	15.6741
2	1.25	16.4396
3	1.50	16.6467
4	2.00	15.8508
5	3.00	12.9417
6	4.00	10.6478

These experiments are accomplished by SIMIND and the results are shown in the last column of the Table 3.1. The change in hole length vs CNR is shown in Figure 3.5.

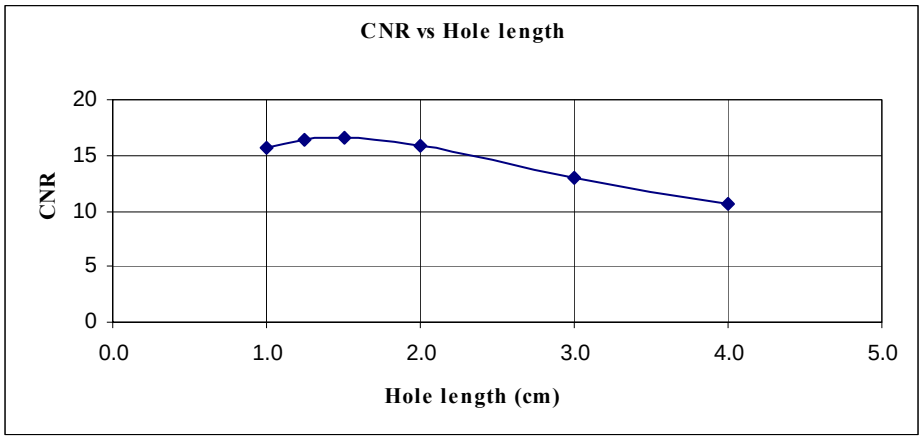

Figure 3.5 Relationship between hole length and CNR.

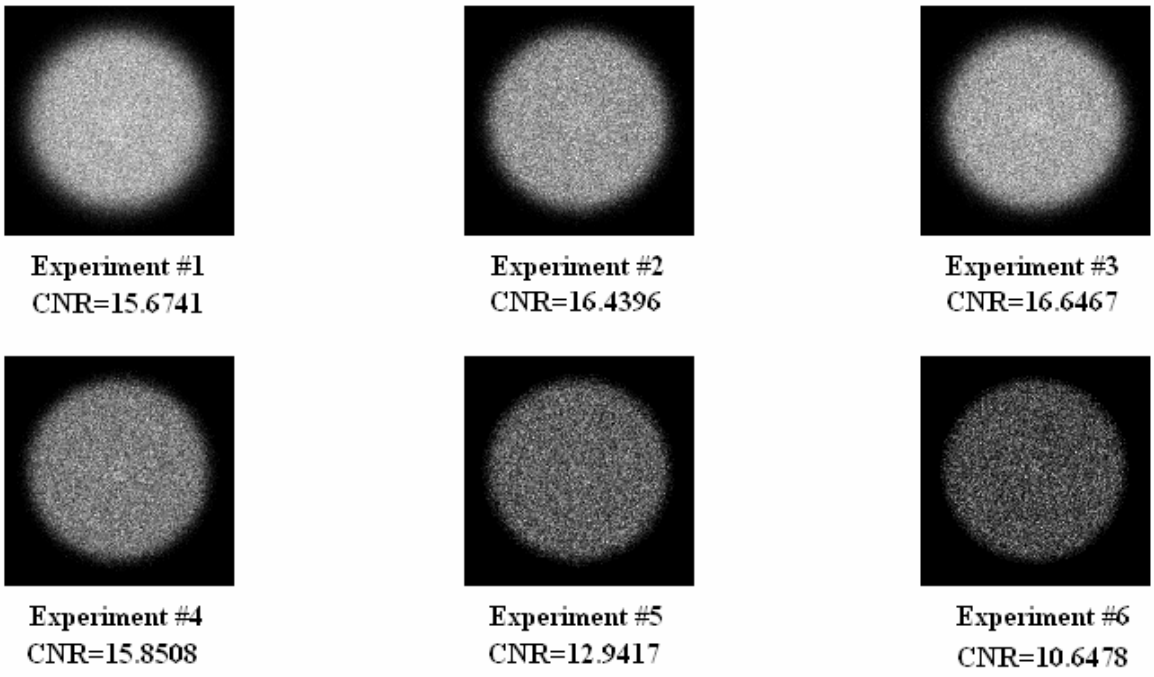

Figure 3.6 Images of screening experiments showing the relation between hole length and CNR.

It can easily be observed that this interval of 1cm to 4 cm hole length can give a reasonable experiment range for the study. Since a peak point can be seen from the graph (Figure 3.5), an optimum hole length can be searched in this interval. In Figure 3.6, the resultant images of each experiment are seen. The third experiment, which has the best CNR value of 16.6467, gives the best lesion detectability.

3.2.1.2 Hole Size. In order to see the effect of hole length change on CNR, six experiment points are selected (Table 3.2). Hole length and septal thickness are kept at 2.5cm and 0.02cm respectively.

Table 3.2
Screening experiment of hole size.

Experiment No	Hole Size (cm)	CNR
1	0.10	18.3336
2	0.15	18.5723
3	0.20	16.9592
4	0.30	13.4571
5	0.40	10.6264
6	0.50	08.9709

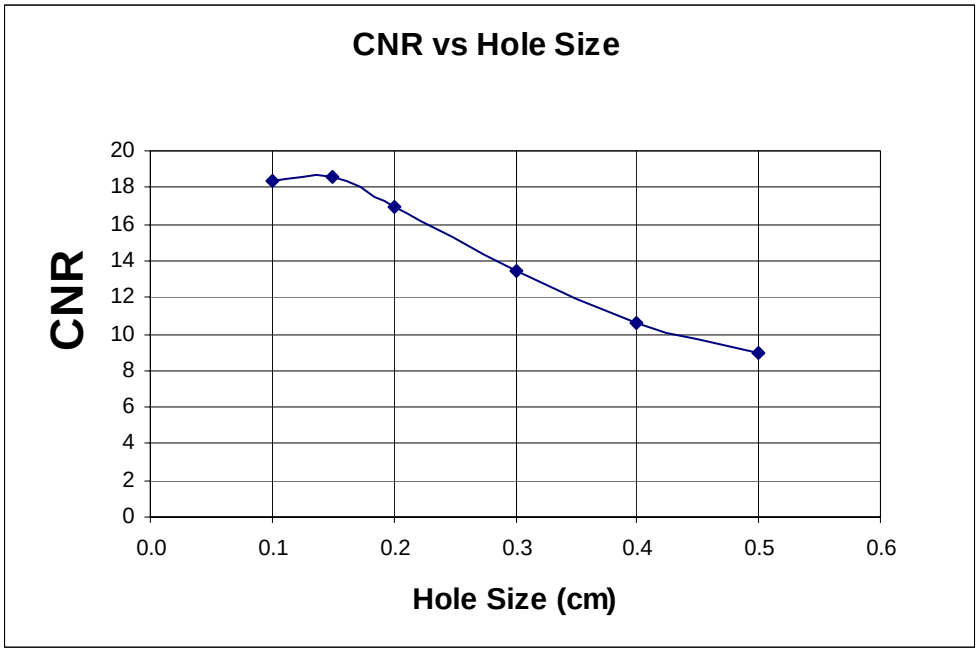

Figure 3.7 Relationship between hole size and CNR.

These experiments are accomplished by SIMIND and the results are shown in the last column of the Table 3.2. The change in hole size vs CNR is shown in Figure 3.7.

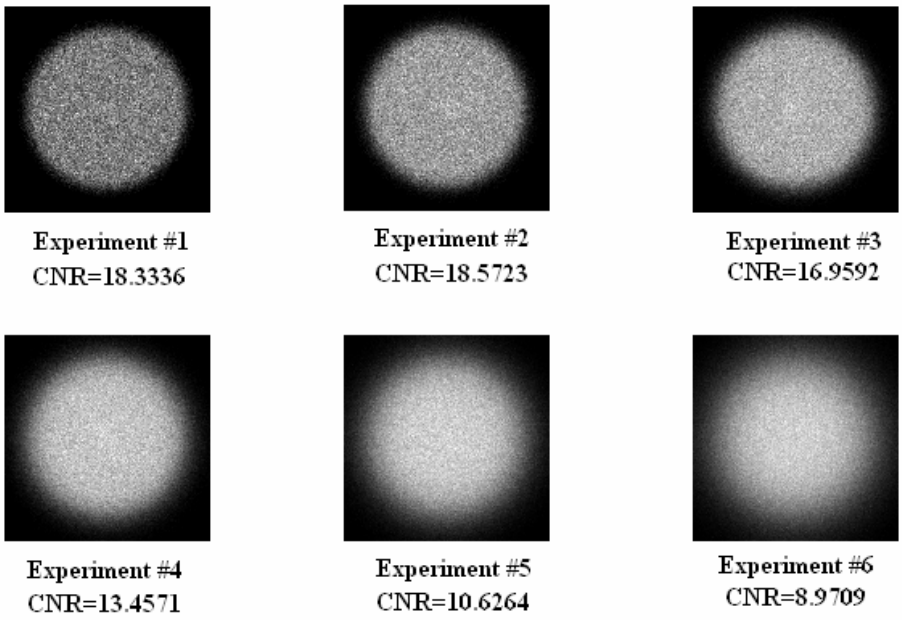

Figure 3.8 Images of screening experiments showing the relation between hole size and CNR.

It can easily be observed that this interval of 0.1cm to 0.5 cm hole size can give a reasonable experiment range for the study. Since a peak point can be seen from the graph (Figure 3.7), an optimum hole length can be searched in this interval. Also, in Figure 3.8, we can see that there is a good correlation between CNR and lesion detectability.

3.2.1.3 Septal thickness. In order to see the effect of septal thickness change on CNR, six experiment points are selected (Table 3.3). Hole length and hole size are kept at 2.5cm and 0.2cm respectively.

Table 3.3
Screening experiment of septal thickness.

Experiment No	Septal Thickness (cm)	CNR
1	0.005	16.6781
2	0.008	16.7631
3	0.010	16.5770
4	0.020	15.7609
5	0.030	14.9187
6	0.050	13.4603

These experiments are accomplished by SIMIND and the results are shown in the last column of the Table 3.3. The change in septal thickness vs CNR is shown in Figure 3.9.

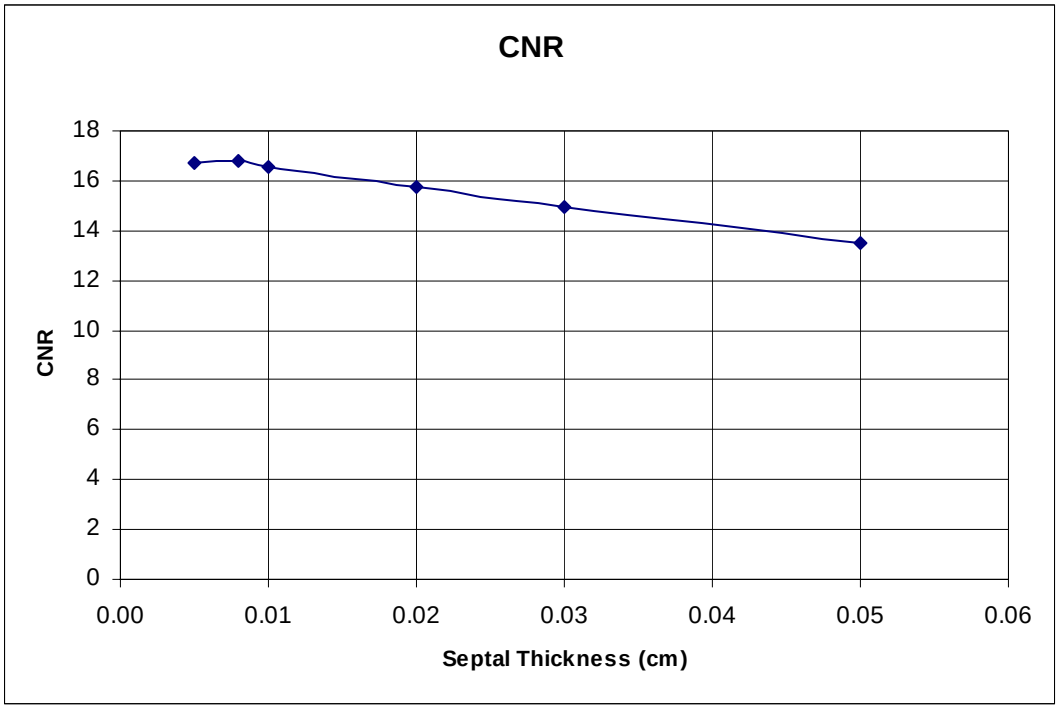

Figure 3.9 Relationship between septal thickness and CNR.

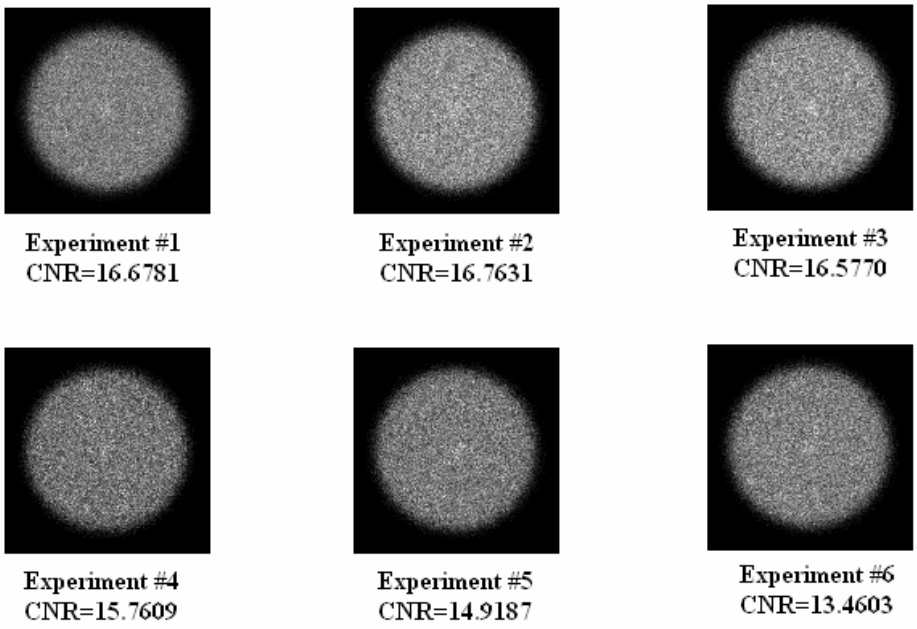

Figure 3.10 Images of screening experiments showing the septal thickness and CNR relation.

It can easily be observed that this interval of 0.005cm to 0.05 cm septal thickness can gives a proper experiment range for the study. Since a peak point can be seen from the graph (Figure 3.9), an optimum hole length can ben searched in this interval.

3.2.2 Design of Experiments of Typical Optimization

The standalone effects of collimator parameters are examined by screening experiments and with the sense of their results, experiment set needed for understanding the collimator parameters interaction and the effects of these interactions to the response is prepared by using Box-Behnken Method. Designs include only three levels of each factor, which makes this method appealing because of the reduced number of experiments. Also, the negative experiment points coming from Central Composite Design, which are not applicable for this study, are eliminated by this method.

For Box Behnken design, the number of factors is chosen as 3 (Hole length, Septal thickness and Hole size). The low and high levels, which define the intervals for each factor, are entered as in Table 3.4.

Table 3.4
Design intervals of collimator parameters for typical optimization problem.

Name	Units	-1 Level	1 Level
Hole Length	cm	1	4
Septal Thickness	cm	0.005	0.05
Hole Size	cm	0.1	0.5

Design Expert calculates the center level for the design and creates a table of experiment inputs (Table 3.5).

Table 3.5
Design of Experiments for typical optimization problem.

Experiment No	Hole Length	Septa	Hole Size
1	1	0.005	0.3
2	4	0.005	0.3
3	1	0.05	0.3
4	4	0.05	0.3
5	1	0.0275	0.1
6	4	0.0275	0.1
7	1	0.0275	0.5
8	4	0.0275	0.5
9	2.5	0.005	0.1
10	2.5	0.05	0.1
11	2.5	0.005	0.5
12	2.5	0.05	0.5
13	2.5	0.0275	0.3
14	2.5	0.0275	0.3
15	2.5	0.0275	0.3
16	2.5	0.0275	0.3
17	2.5	0.0275	0.3

3.2.3 Simulations of Typical Optimization

Once the experiment set is built by Design Expert using Box-Behnken Design Technique, these experiments (simulations) are achieved by a Monte Carlo Simulation program called SIMIND. Two different simulations are accomplished for each experiment; one for lesion, and one for breast source. Then, these two simulated images are superimposed by MATLAB. So, for the typical optimization problem, we have made a total of 34 experiments.

Simulation parameters of breast are:

Photon energy:	140 keV (99mTc)
Energy resolution:	10.6% at 140 keV
Intrinsic resolution:	0.380cm
Crystal length:	40cm
Crystal width:	50cm
Crystal thickness:	0.935cm
Source dimensions:	10x10x6cm (Cylinder)
Phantom dimensions:	10x10x6cm (Cylinder)
Source activity:	1742.7 MBq
Source to camera distance:	4 cm (from the center of the phantom)
Energy window:	10% (126 keV–154keV)
Pixel size:	0.1 cm
Image matrix size:	128x128
Collimator Hole Shape:	Hexagonal
Simulated photons:	1000000
Simulation time:	600sec

Simulation parameters of lesion are:

Photon energy:	140 keV (99mTc)
Energy resolution:	10.6% at 140 keV
Intrinsic resolution:	0.380cm
Crystal length:	40cm
Crystal width:	50cm
Crystal thickness:	0.935cm
Source dimensions:	0.6x0.6x0.6cm (Sphere)
Phantom dimensions:	10x10x6cm (Cylinder)
Source activity:	2.36 MBq
Source to camera distance:	4 cm (from the center of the phantom)
Energy window:	10% (126keV-154keV)
Pixel size:	0.1 cm
Image matrix size:	128x128
Collimator Hole Shape:	Hexagonal
Simulated photons:	1000000
Simulation time:	600sec

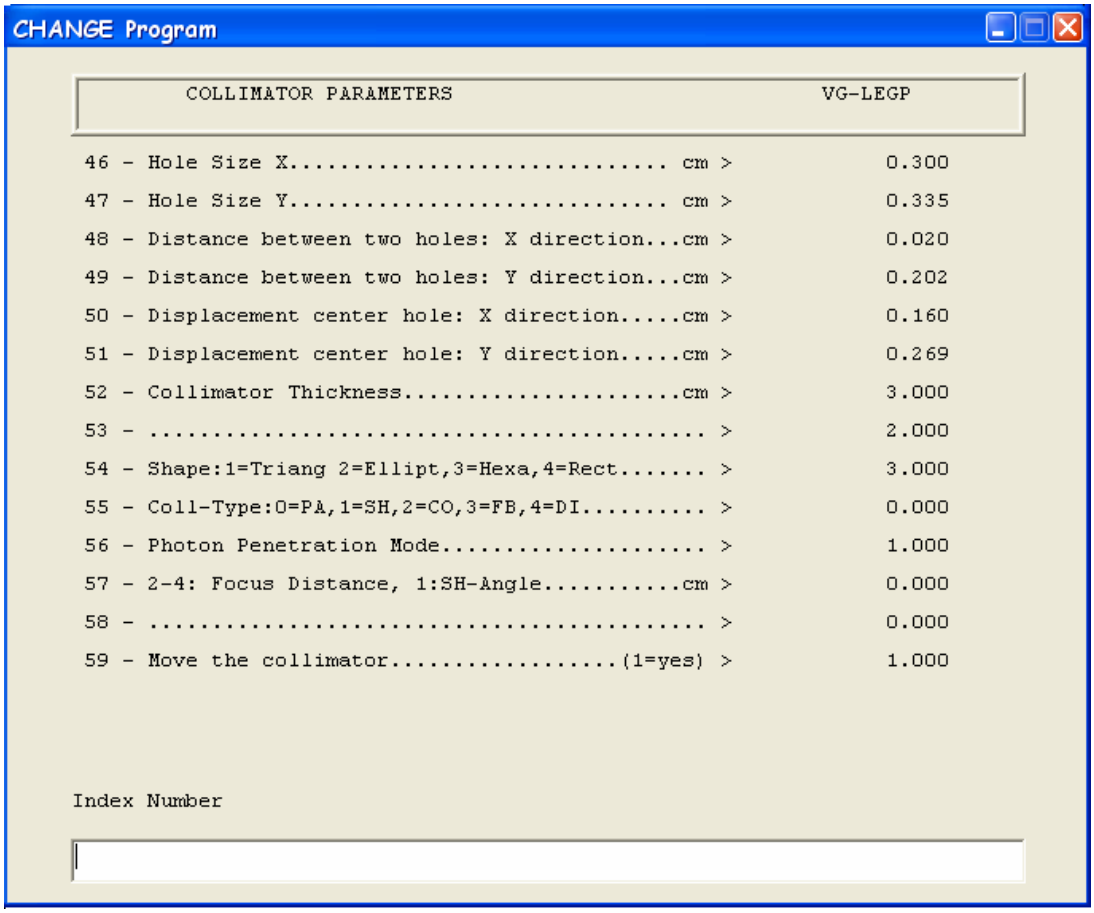

Figure 3.11 SIMIND screenshot. Collimator parameters can be changed from the 'Collimator Parameters' page.

Simulation duration for one experiment was approximately 10 minutes. After each simulation, SIMIND gives a BIM output which is very simple 'image', based on keyboard character, of the matrix together with calculated data and a two row data of a profile through the matrix [141].

3.2.4 Analysis of Simulations and Getting the Responses

CNR (Contrast-to-Noise Ratio) is selected as a measure of the image quality and lesion detectability in this study. CNR is calculated by a MATLAB code from the output files of lesion and breast simulation. This code takes the *.bim files as inputs and gives the CNR value and the resultant image file (as a Matlab figure file *.fig). The CNR values

achieved by the application of the Matlab code are in Table 3.6 and design summary is shown in Table 3.7.

Table 3.6
Experiment results of typical optimization problem.

Experiment No	Hole Length	Septa	Hole Size	CNR
1	1	0.005	0.3	8.3836
2	4	0.005	0.3	13.6448
3	1	0.05	0.3	10.3194
4	4	0.05	0.3	12.6169
5	1	0.0275	0.1	15.6922
6	4	0.0275	0.1	7.0826
7	1	0.0275	0.5	7.2726
8	4	0.0275	0.5	12.0792
9	2.5	0.005	0.1	12.8722
10	2.5	0.05	0.1	8.9139
11	2.5	0.005	0.5	8.9348
12	2.5	0.05	0.5	11.2836
13	2.5	0.0275	0.3	14.5619
14	2.5	0.0275	0.3	14.3786
15	2.5	0.0275	0.3	14.4504
16	2.5	0.0275	0.3	14.3627
17	2.5	0.0275	0.3	14.401

Table 3.7
Design summary of typical optimization problem.

					Study Type	Response Surface	
					Initial Design	Box-Behnken	
					Design Model	Quadratic	
					Runs	17	
					Blocks	No Blocks	
Factor	**Name**	**Low Actual**	**High Actual**	**Low Coded**	**High Coded**	**Mean**	**Std. Dev.**
A	Hole Length	1	4	-1	1	2.5	1.0289915
B	Septa	0.005	0.05	-1	1	0.0275	0.0154349
C	Hole Size	0.1	0.5	-1	1	0.3	0.1371989
Response	**Name**	**Analysis**	**Min**	**Max**	**Mean**	**Std. Dev.**	**Ratio**
Y1	SNR	Polynomial	7.0826	15.6922	11.8382588	2.74909	2.2155988

3.2.5 RSM Analysis of Typical Optimization Problem

Analysis of the experimental data and optimization process is carried out by Design Expert software. Clicking on the Fit Summary button starts the regression calculations to fit all of the polynomial models to the selected response.

The program calculates the effects for all model terms. It produces statistics such as p-values, lack of fit and R-squared values for comparing the models (Table 3.8). If a statistically significant model is detected, the program will underline and note the "Suggested" model. This becomes the default model on the Model screen.

Table 3.8
Regression calculations of fitting all the models to CNR. All of the tests suggest a quadratic model.

Response:	CNR		**Transform:**	None		
Sequential Model Sum of Squares [Type I]						
Source	**Sum of Squares**	**df**	**Mean Square**	**F Value**	**p-value Prob>F**	
Mean vs Total	2382.454	1	2382.4543			
Linear vs Mean	4.938076	3	1.6460255	0.1732101	0.9126	
2FI vs Linear	57.13936	3	19.046454	2.868425	0.0900	
Quadratic vs 2FI	49.01611	3	16.338703	6.5789853	0.0191	Suggested
Cubic vs Quadratic	17.35846	3	5.7861528	896.32102	< 0.0001	Aliased
Residual	0.025822	4	0.0064554			
Total	2510.932	17	147.70189			
Lack of Fit Tests						
Source	**Sum of Squares**	**df**	**Mean Square**	**F Value**	**p-value Prob>F**	
Linear	123.5139	9	13.72377	2125.921	< 0.0001	
2FI	66.37457	6	11.062428	1713.658	< 0.0001	
Quadratic	17.35846	3	5.7861528	896.32102	< 0.0001	Suggested
Cubic	0	0				Aliased
Pure Error	0.025822	4	0.0064554			
Model Summary Statistics						
Source	**Std. Dev.**	**R-Squared**	**Adjusted R-Squared**	**Predicted R-Squared**	**PRESS**	
Linear	3.082703	0.0384352	-0.183464	-0.760335	226.1641	
2FI	2.576827	0.4831763	0.173082	-0.60581	206.3109	
Quadratic	1.575902	0.8646904	0.690721	-1.162051	277.7757	Suggested
Cubic	0.080346	0.999799	0.9991961		+	Aliased

In Table 3.8, we have looked for:

i) The highest order model that is significant (P-value small) and not aliased.

ii) No lack of fit (P-value > 0.10)

iii) Reasonable agreement between Adjusted R-squared and Predicted R-squared (within 0.2 of each other).

From the analysis of regression models, it is proper to fit a second order (quadratic) model for our data. Since all of the collimator parameters and their dual interactions are

significant, all of them are taken into account to form the model. ANOVA report and the regression model is as follows:

Table 3.9
ANOVA (Analysis of variance) table for the quadratic model of typical optimization problem.

ANOVA for Response Surface Quadratic Model						
Analysis of variance table [Partial sum of squares - Type III]						
Source	**Sum of Squares**	**df**	**Mean Square**	**F Value**	**p-value Prob > F**	
Model	111.0935492	9	12.343728	4.97035785	0.0231	
A-Hole Length	1.7631603	1	1.76316	0.709959	0.4273	
B-Septal Thickness	0.0615303	1	0.06153	0.024776	0.8794	
C-Hole Size	3.1133858	1	3.11339	1.253644	0.2998	
AB	2.1958794	1	2.19588	0.884199	0.3784	
AC	44.998606	1	44.9986	18.11926	0.0038	
BC	9.9448776	1	9.94488	4.004431	0.0855	
A^2	10.505969	1	10.506	4.230361	0.0787	
B^2	10.915936	1	10.9159	4.395439	0.0743	
C^2	22.656095	1	22.6561	9.122763	0.0194	
Residual	0,664638	7	0,128363			
Lack of Fit	0,647519	3	0,21584	50,43	0,001233	
Pure Error	1,71E-02	4	4,28E-03			
Cor Total	128.4778295	16				
Std. Dev.	1.575902474		**R-Squared**	0.86469043		
Mean	11.83825882		**Adj R-Squared**	0.69072098		
C.V. %	13.31194475		**Pred R-Squared**	-1.1620515		
PRESS	277.775682		**Adeq Precision**	6.90566911		
Factor	**Coefficient Estimate**	**df**	**Standard Error**	**95% CI Low**	**95% CI High**	**VIF**
Intercept	14.43092	1	0.704765	12.7644156	16.09742	
A-Hole Length	0.4694625	1	0.5571657	-0.8480249	1.78695	1
B-Septal Thickness	-0.0877	1	0.5571657	-1.4051874	1.229787	1
C-Hole Size	-0.6238375	1	0.5571657	-1.9413249	0.69365	1
AB	-0.740925	1	0.7879512	-2.6041336	1.122284	1
AC	3.35405	1	0.7879512	1.49084143	5.217259	1
BC	1.576775	1	0.7879512	-0.2864336	3.439984	1
A^2	-1.57961	1	0.7679999	-3.3956411	0.236421	1.0058824
B^2	-1.610135	1	0.7679999	-3.4261661	0.205896	1.0058824
C^2	-2.31966	1	0.7679999	-4.1356911	-0.50363	1.0058824

Final Equation in Terms of Coded Factors:	
CNR	=
14.43092	
0.4694625	* A
-0.0877	* B
-0.6238375	* C
-0.740925	* A * B
3.35405	* A * C
1.576775	* B * C
-1.57961	* A^2
-1.610135	* B^2
-2.31966	* C^2
Final Equation in Terms of Actual Factors:	
CNR	=
12.44571119	
1.072886111	* Hole Length
120.7954691	* Septal Thickness
-5.910551389	* Hole Size
-21.95333333	* Hole Length * Septal Thickness
11.18016667	* Hole Length * Hole Size
350.3944444	* Septal Thickness * Hole Size
-0.702048889	* Hole Length^2
-3180.51358	* Septal Thickness^2
-57.9915	* Hole Size^2

From the ANOVA table (Table 3.9), we can drive some ideas about our model and its adequacy. If the Prob>F value of the model is very small (less than 0.05) then the terms in the model have a significant effect on the response. With a model Prob>F value of 0.0231, one can say that this model is sufficient to represent the relationship between collimator variables and CNR. Also if the Prob>F value is very small (less than 0.05) then the individual terms in the model have a significant effect on the response. The term AC and C^2 with Prob>F values 0.0038 and 0.0194 are the most significant terms.

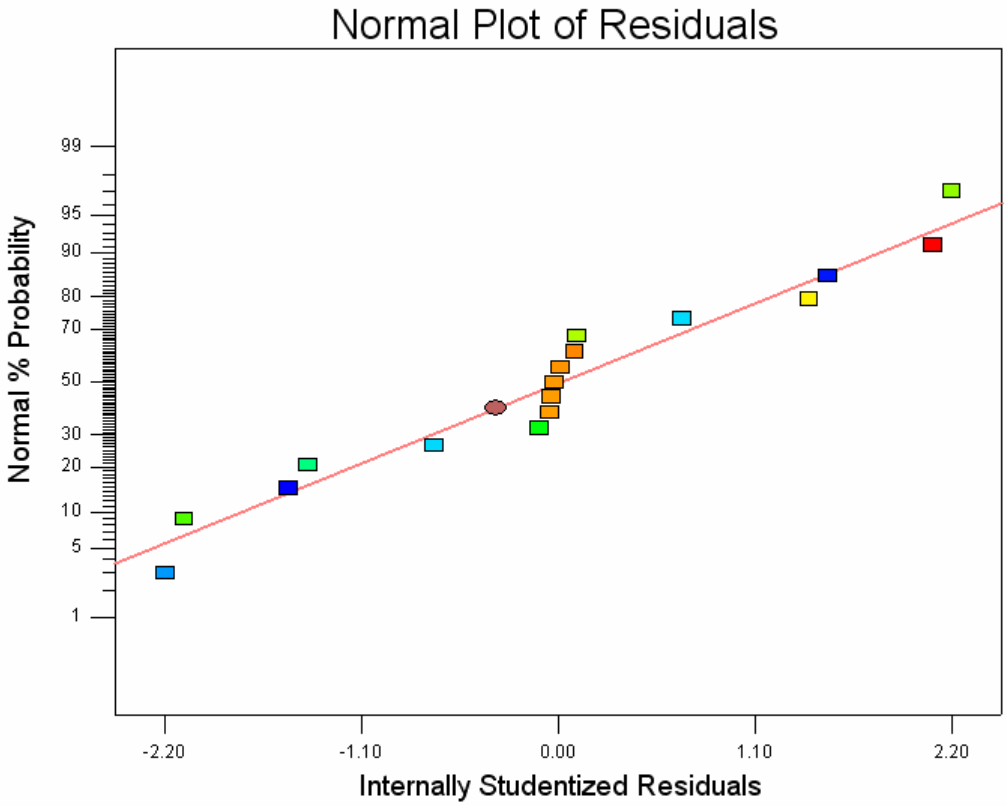

Figure 3.12 Normal plot of residuals (typical optimization problem).

The normal probability plot indicates whether the residuals follow a normal distribution, in which case the points will follow a straight line. Some moderate scatter is expected even with normal data. In (Figure 3.12), a scatter is observed through the straight line, but it is quite normal.

3.3 Methods for Robust Optimization

3.3.1 Screening Experiments

The control and noise interactions are vitally important for robust design in order to model the variance reflection of noise variables to the system response. Indeed, the

structure of these interactions determines the nature of nonhomogeneity of process variance that characterizes the parameter design problem.

Dispersion effects are effects that have influence on the process variance whereas location effects have an effect on the process mean. Slopes of these interactions plots are very important for searching these effects. In the interaction plots are parallel; one can conclude that the noise variable has no dispersion effect than there is no robust parameter design problem. In this stage of the study, the collimator parameters x noise parameters interactions are investigated one by one in order to find if they are dispersion effects or if they have location effects.

3.3.1.1 Collimator parameters and breast diameter interactions.

Hole length

Hole size is kept constant at 0.25cm and septal thickness is 0.02cm. Breast thickness and lesion size are 4cm and 0.6cm, respectively. Hole length is varied between 2cm and 4cm while breast diameter of 8cm and 11cm are tested.

Table 3.10
Screening experiment design for understanding the interaction between hole length and breast diameter.

Hole length (cm)	Breast diameter (cm)	CNR
2	8	12.5996
2	11	11.8395
4	8	11.8107
4	11	11.2602

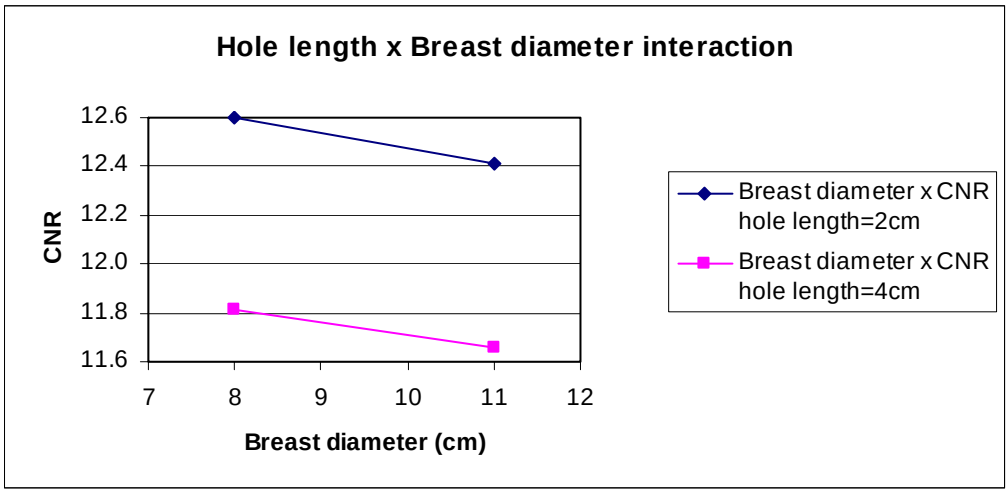

Figure 3.13 Graph showing the interaction between hole length and breast diameter.

Slope is -0.25 for hole length of 2cm, and -0.27 for hole length of 4cm. As a result, since there is a little difference between the slopes, one can say that altering hole length has a little effect on the variance produced by changing the noise variable breast diameter. Then, breast diameter x hole length interaction is very poor.

Hole size

Hole length is kept constant at 2.5cm and septal thickness is 0.02cm. Breast thickness and lesion size are 4cm and 0.6cm, respectively. Hole size is varied between 0.2cm and 0.4cm while breast diameter of 8cm and 11cm are tested.

Table 3.11
Screening experiment design for understanding the interaction between hole size and breast diameter.

Hole size (cm)	Breast diameter (cm)	CNR
0.2	8	13.2453
0.2	11	13.1156
0.4	8	10.5749
0.4	11	10.3158

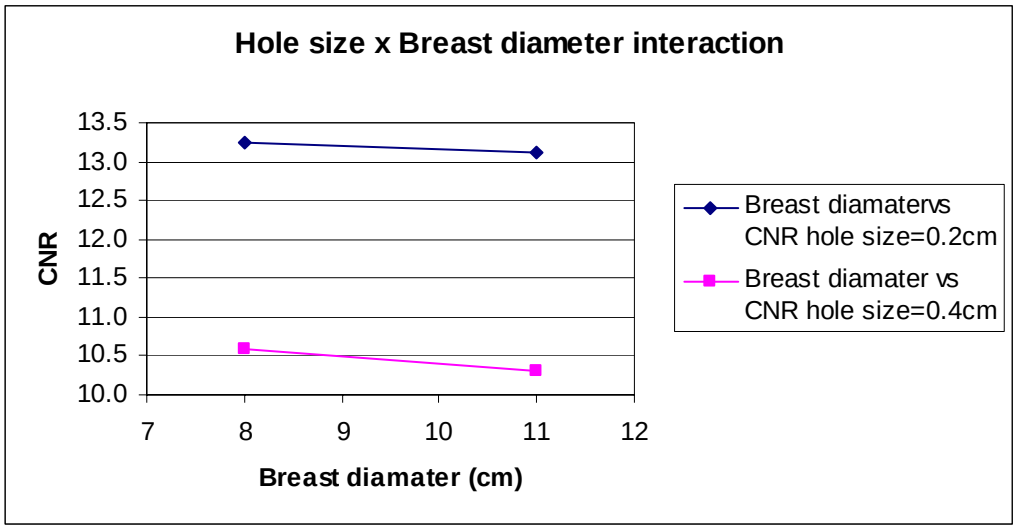

Figure 3.14 Graph showing the interaction between hole size and breast diameter.

Slope is -0.04 for hole size of 0.2cm, and -0.08 for hole size of 0.4cm. As a result, since there is a little difference between the slopes, one can say that altering hole size has a little effect on the variance produced by changing the noise variable breast diameter. There is a little dispersion effect of breast diameter on CNR. When Figure 3.14 is compared with Figure 3.13, we can see that hole size has a greater location effect that hole length on the system response.

Septal thickness

Hole length is kept constant at 2.5cm and hole size is 0.25cm. Breast thickness and lesion size are 4cm and 0.6cm, respectively. Septal thickness is varied between 0.01cm and 0.03cm while breast diameter of 8cm and 11cm are tested.

Table 3.12
Screening experiment design for understanding the interaction between septal thickness and breast diameter.

Septal thickness (cm)	Breast diameter (cm)	CNR
0.01	8	12.8982
0.01	11	12.6639
0.03	8	11.6934
0.03	11	12.1859

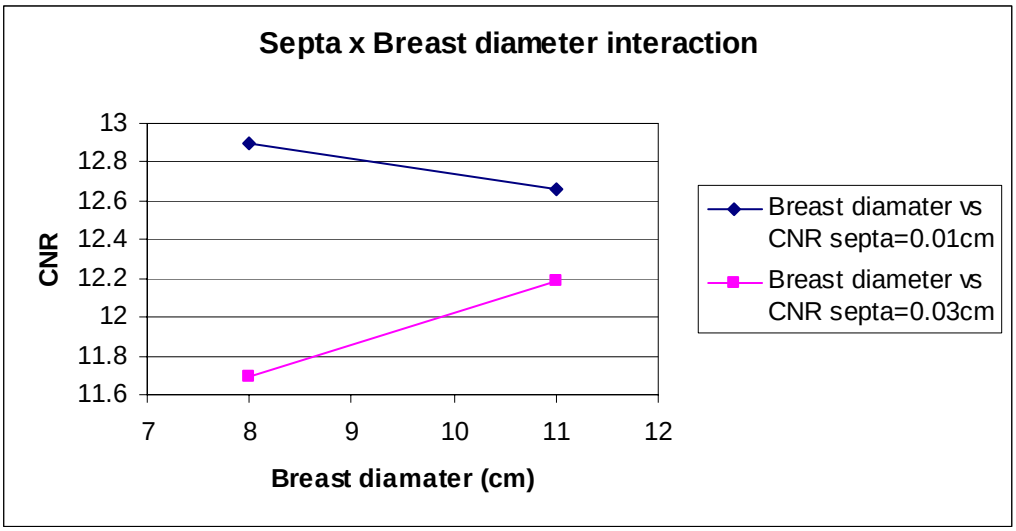

Figure 3.15 Graph showing the interaction between septal thickness and breast diameter.

Slope is -0.078 for septal thickness of 0.01cm, and 0.16 for septal thickness of 0.03cm. These different signed slopes show that septal breast diameter has both dispersion and location effect on CNR. The use of 0.01cm or 0.03cm septal thickness results in process variance. There may be other levels of septal thickness that will produce a less variance associated with changes in breast diameter.

3.3.1.2 Collimator parameters and breast thickness interactions.

Hole length

Hole size is kept constant at 0.25cm and septal thickness is 0.02cm. Breast diameter and lesion size are 8cm and 0.6cm, respectively. Hole length is varied between 2cm and 4cm while breast thickness of 4cm and 8cm are tested.

Table 3.13
Screening experiment design for understanding the interaction between hole length and breast thickness.

Hole length (cm)	Breast thickness (cm)	CNR
2	4	27.7942
2	8	11.8917
4	4	24.3894
4	8	11.8651

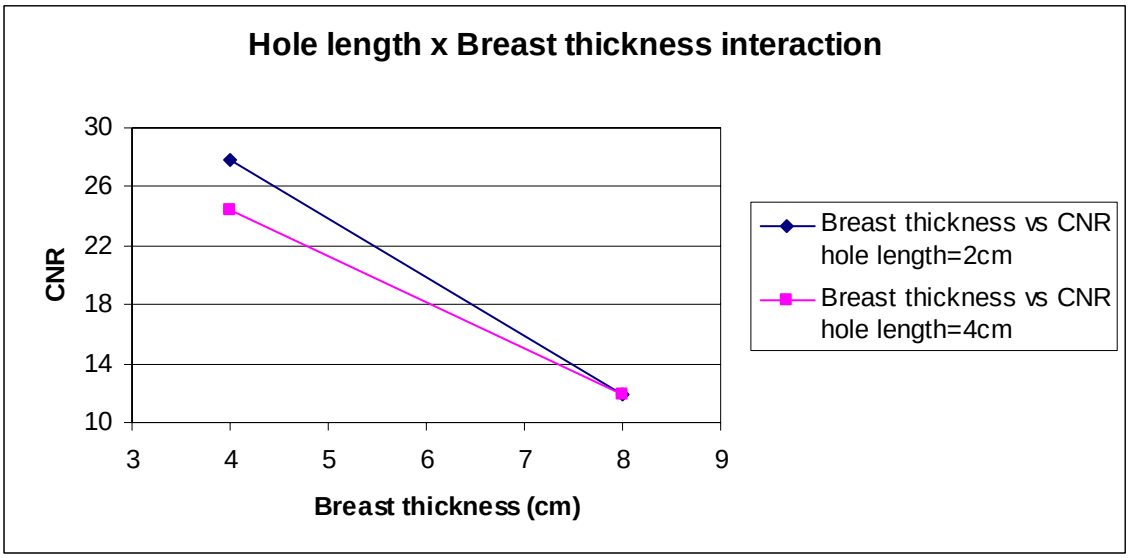

Figure 3.16 Graph showing the interaction between hole length and breast thickness.

Slope is -3.97 for hole length of 2cm, and -3.13 for hole length of 4cm. Since hole length of 4cm creates less variance on CNR than 2cm hole length does, one can say that breast thickness has dispersion effects and using a proper hole length can reduce these effects.

Hole size

Hole length is kept constant at 2.5cm and septal thickness is 0.02cm. Breast diameter and lesion size are 8cm and 0.6cm respectively. Hole size is varied between 0.2cm and 0.4cm while breast thickness of 4cm and 8cm are tested.

Table 3.14
Screening experiment design for understanding the interaction between hole size and breast thickness.

Hole size (cm)	Breast Thickness (cm)	CNR
0.2	4	28.0382
0.2	8	12.9771
0.4	4	23.3121
0.4	8	9.9064

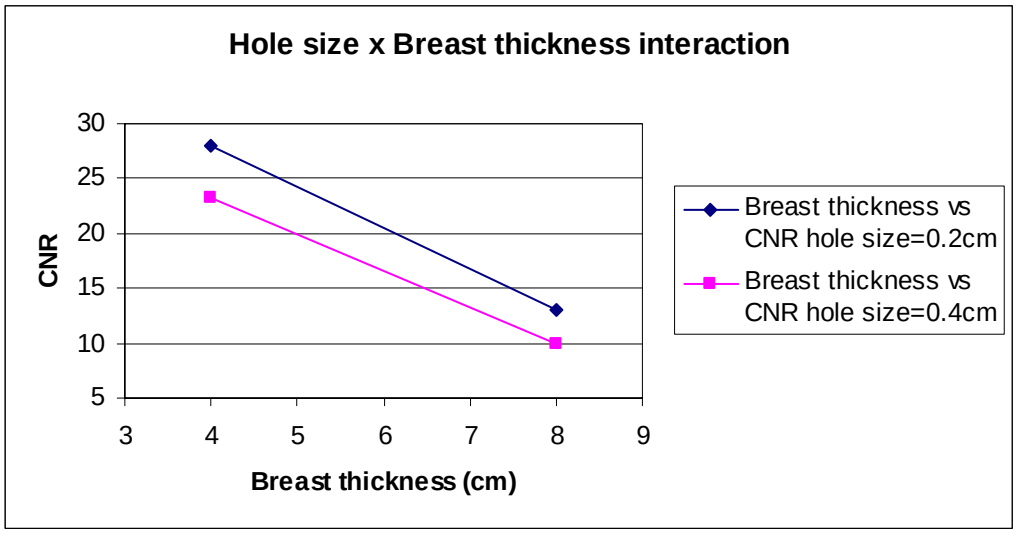

Figure 3.17 Graph showing the interaction between hole size and breast thickness.

Slope is -3.765 for hole size of 0.2cm, and -3.351 for hole size of 0.4cm. As a result, since there is a little difference between the slopes, one can say that altering hole size has a little effect on the variance produced by changing the noise variable breast thickness. Breast thickness x hole size interaction is very poor.

Septal thickness

Hole length is kept constant at 2.5cm and hole size is 0.25cm. Breast diameter and lesion size are 8cm and 0.6cm, respectively. Septal thickness is varied between 0.01cm and 0.03cm while breast thickness of 4cm and 8cm are tested.

Table 3.15
Screening experiment design for understanding the interaction between septal thickness and breast thickness.

Septal thickness (cm)	Breast diameter (cm)	CNR
0.01	4	15.7581
0.01	8	12.3955
0.03	4	13.0369
0.03	8	11.9826

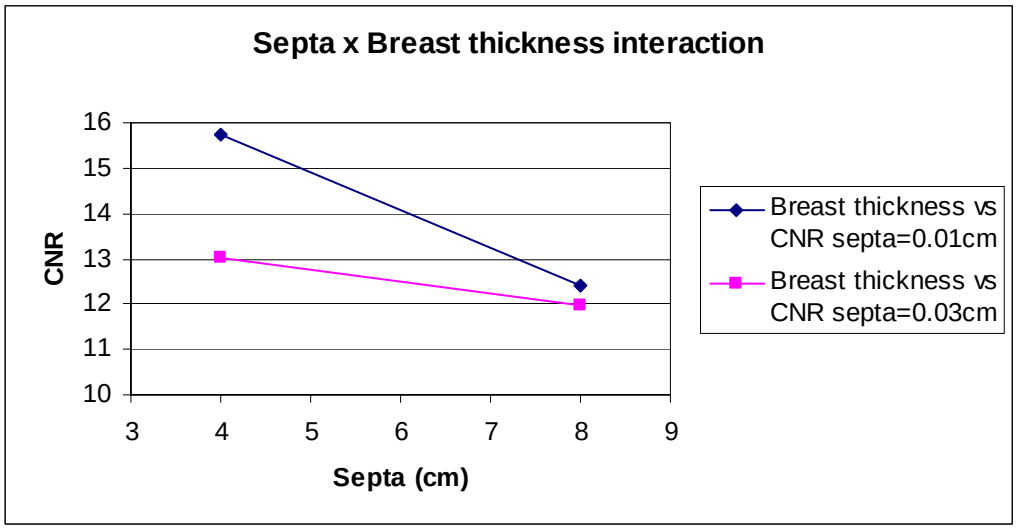

Figure 3.18 Graph showing the interaction between septal thickness and breast thickness.

Slope is -0.84 for septal thickness of 0.01cm, and -0.26 for septal thickness of 0.03cm. Since septal thickness of 0.03cm creates less variance on CNR than 0.01cm septal thickness does, one can say that breast thickness has dispersion effects and using a proper septal thickness can reduce these effects.

3.3.1.3 Collimator parameters and lesion size interactions:

Hole length

Hole size is kept constant at 0.25cm and septal thickness is 0.02cm. Breast diameter and breast thickness are 8cm and 4cm, respectively. Hole length is varied between 2.5cm and 4.5cm while lesion size of 0.6cm and 1.2cm are tested.

Table 3.16
Screening experiment design for understanding the interaction between hole length and lesion size.

Hole length (cm)	Lesion size (cm)	CNR
2.5	0.6	13.1255
2.5	1.2	61.8891
4.5	0.6	10.4521
4.5	1.2	40.2827

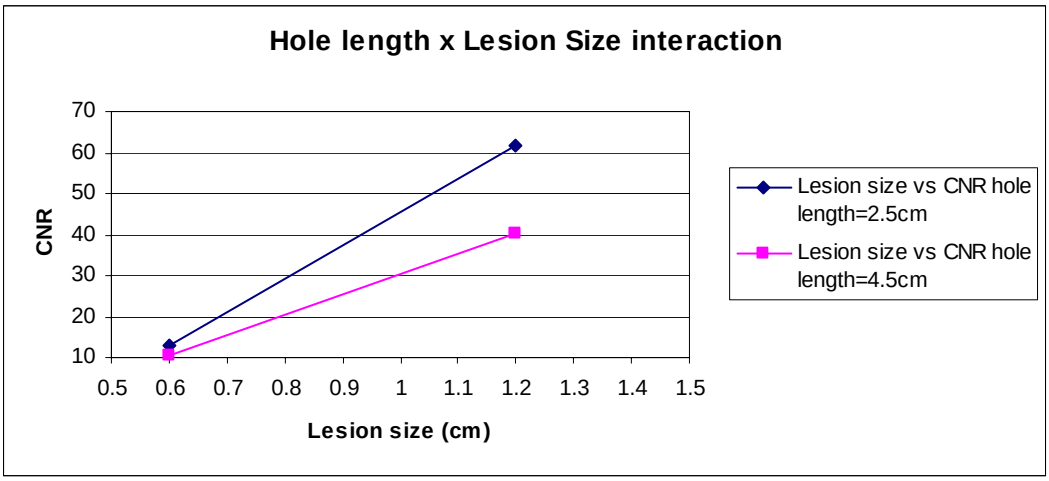

Figure 3.19 Graph showing the interaction between hole length and lesion size.

Slope is 81.27 for hole length of 2.5cm, and 49.71 for hole length of 4.5cm. Since hole length of 4.5cm creates less variance on CNR than 2.5cm hole length does, one can say that lesion size has dispersion effects and using a proper hole length can reduce these effects. In addition, lesion size has a significant location effect on CNR. By using a collimator with a hole length of 2.5cm, system response can be increased.

Hole size

Hole length is kept constant at 2.5cm and septal thickness is 0.02cm. Breast diameter and breast thickness are 8cm and 4cm, respectively. Hole size is varied between 0.2cm and 0.4cm while lesion size of 0.6cm and 1.2cm are tested.

Table 3.17
Screening experiment design for understanding the interaction between hole size and lesion size.

Hole size (cm)	Lesion Size (cm)	CNR
0.2	0.6	13.1255
0.2	1.2	61.8891
0.4	0.6	10.4129
0.4	1.2	67.1442

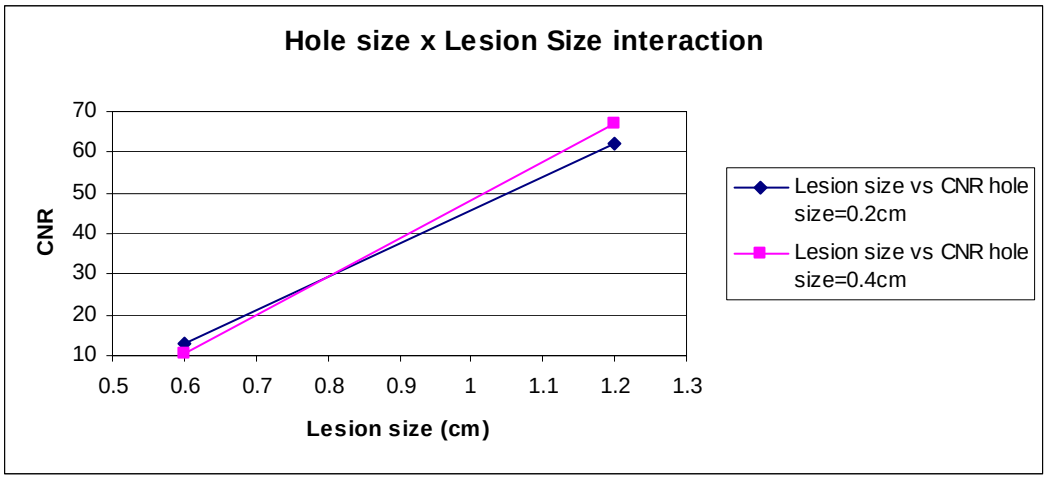

Figure 3.20 Graph showing the interaction between hole size and lesion size.

Slope is -81.27 for hole size of 0.2cm, and -94.55 for hole size of 0.4cm. Since hole size of 0.2cm creates less variance on CNR than 0.4cm hole size does, one can say that lesion size has dispersion effects and using a proper hole size can reduce these effects. Despite of this, lesion size x hole size has very little location effect on response.

Septal thickness

Hole length is kept constant at 2.5cm and hole size is 0.25cm. Breast diameter and breast thickness are 8cm and 4cm, respectively. Septal thickness is varied between 0.02cm and 0.04cm while lesion size of 0.6cm and 1.2cm are tested.

Table 3.18
Screening experiment design for understanding the interaction between septal thickness and lesion size.

Septal thickness (cm)	Lesion size (cm)	CNR
0.02	0.6	13.1255
0.02	1.2	61.8891
0.04	0.6	12.0252
0.04	1.2	56.6831

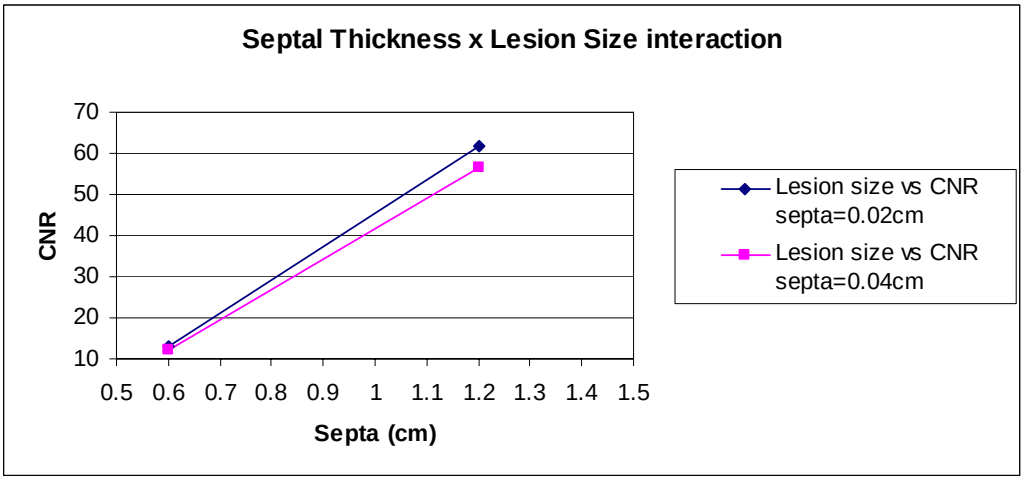

Figure 3.21 Graph showing the interaction between septal thickness and lesion size.

Slope is -81.27 for septal thickness of 0.02cm, and -74.42 for septal thickness of 0.04cm. Since septal thickness of 0.04cm creates less variance on CNR than 0.02cm septal thickness does, one can say that lesion size has dispersion effects and using a proper septal thickness can reduce these effects. In addition, since CNR values are very close at points with the same septal thickness, lesion size x septal thickness has a little location effect on CNR.

3.3.2 Design of Experiments for Robust Optimization Problem

The interactions of control parameters (collimator parameters) and noise parameters (breast and lesion parameters) are examined by screening experiments and with the sense of them, experiment set needed for understanding the collimator parameters interactions, collimator parameters x noise parameters interactions and the effects of these interactions to the response is prepared by using Box-Behnken Method. Designs include only three levels of each factor, which makes this method appealing because of the reduced number of experiments. Also, the negative experiment points coming from Central Composite Design, which are not applicable for this study, are eliminated by this method.

For Box Behnken design, the number of factors is chosen as 6 (Hole length, Septal thickness, Hole size, Breast diameter, Breast thickness and Lesion size). The low and high levels, which define the intervals for each factor are entered as in Table 3.19.

Table 3.19
Design intervals of collimator parameters for robust optimization problem.

Name	Units	-1 Level	1 Level
Hole Length	cm	1	4
Septal Thickness	cm	0.005	0.05
Hole Size	cm	0.1	0.5
Breast diameter	cm	8	12
Breast thickness	cm	5	7
Lesion size	cm	0.5	0.7

Design Expert calculates the center level for the design and creates a table of experiment inputs (Table 3.20).

Table 3.20
Design of Experiments for robust optimization problem.

	Control Parameters			Noise Parameters		
Experiment No	Hole Length	Septa	Hole Diameter	Breast Diameter	Breast Thickness	Hole Size
1	1	0.005	0.3	8	6	0.6
2	4	0.005	0.3	8	6	0.6
3	1	0.05	0.3	8	6	0.6
4	4	0.05	0.3	8	6	0.6
5	1	0.005	0.3	12	6	0.6
6	4	0.005	0.3	12	6	0.6
7	1	0.05	0.3	12	6	0.6
8	4	0.05	0.3	12	6	0.6
9	2.5	0.005	0.1	10	5	0.6
10	2.5	0.05	0.1	10	5	0.6
11	2.5	0.005	0.5	10	5	0.6
12	2.5	0.05	0.5	10	5	0.6
13	2.5	0.005	0.1	10	7	0.6
14	2.5	0.05	0.1	10	7	0.6
15	2.5	0.005	0.5	10	7	0.6
16	2.5	0.05	0.5	10	7	0.6
17	2.5	0.0275	0.1	8	6	0.5
18	2.5	0.0275	0.5	8	6	0.5
19	2.5	0.0275	0.1	12	6	0.5
20	2.5	0.0275	0.5	12	6	0.5
21	2.5	0.0275	0.1	8	6	0.7
22	2.5	0.0275	0.5	8	6	0.7

23	2.5	0.0275	0.1	12	6	0.7
24	2.5	0.0275	0.5	12	6	0.7
25	1	0.0275	0.3	8	5	0.6
26	4	0.0275	0.3	8	5	0.6
27	1	0.0275	0.3	12	5	0.6
28	4	0.0275	0.3	12	5	0.6
29	1	0.0275	0.3	8	7	0.6
30	4	0.0275	0.3	8	7	0.6
31	1	0.0275	0.3	12	7	0.6
32	4	0.0275	0.3	12	7	0.6
33	2.5	0.005	0.3	10	5	0.5
34	2.5	0.05	0.3	10	5	0.5
35	2.5	0.005	0.3	10	7	0.5
36	2.5	0.05	0.3	10	7	0.5
37	2.5	0.005	0.3	10	5	0.7
38	2.5	0.05	0.3	10	5	0.7
39	2.5	0.005	0.3	10	7	0.7
40	2.5	0.05	0.3	10	7	0.7
41	1	0.0275	0.1	10	6	0.5
42	4	0.0275	0.1	10	6	0.5
43	1	0.0275	0.5	10	6	0.5
44	4	0.0275	0.5	10	6	0.5
45	1	0.0275	0.1	10	6	0.7
46	4	0.0275	0.1	10	6	0.7
47	1	0.0275	0.5	10	6	0.7
48	4	0.0275	0.5	10	6	0.7
49	2.5	0.0275	0.3	10	6	0.6
50	2.5	0.0275	0.3	10	6	0.6
51	2.5	0.0275	0.3	10	6	0.6
52	2.5	0.0275	0.3	10	6	0.6
53	2.5	0.0275	0.3	10	6	0.6
54	2.5	0.0275	0.3	10	6	0.6

3.3.3 Simulations of Typical Optimization

Once the experiment set is built by Design Expert using Box-Behnken Design Technique, Monte Carlo Simulation software called SIMIND is employed to simulate these experiment sets. For each experiment in the design-set, there appeared two separate simulations; one for the lesion and another for the breast source. Then, the resultant simulated image pair is superimposed by MATLAB in order to produce the experiment's output. This way, for the robust optimization problem, we have conducted 108 simulations.

Simulation parameters of breast are:

Photon energy:	140 keV (99mTc)
Energy resolution:	10.6% at 140 keV
Intrinsic resolution:	0.380cm
Crystal length:	40cm
Crystal width:	50cm
Crystal thickness:	0.935cm
Source to camera distance:	4 cm (from the center of the phantom)
Energy window:	10% (126 keV−154keV)
Pixel size:	0.1cm
Image matrix size:	128x128
Collimator Hole Shape:	Hexagonal
Simulated photons:	1000000
Simulation time:	600sec

Simulation duration for one experiment was approximately 10 minutes. After each simulation, SIMIND gives a BIM output which is very simple 'image', based on keyboard character, of the matrix together with calculated data and a two row data of a profile through the matrix [141].

Table 3.21
Breast activities according to various breast dimensions.

Breast radius (cm)	Breast Thickness (cm)	Volume (cc)	Breast Activity Density (MBq/cc)	Total Activity(Bq)
4	6	301.44	3.7	1115.328
6	6	678.24	3.7	2509.488
5	5	392.5	3.7	1452.25
5	7	549.5	3.7	2033.15
4	5	251.2	3.7	929.44
6	5	565.2	3.7	2091.24
4	7	351.68	3.7	1301.216
6	7	791.28	3.7	2927.736
5	6	471	3.7	1742.7

Table 3.22
Lesion activities according to various lesion dimensions.

Lesion radius (cm)	Volume (cc)	Lesion Activity Density (MBq/cc)	Total Activity (MBq)
0.25	0.065417	20.868	1.365115
0.3	0.11304	20.868	2.3589187
0.35	0.179503	20.868	3.7458756

3.3.4 Analysis of Simulations and Getting the Responses

CNR (Contrast-to-Noise Ratio) is selected as a measure of the image quality and lesion detectability in this study. CNR is calculated by a MATLAB code from the output files of lesion and breast simulation. This code takes the *.bim files as inputs and gives the CNR value and the resultant image file (as a Matlab figure file *.fig).

The CNR values achieved by the application of the Matlab code are in Table 3.23. In Table 3.24, design summary can be seen.

Table 3.23
Experiment results of robust optimization problem.

	Control Parameters			Noise Parameters			
Experiment No	**Hole Length**	**Septa**	**Hole Diameter**	**Breast Diameter**	**Breast Thickness**	**Hole Size**	**CNR**
1	1	0.005	0.3	8	6	0.6	8.071
2	4	0.005	0.3	8	6	0.6	12.8941
3	1	0.05	0.3	8	6	0.6	9.5536
4	4	0.05	0.3	8	6	0.6	12.2293
5	1	0.005	0.3	12	6	0.6	7.5762
6	4	0.005	0.3	12	6	0.6	12.6652
7	1	0.05	0.3	12	6	0.6	9.1076
8	4	0.05	0.3	12	6	0.6	12.0088
9	2.5	0.005	0.1	10	5	0.6	15.6751
10	2.5	0.05	0.1	10	5	0.6	10.9057
11	2.5	0.005	0.5	10	5	0.6	10.1587
12	2.5	0.05	0.5	10	5	0.6	12.5381
13	2.5	0.005	0.1	10	7	0.6	11.4494
14	2.5	0.05	0.1	10	7	0.6	8.0006
15	2.5	0.005	0.5	10	7	0.6	6.6607
16	2.5	0.05	0.5	10	7	0.6	8.2014
17	2.5	0.0275	0.1	8	6	0.5	7.8625
18	2.5	0.0275	0.5	8	6	0.5	6.3166
19	2.5	0.0275	0.1	12	6	0.5	7.7569
20	2.5	0.0275	0.5	12	6	0.5	6.0876
21	2.5	0.0275	0.1	8	6	0.7	16.2996
22	2.5	0.0275	0.5	8	6	0.7	16.5209
23	2.5	0.0275	0.1	12	6	0.7	16.0835
24	2.5	0.0275	0.5	12	6	0.7	15.998
25	1	0.0275	0.3	8	5	0.6	12.5688
26	4	0.0275	0.3	8	5	0.6	15.7888
27	1	0.0275	0.3	12	5	0.6	12.0527
28	4	0.0275	0.3	12	5	0.6	15.5408
29	1	0.0275	0.3	8	7	0.6	7.9957
30	4	0.0275	0.3	8	7	0.6	10.9275
31	1	0.0275	0.3	12	7	0.6	7.5755
32	4	0.0275	0.3	12	7	0.6	10.72
33	2.5	0.005	0.3	10	5	0.5	9.0196
34	2.5	0.05	0.3	10	5	0.5	9.5554
35	2.5	0.005	0.3	10	7	0.5	5.9391
36	2.5	0.05	0.3	10	7	0.5	6.2725
37	2.5	0.005	0.3	10	5	0.7	23.1128
38	2.5	0.05	0.3	10	5	0.7	24.0941
39	2.5	0.005	0.3	10	7	0.7	15.2722
40	2.5	0.05	0.3	10	7	0.7	15.9823
41	1	0.0275	0.1	10	6	0.5	9.3653
42	4	0.0275	0.1	10	6	0.5	5.5801
43	1	0.0275	0.5	10	6	0.5	4.0946

44	4	0.0275	0.5	10	6	0.5	6.7099
45	1	0.0275	0.1	10	6	0.7	22.8467
46	4	0.0275	0.1	10	6	0.7	11.1289
47	1	0.0275	0.5	10	6	0.7	11.0249
48	4	0.0275	0.5	10	6	0.7	17.2828
49	2.5	0.0275	0.3	10	6	0.6	13.3336
50	2.5	0.0275	0.3	10	6	0.6	13.3065
51	2.5	0.0275	0.3	10	6	0.6	13.347
52	2.5	0.0275	0.3	10	6	0.6	13.3175
53	2.5	0.0275	0.3	10	6	0.6	13.2871
54	2.5	0.0275	0.3	10	6	0.6	13.3

Design Summary is as follows:

Table 3.24
Design Summary of robust optimization problem.

					Study Type	Response Surface	
					Initial Design	Box-Behnken	
					Design Model	Quadratic	
					Runs	17	
					Blocks	No Blocks	
Factor	**Name**	**Low Actual**	**High Actual**	**Low Coded**	**High Coded**	**Mean**	**Std. Dev.**
A	Hole Length	1	4	-1	1	2.5	1
B	Septal Thickness	0.005	0.05	-1	1	0	0
C	Hole Size	0.1	0.5	-1	1	0.3	0.1
D	Breast Diameter	8	12	-1	1	10	1.3
E	Breast Thickness	5	7	-1	1	6	0.7
F	Lesion Diameter	0.5	0.7	-1	1	0.6	0.1
Response	**Name**	**Analysis**	**Min**	**Max**	**Mean**	**Std. Dev.**	**Ratio**
Y1	SNR	Polynomial	4.09	24.1	12	4.4	5.9

3.3.5 Response Surface Method Analysis of Robust Optimization Problem

Analysis of the experimental data and robust optimization process is carried out by Design Expert software. Clicking on the Fit Summary button starts the regression calculations to fit all of the polynomial models to the selected response.

The program calculates the effects for all model terms. It produces statistics such as p-values, lack of fit and R-squared values for comparing the models (Table 3.25). If a statistically significant model is detected, the program will underline and note the "Suggested" model. This becomes the default model on the Model screen.

Table 3.25
Regression tests for assigning the most proper model. Quadraric model is suggested.

Response:	CNR		**Transform:**	None		
Sequential Model Sum of Squares [Type I]						
Source	**Sum of Squares**	**df**	**Mean Square**	**F Value**	**p-value Prob>F**	
Mean vs Total	7372.506	1	7372.506			
Linear vs Mean	780.7944	6	130.1324	23.64228	< 0.0001	
2FI vs Linear	109.3452	15	7.289681	1.561866	0.1415	
Quadratic vs 2FI	73.99627	6	12.33271	4.255084	0.0041	Suggested
Cubic vs Quadratic	73.81032	18	4.100573	21.20941	< 0.0001	Aliased
Residual	1.5467	8	0.193337			
Total	8411.999	54	155.7778			
Lack of Fit Tests						
Source	**Sum of Squares**	**df**	**Mean Square**	**F Value**	**p-value Prob>F**	
Linear	258.696	42	6.15943	12563.15	< 0.0001	
2FI	149.3508	27	5.531512	11282.41	< 0.0001	
Quadratic	75.35457	21	3.588313	7318.94	< 0.0001	Suggested
Cubic	1.544249	3	0.51475	1049.914	< 0.0001	Aliased
Pure Error	0.002451	5	0.00049			
Model Summary Statistics						
Source	**Std. Dev.**	**R-Squared**	**Adjusted R-Squared**	**Predicted R-Squared**	**PRESS**	
Linear	2.346108	0.75113	0.719359	0.665729	347.4728	
2FI	2.160391	0.856321	0.762032	0.550404	467.3517	
Quadratic	1.702453	0.927506	0.852224	0.621265	393.6927	Suggested
Cubic	0.439702	0.998512	0.990142	0.619688	395.3312	Aliased

In Table 3.25, we have looked for:

i) The highest order model that is significant (P-value small) and not aliased.

ii) No lack of fit (P-value > 0.10)

iii) Reasonable agreement between Adjusted R-squared and Predicted R-squared (within 0.2 of each other).

From the analysis of regression models, it is proper to fit a second order (quadratic) model for our data. In order to improve the model, insignificant terms (values of “Prob>F” greater than 0.1) are eliminated. ANOVA report and the regression model is as follows:

Table 3.26
ANOVA (Analysis of variance) table for the quadratic model of robust optimization problem.

ANOVA for Response Surface Quadratic Model						
Analysis of variance table [Partial sum of squares - Type III]						
Source	**Sum of Squares**	**df**	**Mean Square**	**F Value**	**p-value Prob > F**	
Model	920.1116	12	76.67597	26.3334	< 0.0001	
A-Hole Length	19.51856	1	19.51856	6.703403	0.0133	
B-Septal Thickness	8.33E-05	1	8.33E-05	2.86E-05	0.9958	
C-Hole Size	19.01058	1	19.01058	6.528943	0.0144	
D-Breast Diameter	0.619402	1	0.619402	0.212726	0.6471	
E-Breast Thickness	130.7306	1	130.7306	44.89778	< 0.0001	
F-Lesion Diameter	610.9152	1	610.9152	209.8111	< 0.0001	
AB	2.349245	1	2.349245	0.806819	0.3743	
AC	74.27489	1	74.27489	25.50878	< 0.0001	
CF	0.207936	1	0.207936	0.071413	0.7906	
A^2	20.34121	1	20.34121	6.985931	0.0116	
C^2	41.77571	1	41.77571	14.34734	0.0005	
F^2	17.42191	1	17.42191	5.983335	0.0188	
Residual	119.3813	41	2.911739			
Lack of Fit	119.3788	36	3.316079	6763.675	< 0.0001	
Pure Error	0.002451	5	0.00049			
Cor Total	1039.493	53				
Std. Dev.	1.722492		**R-Squared**	0.891538		
Mean	11.68451		**Adj R-Squared**	0.848724		
C.V. %	14.74167		**Pred R-Squared**	0.737893		
PRESS	272.4588		**Adeq Precision**	21.64063		
Factor	**Coefficient Estimate**	**df**	**Standard Error**	**95% CI Low**	**95% CI High**	**VIF**
Intercept	13.10152	1	0.574164	11.93918	14.26385	
A-Hole Length	0.901817	1	0.351602	0.190035	1.613598	1
B-Septal Thickness	-0.00186	1	0.351602	-0.71364	0.709919	1
C-Hole Size	-0.89	1	0.351602	-1.60179	-0.17822	1
D-Breast Diameter	-0.16065	1	0.351602	-0.87243	0.551132	1
E-Breast Thickness	-2.3339	1	0.351602	-3.04569	-1.62212	1
F-Lesion Diameter	5.045275	1	0.351602	4.333493	5.757057	1
AB	-0.5419	1	0.608993	-1.77474	0.690942	1
AC	3.047025	1	0.608993	1.814183	4.279867	1
BF	0.102775	1	0.608993	-1.13007	1.335617	1
CF	0.114	1	0.430623	-0.75775	0.985751	1
DF	-0.05055	1	0.608993	-1.28339	1.182292	1
A^2	-1.47635	1	0.50495	-2.49857	-0.45413	1.145833
B^2	-0.74918	1	0.50495	-1.7714	0.27304	1.145833

C^2	-2.08501	1	0.527403	-3.15268	-1.01733	1.25
F^2	1.122281	1	0.527403	0.054608	2.189953	1.25

Final Equation in Terms of Coded Factors:	
CNR	=
13.10152	
0.901817	* A
-0.00186	* B
-0.89	* C
-0.16065	* D
-2.3339	* E
5.045275	* F
-0.5419	* A * B
3.047025	* A * C
0.102775	* B * F
0.114	* C * F
-0.05055	* D * F
-1.47635	* A^2
-0.74918	* B^2
-2.08501	* C^2
1.122281	* F^2

Final Equation in Terms of Actual Factors:	
CNR	=
34.7384	
1.276507	* Hole Length
94.04357	* Septal Thickness
-1.98679	* Hole Size
0.071325	* Breast Diameter
-2.3339	* Breast Thickness
-84.6596	* Lesion Diameter
-16.0563	* Hole Length * Septal Thickness
10.15675	* Hole Length * Hole Size
45.67778	* Septal Thickness * Lesion Diameter
5.7	* Hole Size * Lesion Diameter
-0.25275	* Breast Diameter * Lesion Diameter
-0.65615	* Hole Length^2
-1479.86	* Septal Thickness^2
-52.1252	* Hole Size^2
112.2281	* Lesion Diameter^2

The “Prob>F value” of the model is very small (less than 0.05) then the terms in the model have a significant effect on the response. From the Table 3.26 one can derive that this model is sufficient to represent the relationship between collimator variables and CNR.

Also, if the “Prob>F value” is very small (less than 0.05) then the individual terms in the model have a significant effect on the response. The “Prob>F value” greater than 0.1 indicates the corresponding model term is insignificant. In order to improve our model, the terms A*D, A*E, A*F, BC*, B*D, B*E, C*D, C*E, D*E, E*F, D^2, A^2 are eliminated. A, C, E, F, A*C, A^2, C^2 and F^2 are the most significant terms with “Prob>F values” less than 0.05.

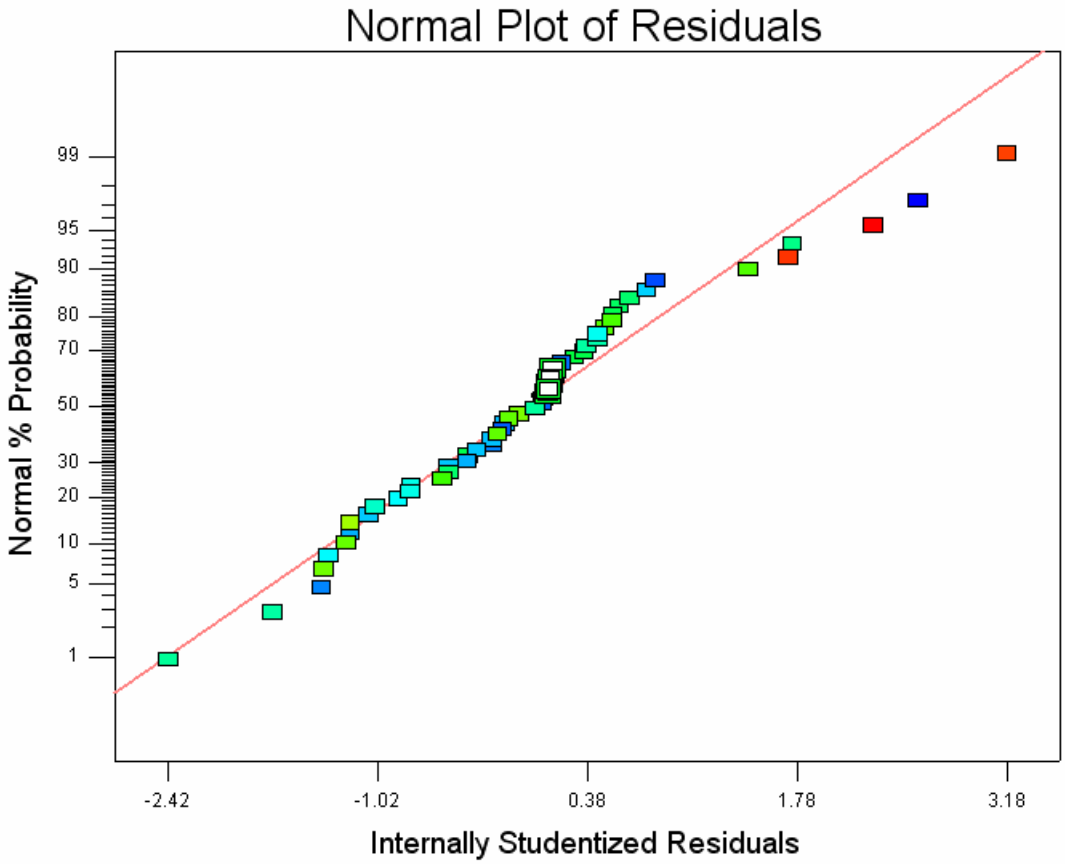

Figure 3.22 Normal plot of residuals (robust optimization problem).

The normal probability plot indicates whether the residuals follow a normal distribution, in which case the points will follow a straight line. Some moderate scatter is expected even with normal data. In (Figure 3.22), a scatter is observed through the straight line.

4. RESULTS

4.1 Typical Optimization Problem

4.1.1 The Model

The method of least squares is employed by Design Expert to derive the model of the relation between collimator parameters and CNR. The model in terms of coded factors and in terms of actual factors is below.

Final Equation in Terms of Coded Factors:

CNR	=
14.43092	
0.469463	* A
-0.0877	* B
-0.62384	* C
-0.74093	* A * B
3.35405	* A * C
1.576775	* B * C
-1.57961	* A^2
-1.61014	* B^2
-2.31966	* C^2

Final Equation in Terms of Actual Factors:

CNR	=
12.44571	
1.072886	* Hole Length
120.7955	* Septal Thickness
-5.91055	* Hole Size
-21.9533	* Hole Length * Septal Thickness
11.18017	* Hole Length * Hole Size
350.3944	* Septal Thickness * Hole Size
-0.70205	* Hole Length^2
-3180.51	* $\text{Septal Thickness}^2$
-57.9915	* Hole Size^2

Contour plots, Figure 4.1(a), 4.2(a), and 4.3 (a) show contours of constant response with the axis systems of hole length vs septal thickness, hole length vs hole size, septal thickness vs hole size, respectively, while the other design variables are held constant. Response surface plots of the same graphs are shown in Figure 4.1 (b), 4.2 (b) and 4.3 (b).

a)

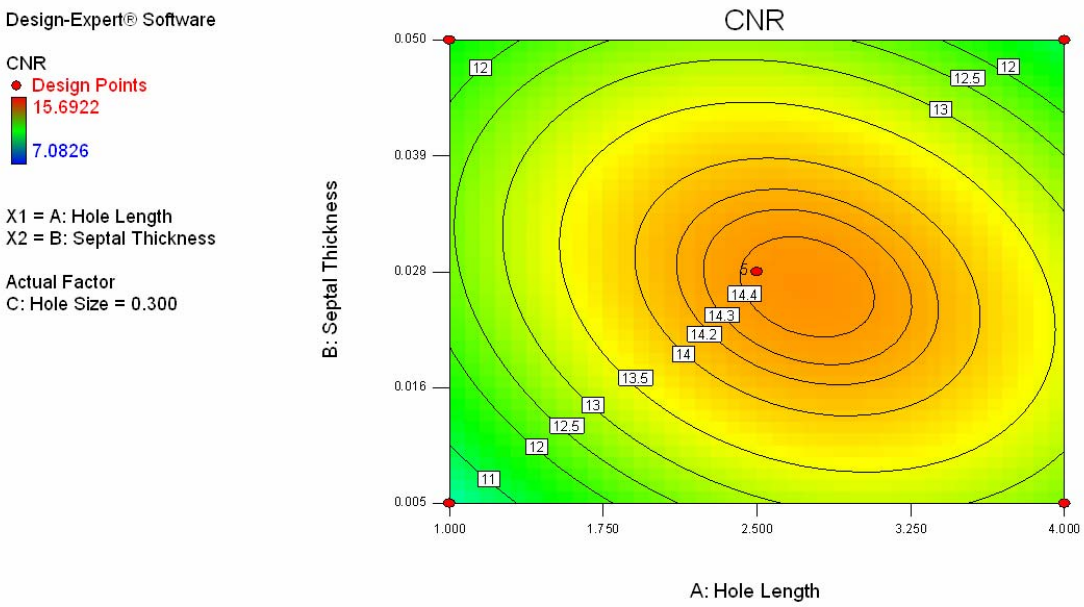

b)

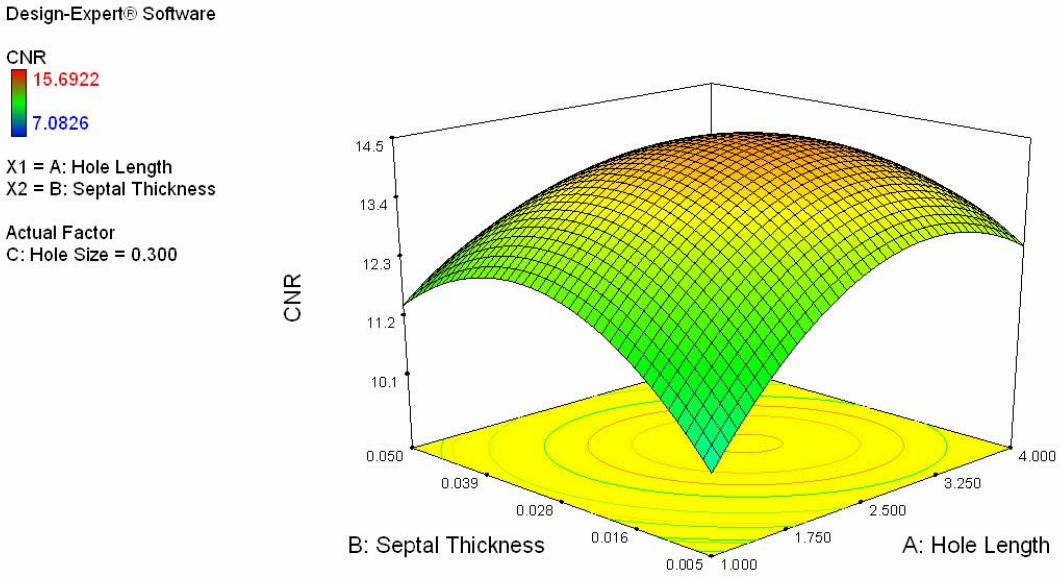

Figure 4.1 a) Contour plot of CNR with respect to hole length and septal thickness while hole size is kept at 0.3cm. b) Response surface plot of CNR with respect to hole length and septal thickness while hole size is kept 0.3cm.

a)

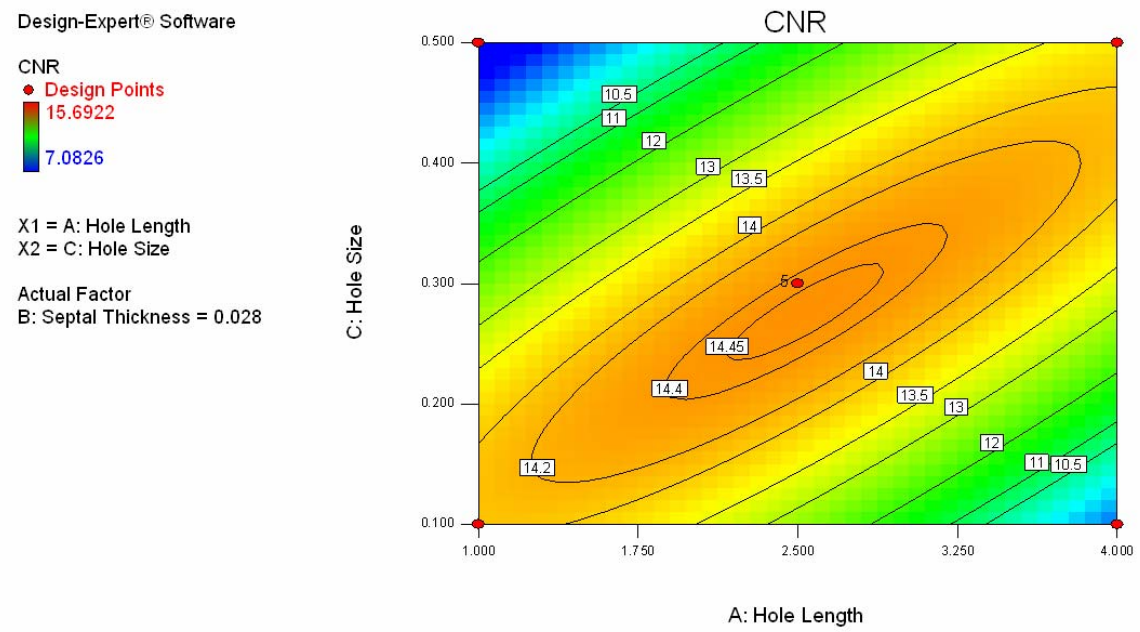

b)

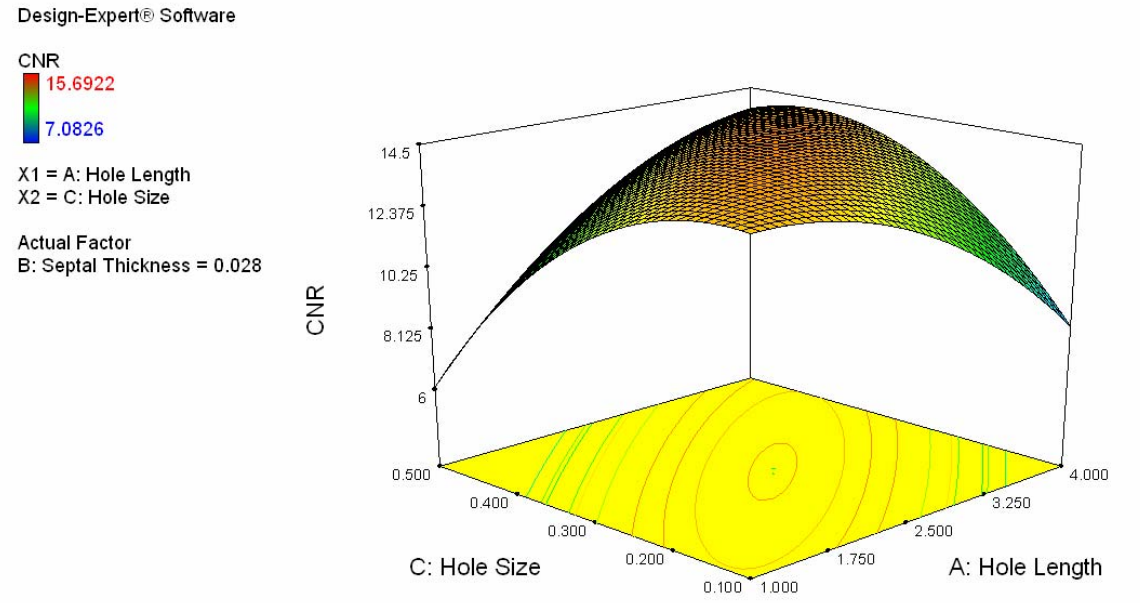

Figure 4.2 a) Contour plot of CNR with respect to hole length and hole size while septal thickness is kept at 0.028cm. b) Response surface plot of CNR with respect to hole length and hole size while septal thickness is kept 0.028cm.

a)

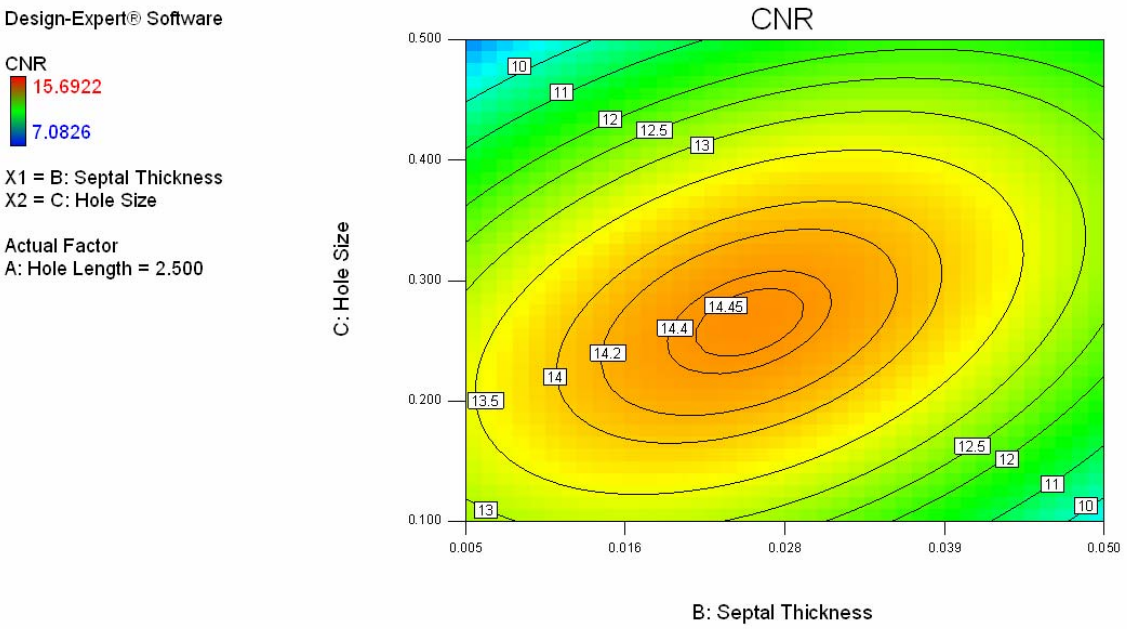

b)

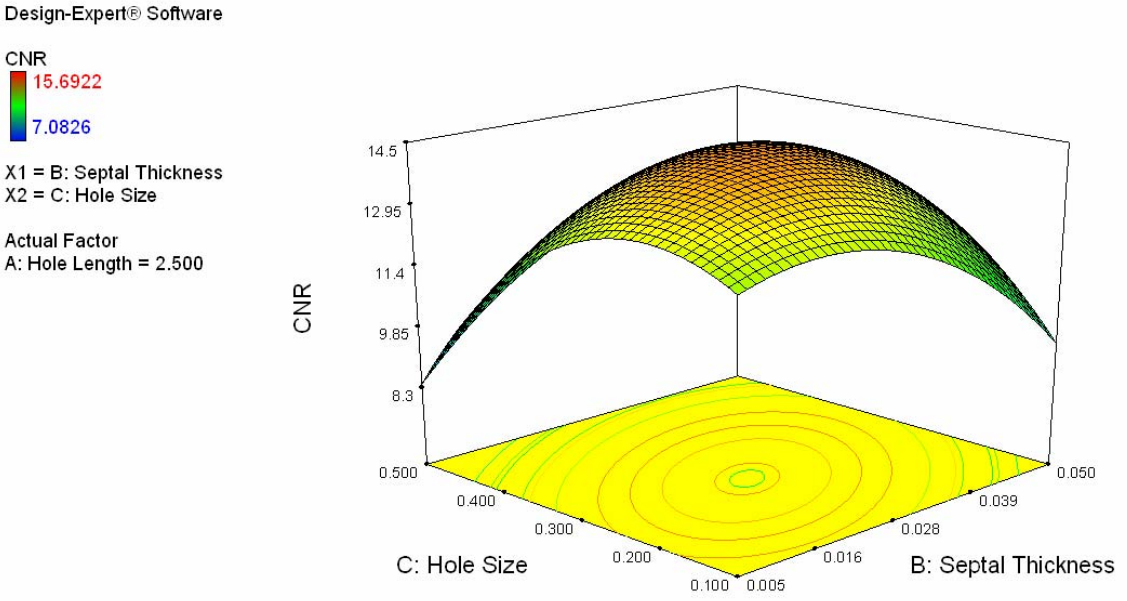

Figure 4.3 a) Contour plot of CNR with respect to septal thickness and hole size while hole length is kept at 2.5cm. b) Response surface plot of CNR with respect to septal thickness and hole size while hole length is kept 2.5cm.

4.1.2 Response Surface Optimization of Typical Optimization Problem

Numerical optimization searches the design space, using the model created in the analysis, to find factor settings that meet the maximum CNR goal. The goal of maximization for the response CNR is defined in "Criteria" screen (Figure 4.4) in Design Expert. Limits are set as the minimum and maximum responses achieved by the model. Importance determines the relative importance of one response versus another. Since there is only one response in the typical optimization problem, this importance selection is trivial.

Weight can range from 0.1 to 1 and it fine-tunes how the optimization process searches for the best solution. A low weight (near 0.1) will allow more solutions that don't quite meet the optimal goal. A high weight (close to 1) will cause the optimization to seek a solution close to or beyond the stated goal. From a practical standpoint, the weights are left at 1. Finally Design Expert generates a list of potential factor settings that provide response that meets the defined criteria.

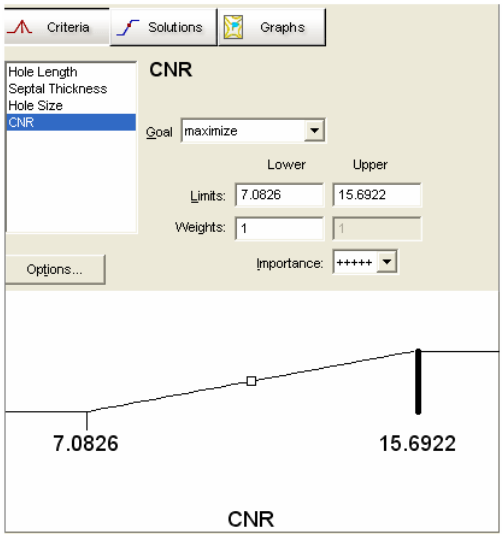

Figure 4.4 Criteria definition for typical optimization problem. Optimization goal, limits of the response, weights and importance can be adjusted for desirable optimization process.

Table 4.1
Numerical optimization solution for typical optimization problem.

Constraints						
Name	**Goal**	**Lower Limit**	**Upper Limit**	**Lower Weight**	**Upper Weight**	**Importance**
Hole Length	is in range	1	4	1	1	3
Septa	is in range	0.005	0.05	1	1	3
Hole Size	is in range	0.1	0.5	1	1	3
CNR	maximize	7.0826	15.6922	1	1	5
Solutions						
Number	**Hole Length**	**Septa**	**Hole Size**	**CNR**	**Desirability**	
1	2.444197	0.024861	0.259686	14.4901	0.860377	Selected

In Table 4.1, constraints part summarizes the set for the optimization run. In solutions list, the optimum solution that meets the optimization criteria is displayed. A hole length of 2.444cm, a septal thickness of 0.024cm and a hole size of 0.259cm is the optimum solution for the first part of the study with a desirability of 0.860. This point defines the parameters of optimum collimator. In Figure 4.5, this point of optimum is showed in ramp graphs of hole length, septal thickness and hole size with red dots. The response, CNR, at this optimum point is marked with a blue dot on the ramp graph of CNR.

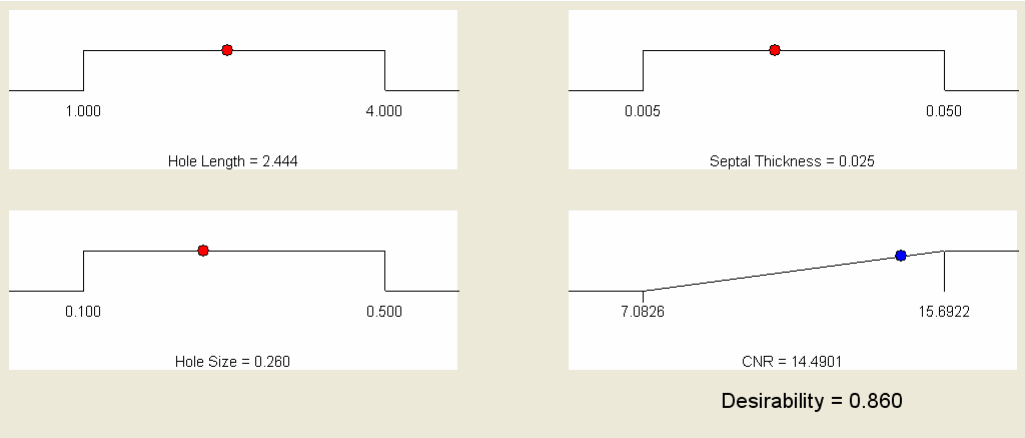

Figure 4.5 Ramp graphs of the solution of typical optimization problem. The optimum point is marked with red dots on collimator parameter graphs. The last graph shows the optimum CNR value on the response ramp graph.

In Figure 4.6, the corresponding CNR value of optimal collimator parameters is pointed out with a flag on the contour plot of CNR with respect to hole length and septal thickness (hole size is kept constant at its optimum value of 0.260cm). In an analogous way, Figure 4.7 shows the corresponding CNR value of optimal collimator parameters on the contour plot of CNR with respect to hole length and hole size. Finally, Figure 4.8 shows the same point in a contour plot of CNR with respect to septal thickness and hole size.

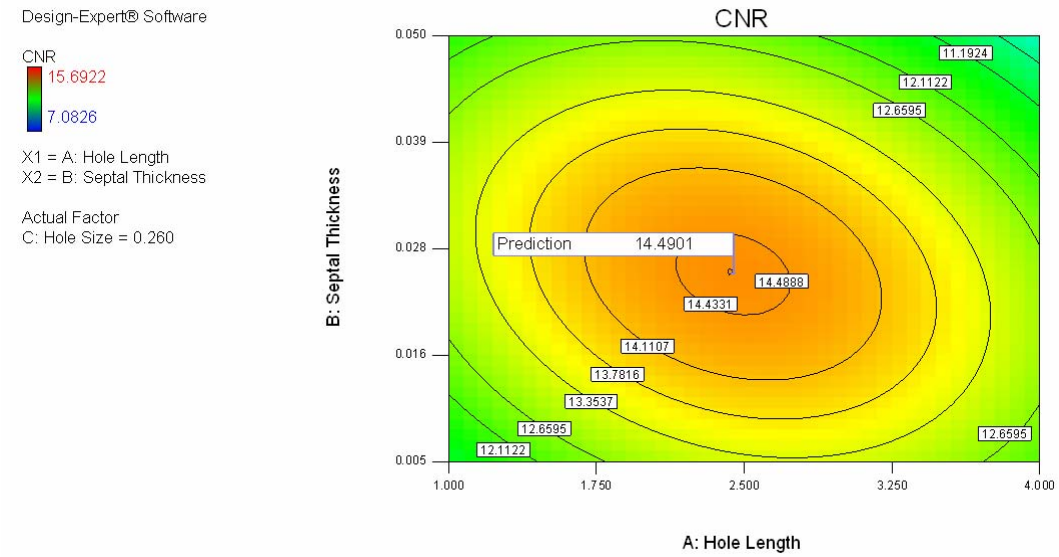

Figure 4.6 Contour plot of optimum CNR with respect to hole length and septal thickness while hole size is kept constant at 0.26cm. The optimum predicted CNR value (14.4901) is marked with a flag.

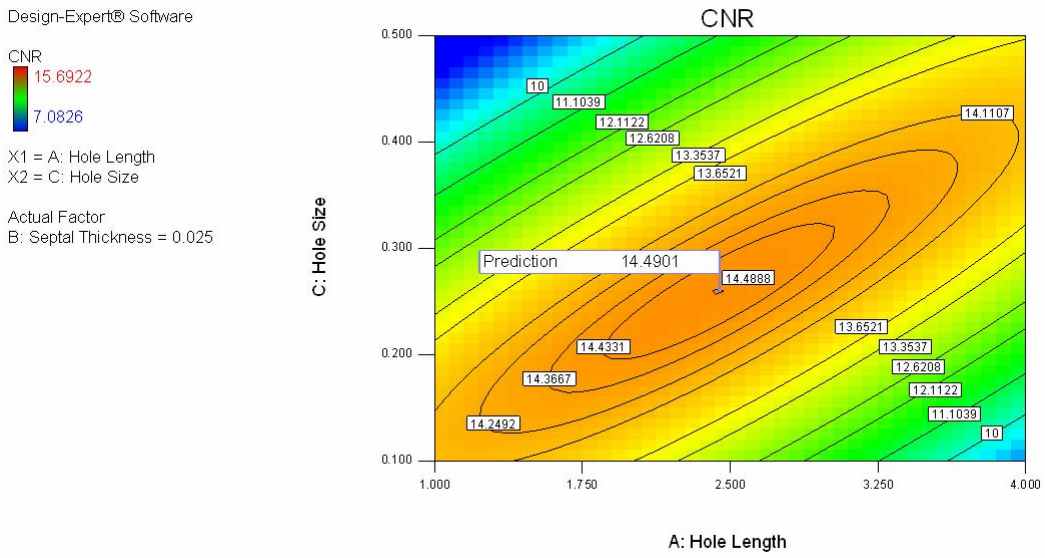

Figure 4.7 Contour plot of optimum CNR with respect to hole length and hole size while septal thickness is kept constant at 0.025cm. The optimum predicted CNR value (14.4901) is marked with a flag.

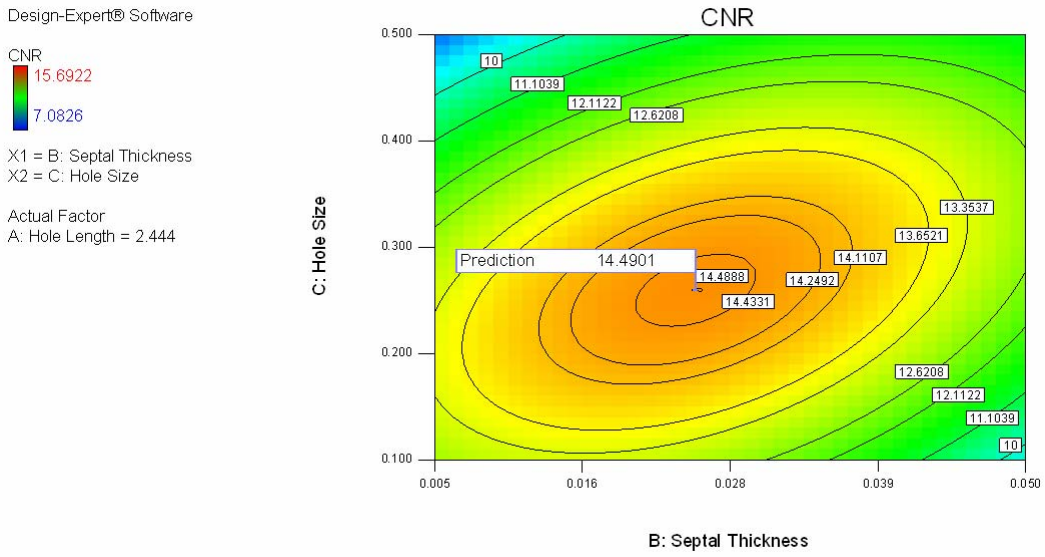

Figure 4.8 Contour plot of optimum CNR with respect to septal thickness and hole size while hole length is kept constant at 2.444cm. The optimum predicted CNR value (14.4901) is marked with a flag.

4.1.3 Comparison of Results with Commercial collimators

The result of optimization operation (called optimum collimator) is simulated in SIMIND and its performance is compared with the commercial collimator parameters in light of performance measures CNR and relative improvement (Table 4.2).

Relative improvement of the selected commercial collimator is the measure of the performance difference compared to the optimum collimator. This ratio indicates how much the selected commercial collimator's performance can be improved relative to the optimum collimator's performance.

Table 4.2
Comparison of optimum collimator with commercial collimators.

Collimator	Hole Size (cm)	Septa (cm)	Hole Length (cm)	CNR	Relative Improvement
A	0.250	0.030	4.100	12.717	13.18%
B	0.140	0.018	2.920	13.121	9.69%
C	0.140	0.020	2.540	13.915	3.43%
D	0.170	0.020	3.500	12.792	12.51%
E	0.130	0.020	3.500	11.036	30.41%
F	0.111	0.016	2.360	13.288	8.31%
G	0.145	0.020	2.410	14.110	2.00%
OPTIMUM	0.259	0.024	2.444	14.393	

In Figure 4.9, the performance values are graphed in a column graph showing the performance of the optimum collimator is the largest over the commercial collimators.

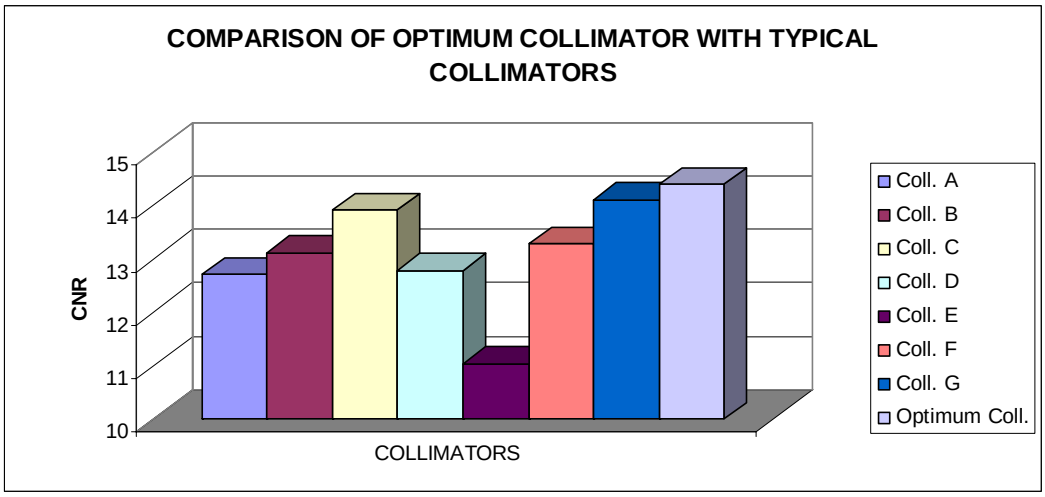

Figure 4.9 Column graph showing comparison of optimum collimator's performance with commercial collimators' performances.

In order to see if the numerical results in Table 4.2 and Figure 4.9 coincide with simulation results, SIMIND is utilized. The images in Figure 4.10 are achieved by the simulations of our phantom model in SIMIND by using commercial collimators A, B, C, D, E, F, G and optimum collimator derived in this study. Last image, which is the resultant image of optimum collimator simulation, gives the best lesion detectability. Consequently, compatibilities of the model and simulation results are verified.

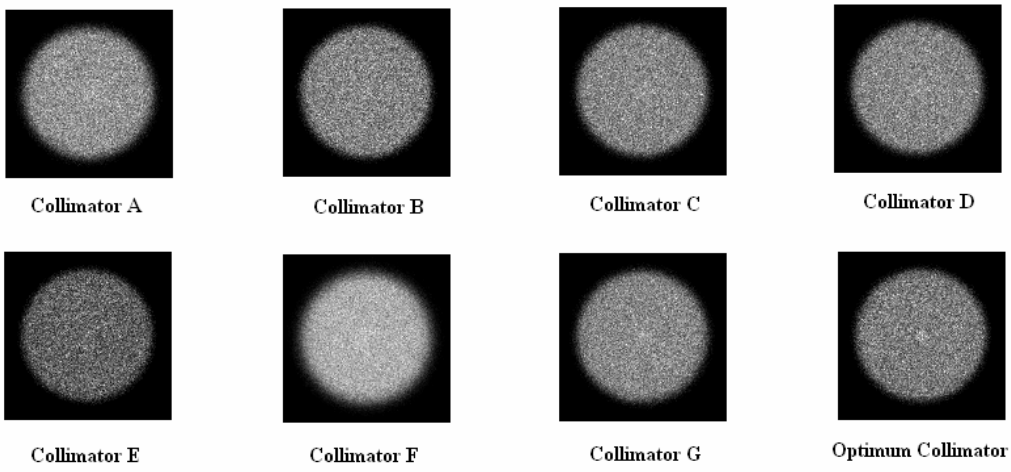

Figure 4.10 Comparison of simulated image of optimum collimator with commercial collimators' (A, B, C, D, E, F and G) simulated images.

4.2 Robust Optimization Problem

4.2.1 The Model

The method of least squares is employed by Design Expert to derive the model of the relation between controllable collimator parameters, uncontrollable breast, lesion parameters and CNR. The model in terms of coded factors and in terms of actual factors is below:

Final Equation in Terms of Coded Factors:

$$
\begin{aligned}
CNR = {} & 13.10152 \\
& + 0.901817 * A \\
& - 0.00186 * B \\
& - 0.89 * C \\
& - 0.16065 * D \\
& - 2.3339 * E \\
& + 5.045275 * F \\
& - 0.5419 * A * B \\
& + 3.047025 * A * C \\
& + 0.102775 * B * F \\
& + 0.114 * C * F \\
& - 0.05055 * D * F \\
& - 1.47635 * A^2 \\
& - 0.74918 * B^2 \\
& - 2.08501 * C^2 \\
& + 1.122281 * F2
\end{aligned}
$$

Final Equation in Terms of Actual Factors:

CNR	=
34.7384	
1.276507	* Hole Length
94.04357	* Septal Thickness
-1.98679	* Hole Size
0.071325	* Breast Diameter
-2.3339	* Breast Thickness
-84.6596	* Lesion Diameter
-16.0563	* Hole Length * Septal Thickness
10.15675	* Hole Length * Hole Size
45.67778	* Septal Thickness * Lesion Diameter
5.7	* Hole Size * Lesion Diameter
-0.25275	* Breast Diameter * Lesion Diameter
-0.65615	* Hole Length^2
-1479.86	* Septal Thickness^2
-52.1252	* Hole Size^2
112.2281	* Lesion Diameter^2

Contour plots, Figure 4.11 (a) and 4.12 (a) show contours of constant response with the axis systems of hole length vs septal thickness, hole length vs hole size, respectively, while the other design and noise variables are held constant (Hole size is 0.30cm, breast diameter is 10cm, breast thickness is 6cm and lesion diameter is 0.6cm). Response surface plots of the same graphs are shown in Figure 4.11 (b) and 4.12 (b).

a)

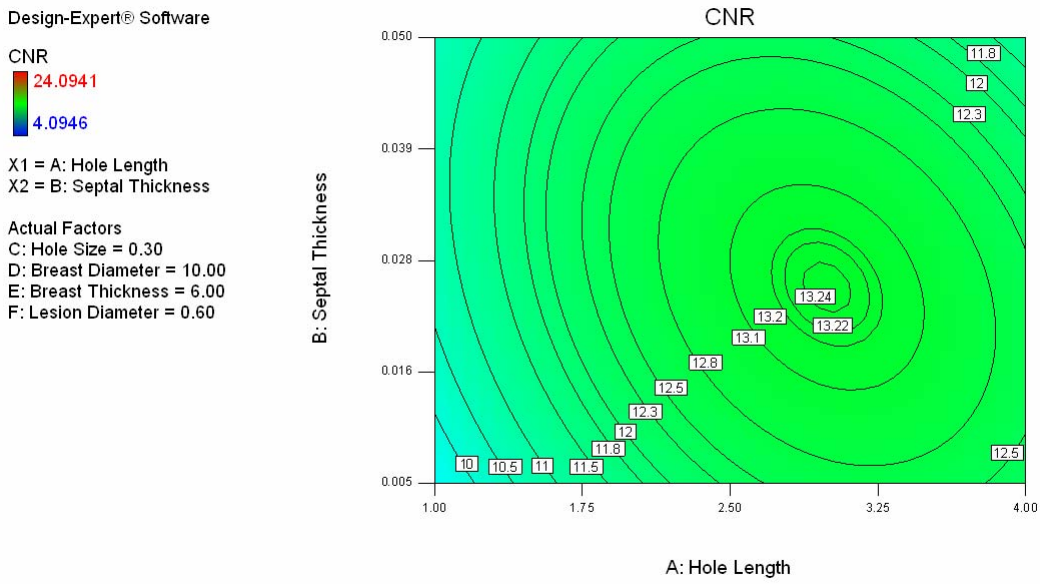

b)

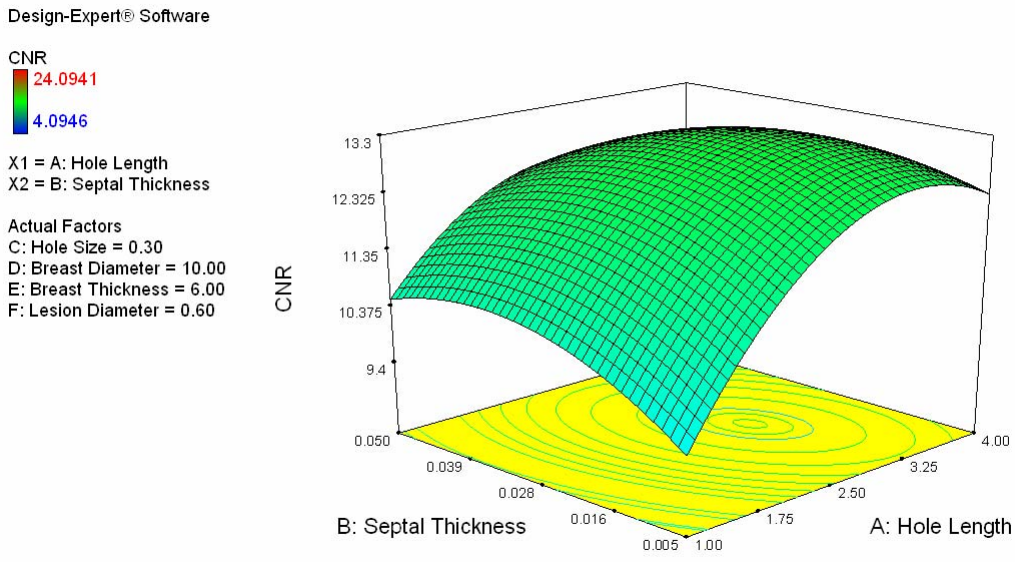

Figure 4.11 a) Contour plot of CNR with respect to hole length and septal thickness while hole size is kept at 0.3cm. The noise variables are kept constant (breast thickness is10cm, breast thickness is 6cm, lesion diameter is 0.6cm). b) Response surface plot of CNR with respect to hole length and septal thickness while hole size is kept 0.3cm. The noise variables; breast diameter is 10cm, breast thickness is 6cm, lesion diameter is 0.6cm.

a)

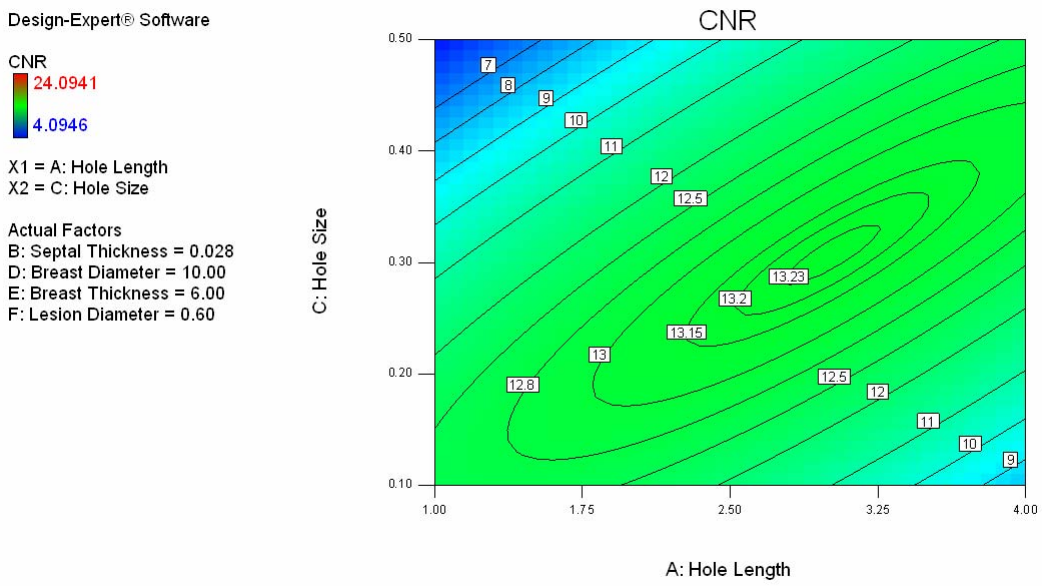

b)

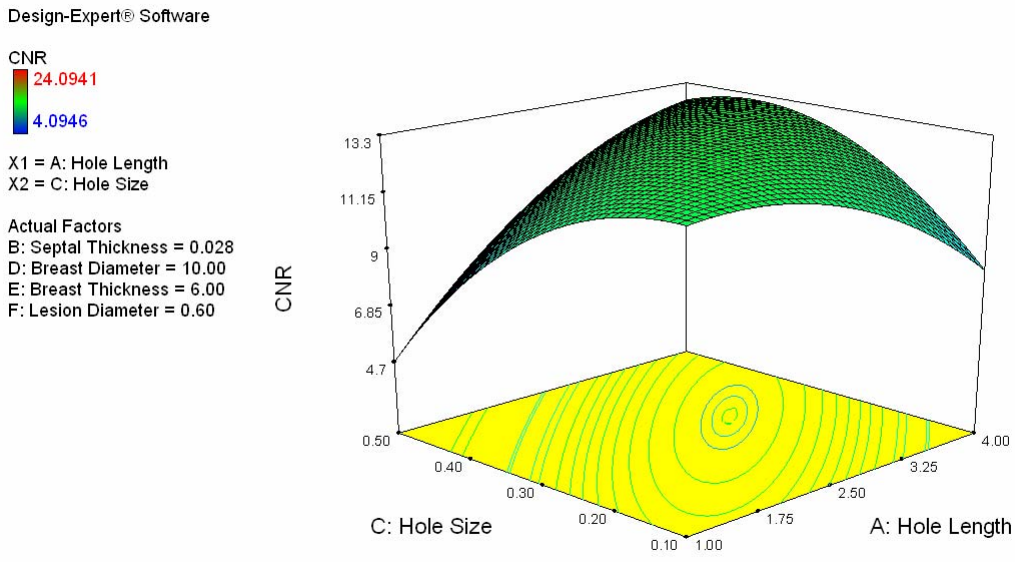

Figure 4.12 a) Contour plot of CNR with respect to hole length and hole size while septal thickness is kept at 0.028cm. The noise variables are kept constant (breast thickness is10cm, breast thickness is 6cm, lesion diameter is 0.6cm). b) Response surface plot of CNR with respect to hole length and hole size while septal thickness is kept 0.028cm. The noise variables; breast diameter is 10cm, breast thickness is 6cm, lesion diameter is 0.6cm.

4.2.2 Response Surface Optimization of Robust Optimization Problem

Numerical optimization searches the design space, using the model created in the CNR analysis, to find factor settings that meet the sufficiently large CNR that will satisfy lesion detectability and a minimum Propagation of Error (POE) of CNR, which is a measure that makes the CNR be affected minimally from patient variations. First, the quadratic model that shows the relation between response and both controllable collimator parameters and uncontrollable patient parameters is constructed. Then, the goals of maximization of the response CNR and minimization of POE(CNR) are defined (Figure 4.13 (a) and (b)).

Robust optimization is the process of making compromises between mean and the variance of CNR. It can be assumed that in the robust optimization problem of this study, there are two responses, CNR and POE(CNR) and the aim is to make compromise between them to find the collimator parameter set that makes the system less susceptible to patient varieties. Importance determines the relative importance of one response versus another. Since getting a CNR large enough for lesion detectability is more important than getting a small POE where CNR is insufficient for lesion detectability, the importance is "+++++" for CNR and "+" for POE(CNR).

Weight can range from 0.1 to 1 and it fine-tunes how the optimization process searches for the best solution. A low weight (near 0.1) will allow more solutions that don't quite meet the optimal goal. A high weight (close to 1) will cause the optimization to seek a solution close to or beyond the stated goal. From a practical standpoint, the weights are left at 1.

Finally Design Expert generates a list of potential factor settings that provide response that meets the defined criteria.

a)

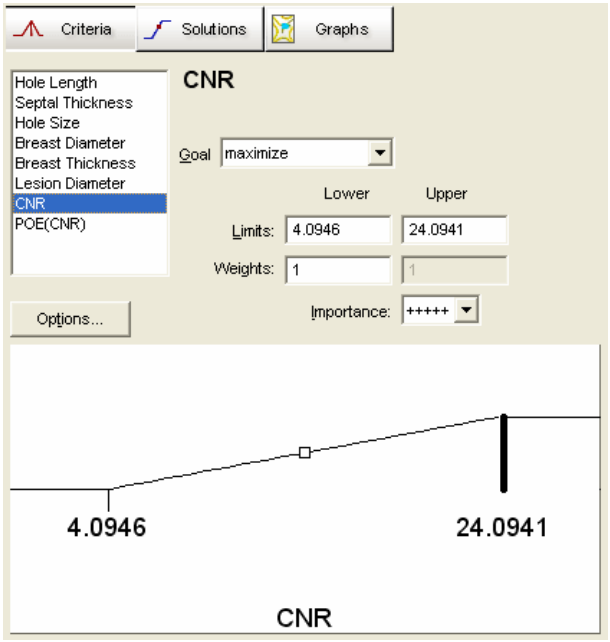

b)

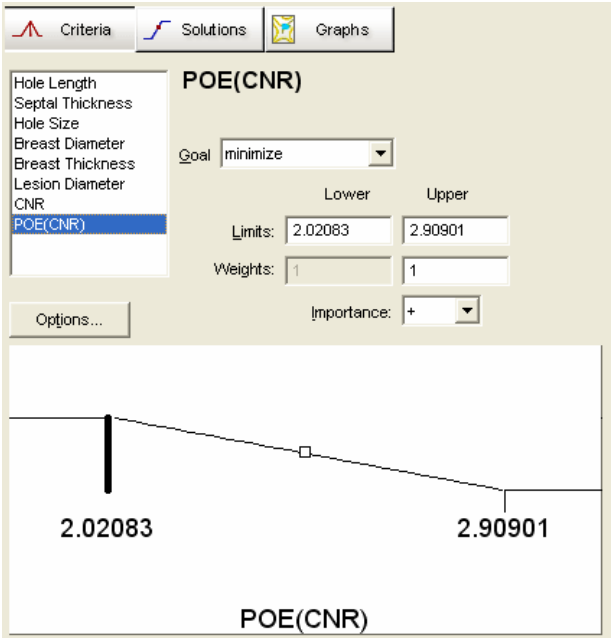

Figure 4.13 Criteria definition of robust optimization problem. a) Goal of setting CNR to maximum, weights and importance are adjusted for desirable robust optimization process. b) Goal of minimization of POE(CNR), limits of the response, weights and importance are adjusted for desirable robust optimization process.

In Table 4.3, the 79 results of robust optimization with different values of CNR and POE values are listed. The results are computed at different values of breast and lesion dimensions. From the screening experiments (described in Methods and Materials) it is well known that lesion detectability gets harder when breast dimensions get larger and lesion size gets smaller. In order to find the most robust solution set, these results are tested in SIMIND. Patient parameters are selected to get the most crucible experiment environment, where lesion size is the smallest value in design space which is 0.5cm, breast diameter and breast thickness are the largest values in the interval, 12cm and 7cm, respectively. This particular case is called as “the worst case” in the study.

Table 4.3
Design Expert outputs for robust optimization problem. Numerical optimization solutions are listed with their CNR and POE(CNR) values. These solutions are found inside the whole parameter set of breast and lesion.

Solutions Number	Hole Size	Septal Thickness	Hole Length	Breast Diameter	Breast Thickness	Lesion Diameter	CNR	POE(CNR)
1	0.29	0.02	2.95	8.00	5.00	0.66	19.23	2.68
2	0.28	0.02	2.89	8.18	5.00	0.66	19.24	2.68
3	0.30	0.02	3.09	8.00	5.00	0.66	19.25	2.68
4	0.30	0.02	3.08	8.00	5.00	0.66	19.23	2.68
5	0.32	0.02	3.21	8.00	5.00	0.66	19.24	2.68
6	0.29	0.02	2.92	8.00	5.00	0.66	19.11	2.67
7	0.30	0.02	3.09	8.00	5.00	0.66	19.26	2.68
8	0.29	0.02	2.91	8.49	5.00	0.66	19.22	2.68
9	0.25	0.02	2.67	8.38	5.00	0.66	19.22	2.68
10	0.30	0.02	2.98	8.52	5.00	0.66	19.23	2.68
11	0.26	0.03	2.66	8.25	5.00	0.66	19.19	2.68
12	0.28	0.02	2.78	8.00	5.00	0.66	19.21	2.68
13	0.31	0.02	3.22	8.46	5.00	0.66	19.22	2.68
14	0.28	0.02	2.96	8.00	5.00	0.66	19.12	2.67
15	0.30	0.02	3.13	8.70	5.00	0.66	19.16	2.68
16	0.26	0.02	2.70	8.61	5.00	0.66	19.18	2.68
17	0.30	0.02	3.02	8.84	5.00	0.66	19.23	2.68
18	0.33	0.02	3.36	8.00	5.00	0.66	19.17	2.68
19	0.24	0.03	2.49	9.07	5.00	0.66	19.21	2.68
20	0.29	0.02	2.99	8.94	5.00	0.66	19.22	2.68
21	0.30	0.02	3.08	8.00	5.00	0.66	19.18	2.68
22	0.31	0.02	3.20	9.10	5.00	0.66	19.22	2.68
23	0.29	0.02	3.01	9.30	5.00	0.66	19.20	2.68
24	0.30	0.02	3.00	8.13	5.01	0.66	19.25	2.68
25	0.29	0.02	2.93	8.03	5.00	0.66	19.20	2.68
26	0.27	0.02	2.73	8.02	5.00	0.66	19.22	2.68
27	0.29	0.03	3.10	9.59	5.00	0.66	19.21	2.68
28	0.26	0.02	2.73	9.01	5.00	0.66	19.18	2.68
29	0.33	0.02	3.33	9.86	5.00	0.66	19.20	2.68
30	0.27	0.02	2.76	9.96	5.00	0.66	19.19	2.68
31	0.33	0.02	3.34	9.06	5.00	0.66	19.15	2.68
32	0.28	0.02	2.85	10.09	5.00	0.66	19.20	2.68
33	0.23	0.02	2.43	8.00	5.00	0.66	19.19	2.68
34	0.29	0.02	2.92	10.46	5.00	0.66	19.19	2.68
35	0.35	0.02	3.49	10.44	5.00	0.66	19.20	2.68
36	0.30	0.02	3.06	10.51	5.00	0.66	19.18	2.68
37	0.24	0.03	2.48	9.24	5.00	0.66	19.19	2.68
38	0.26	0.02	2.70	10.26	5.00	0.66	19.16	2.68
39	0.34	0.02	3.49	9.36	5.00	0.66	19.21	2.68
40	0.27	0.02	2.70	11.02	5.00	0.67	19.18	2.68
41	0.27	0.02	2.78	10.96	5.00	0.66	19.16	2.68
42	0.30	0.02	3.21	11.08	5.00	0.66	19.16	2.68
43	0.37	0.02	3.69	11.33	5.00	0.66	19.15	2.68

44	0.31	0.02	3.09	9.93	5.00	0.66	19.04	2.67
45	0.22	0.03	2.41	11.41	5.00	0.66	19.16	2.68
46	0.27	0.02	2.81	8.95	5.00	0.66	19.01	2.67
47	0.29	0.02	2.98	8.00	5.00	0.66	19.13	2.68
48	0.28	0.02	2.86	11.65	5.00	0.67	19.15	2.68
49	0.30	0.02	3.13	11.74	5.00	0.67	19.16	2.68
50	0.25	0.03	2.64	12.00	5.00	0.67	19.16	2.68
51	0.21	0.03	1.99	12.00	5.00	0.67	19.15	2.68
52	0.21	0.03	2.30	12.00	5.00	0.67	19.19	2.69
53	0.19	0.03	1.95	8.04	5.04	0.66	19.12	2.68
54	0.35	0.02	3.38	8.00	5.00	0.66	19.03	2.67
55	0.24	0.02	2.46	8.00	5.00	0.66	19.03	2.67
56	0.17	0.03	1.94	12.00	5.00	0.67	19.25	2.69
57	0.40	0.01	3.91	11.74	5.00	0.67	19.17	2.69
58	0.38	0.01	3.85	12.00	5.00	0.67	19.09	2.68
59	0.18	0.02	1.90	12.00	5.02	0.67	19.06	2.68
60	0.21	0.03	2.22	8.25	5.00	0.66	18.97	2.67
61	0.15	0.03	1.65	8.00	5.00	0.66	18.83	2.66
62	0.36	0.02	3.90	12.00	5.00	0.67	19.01	2.68
63	0.14	0.03	1.66	9.93	5.00	0.66	19.09	2.68
64	0.16	0.03	1.72	12.00	5.00	0.67	19.14	2.69
65	0.39	0.02	3.99	12.00	5.00	0.66	18.80	2.66
66	0.15	0.02	1.61	8.00	5.00	0.66	18.99	2.68
67	0.14	0.02	1.74	8.00	5.01	0.66	19.06	2.68
68	0.18	0.04	1.94	8.01	5.00	0.66	18.92	2.68
69	0.11	0.03	1.14	8.96	5.00	0.66	18.80	2.67
70	0.11	0.03	1.33	12.00	5.00	0.66	18.93	2.68
71	0.11	0.02	1.18	11.88	5.00	0.67	19.09	2.69
72	0.16	0.04	1.43	9.97	5.00	0.67	18.85	2.67
73	0.28	0.03	2.09	9.68	5.00	0.66	18.41	2.64
74	0.36	0.04	3.60	10.04	5.00	0.67	18.88	2.69
75	0.27	0.01	3.34	8.52	5.00	0.67	18.81	2.68
76	0.16	0.01	1.56	12.00	5.00	0.66	18.36	2.65
77	0.26	0.05	2.83	9.49	5.00	0.65	18.31	2.64
78	0.19	0.04	2.36	12.00	5.00	0.66	18.44	2.67
79	0.14	0.05	1.07	11.54	5.00	0.67	18.80	2.70

Table 4.4
Simulation results of robust optimization solution set. Simulations are accomplished with the noise parameters that define the hardest situation for lesion detectability.

Solutions Number	Hole Size	Septal Thickness	Hole Length	CNR(Simulation Result)
1	0.29	0.02	2.95	7.02
2	0.28	0.02	2.89	7.1221
3	0.30	0.02	3.09	6.9377
4	0.30	0.02	3.08	6.9317
5	0.32	0.02	3.21	6.7999
6	0.29	0.02	2.92	6.9997
7	0.30	0.02	3.09	6.9377
8	0.29	0.02	2.91	6.9987
9	0.25	0.02	2.67	7.3749
10	0.30	0.02	2.98	6.9256
11	0.26	0.03	2.66	7.0519
12	0.28	0.02	2.78	7.1087
13	0.31	0.02	3.22	6.892
14	0.28	0.02	2.96	6.9795
15	0.30	0.02	3.13	6.9704
16	0.26	0.02	2.70	7.285
17	0.30	0.02	3.02	6.938
18	0.33	0.02	3.36	6.7321
19	0.24	0.03	2.49	7.181
20	0.29	0.02	2.99	7.0445
21	0.30	0.02	3.08	6.9419
22	0.31	0.02	3.20	6.88
23	0.29	0.02	3.01	7.049
24	0.30	0.02	3.00	6.9173
25	0.29	0.02	2.93	7.0449
26	0.27	0.02	2.73	7.1549
27	0.29	0.03	3.10	6.8655
28	0.26	0.02	2.73	7.279
29	0.33	0.02	3.33	6.7183
30	0.27	0.02	2.76	7.1863
31	0.33	0.02	3.34	6.7268
32	0.28	0.02	2.85	7.0701
33	0.23	0.02	2.43	7.5536
34	0.29	0.02	2.92	7.0346
35	0.35	0.02	3.49	6.5581
36	0.30	0.02	3.06	6.9567
37	0.24	0.03	2.48	7.1663
38	0.26	0.02	2.70	7.2776
39	0.34	0.02	3.49	6.6478
40	0.27	0.02	2.70	7.1727
41	0.27	0.02	2.78	7.2016
42	0.30	0.02	3.21	6.9661
43	0.37	0.02	3.69	6.4059

44	0.31	0.02	3.09	6.8578
45	0.22	0.03	2.41	7.3605
46	0.27	0.02	2.81	7.2115
47	0.29	0.02	2.98	7.022
48	0.28	0.02	2.86	7.1005
49	0.30	0.02	3.13	6.9925
50	0.25	0.03	2.64	7.1403
51	0.21	0.03	1.99	7.2618
52	0.21	0.03	2.30	7.4165
53	0.19	0.03	1.95	7.4617
54	0.35	0.02	3.38	6.5736
55	0.24	0.02	2.46	7.4315
56	0.17	0.03	1.94	7.6438
57	0.40	0.01	3.91	6.0971
58	0.38	0.01	3.85	6.2436
59	0.18	0.02	1.90	7.9159
60	0.21	0.03	2.22	7.374
61	0.15	0.03	1.65	7.7004
62	0.36	0.02	3.90	6.5151
63	0.14	0.03	1.66	7.7532
64	0.16	0.03	1.72	7.6425
65	0.39	0.02	3.99	6.2718
66	0.15	0.02	1.61	8.1199
67	0.14	0.02	1.74	8.2563
68	0.18	0.04	1.94	7.2129
69	0.11	0.03	1.14	7.6195
70	0.11	0.03	1.33	7.7674
71	0.11	0.02	1.18	8.2079
72	0.16	0.04	1.43	7.0158
73	0.28	0.03	2.09	6.5294
74	0.36	0.04	3.60	6.1989
75	0.27	0.01	3.34	7.3614
76	0.16	0.01	1.56	8.1066
77	0.26	0.05	2.83	6.5944
78	0.19	0.04	2.36	7.2767
79	0.14	0.05	1.07	6.2417

The 67th solution in Table 4.8, gives the highest CNR value. A hole length of 1.74cm, a septal thickness of 0.02cm and a hole size of 0.14cm is the optimum solution for the second part of the study. This point defines the parameters of robust collimator.

In Figure 4.14, this point of optimum is showed in ramp graphs of hole length, septal thickness and hole size with red dots. Noise parameters are kept in their average values, 10cm for breast diameter, 6cm for breast thickness and 0.6cm for lesion diameter.

The response, CNR, at this optimum point is marked with a blue dot on the ramp graph of CNR. The POE(CNR) found in this optimization process is marked with blue dot on the ramp graph of POE(CNR).

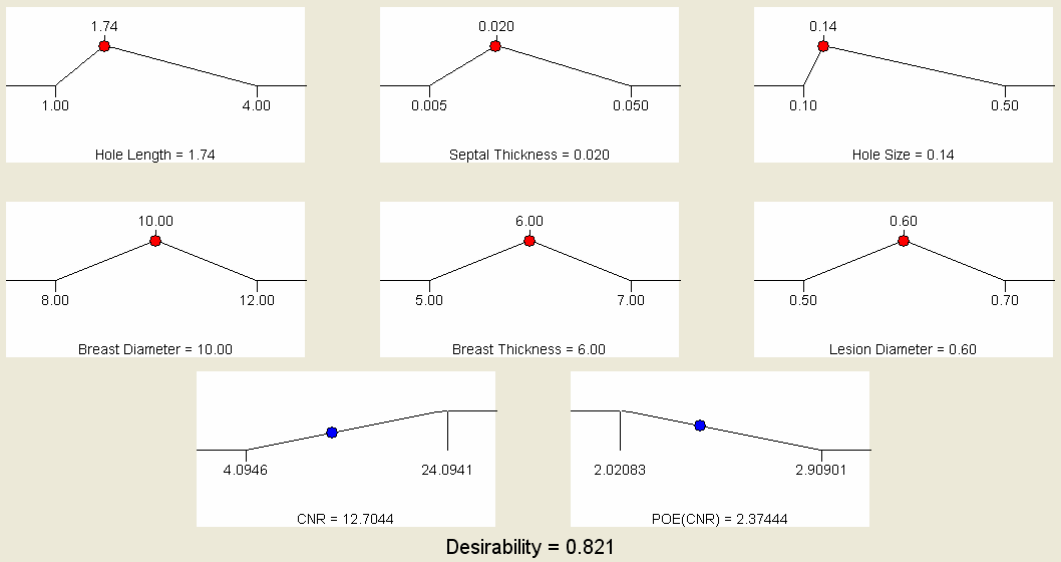

Figure 4.14 Ramp graphs of the solution of robust optimization problem. The optimum point is marked with red dots on collimator parameter graphs. Patient parameters are at their average value in the design space. The last two graphs show the corresponding CNR value of these robust collimator parameters on the response ramp graph and on the propagation of error graph.

In Figure 4.15 (a), the corresponding CNR value of robust collimator parameters is pointed out with a flag on the contour plot of CNR with respect to hole length and septal thickness (hole size is kept constant at its optimum value of 0.14cm). In order to visualize the system behavior, breast and lesion parameters are kept constant at their average values in design space. Same plot is displayed in three dimensions in Figure 4.15 (b). Although, this demonstration is not as useful as the contour plot for establishing responses values and coordinates, it provides a clearer view of the surface.

In an analogous way, Figure 4.16 (a) shows the corresponding CNR value of robust collimator parameters on the contour plot of CNR with respect to hole length and hole size. Finally, Figure 4.16 (b) shows the same point in a response surface plot of CNR with respect to hole length and hole size while septal thickness is kept constant at 0.02cm.

Breast and lesion parameters are constant at their average values (breast diameter of 10cm, breast thickness of 6cm and lesion diameter of 0.6cm)

a)

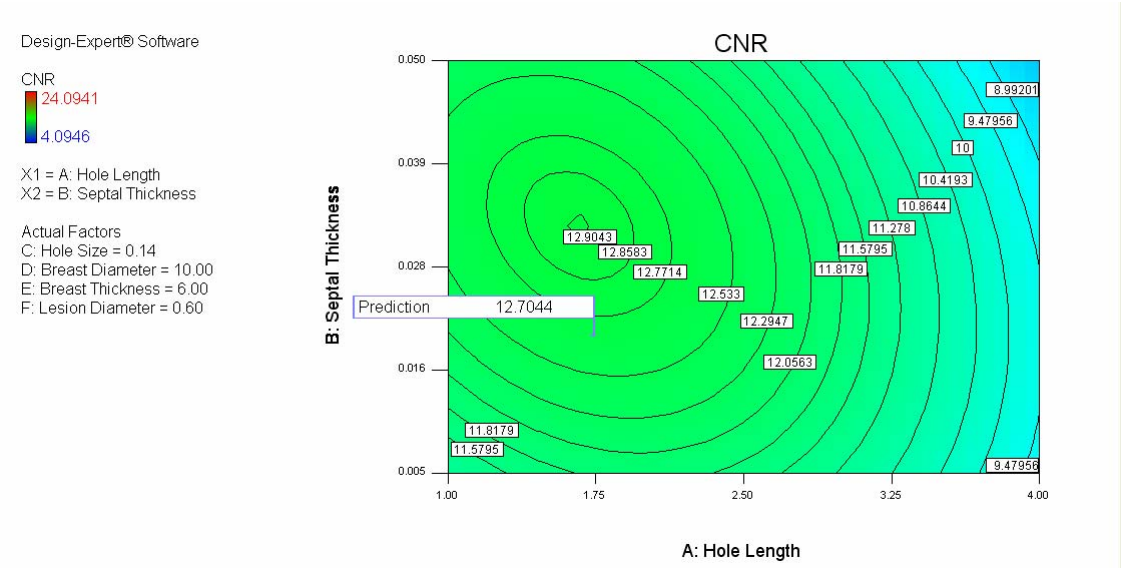

b)

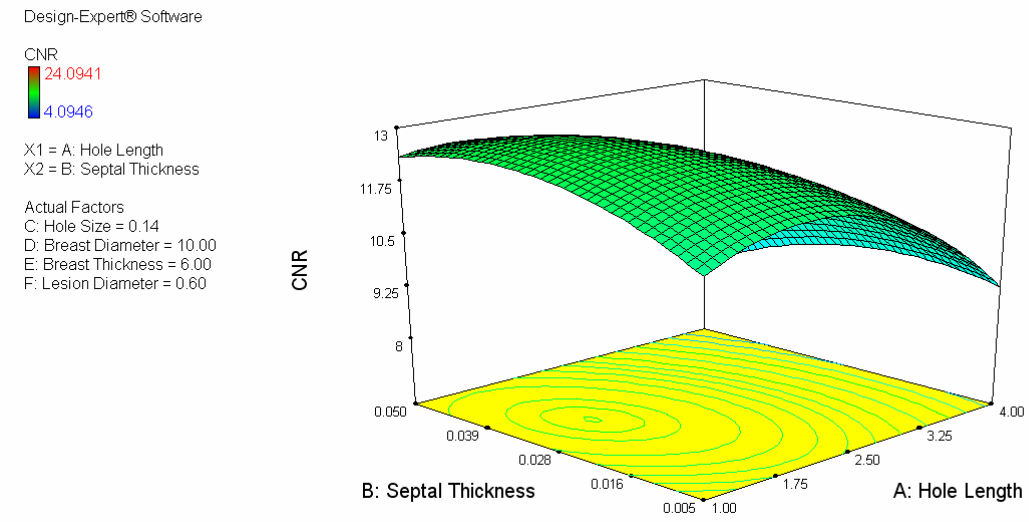

Figure 4.15 Solution graphs of robust problem with respect to hole length and septal thickness while hole size is kept constant at 0.14cm. a) Contour plot of optimum CNR. b) Response surface plot of optimum CNR with respect to robust collimator parameters.

a)

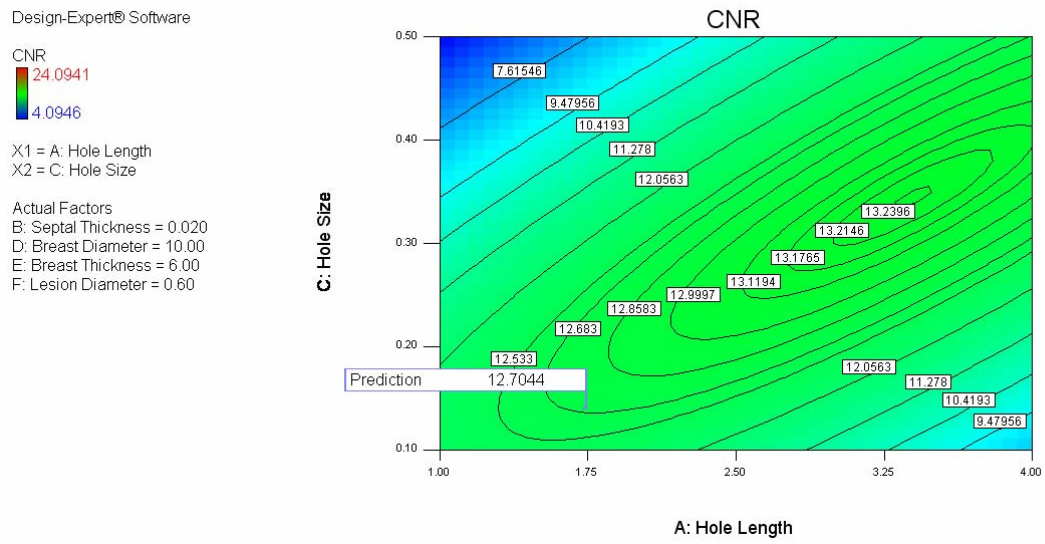

b)

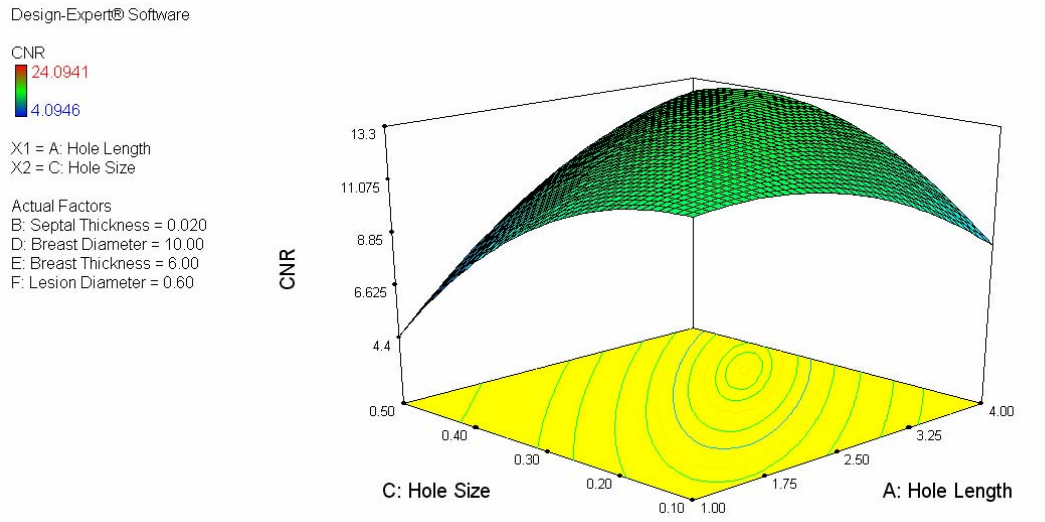

Figure 4.16 Solution graphs of robust problem with respect to hole length and hole size. a) Contour plot of optimum CNR with respect to robust hole length and hole size parameters while septal thickness is kept constant at 0.02cm. The optimum predicted CNR value (12.7044) for the noise parameter set (breast diameter of 10cm, breast thickness of 6cm and lesion diameter of 0.6cm) is marked with a flag. b) Response surface plot of optimum CNR with respect to robust collimator parameters (Septal thickness is kept constant).

In Figure 4.17 (a), the corresponding POE(CNR) value (2.3744) of robust collimator parameters is pointed out with a flag on the contour plot of POE(CNR) with respect to hole length and septal thickness (hole size is kept constant at its optimum value of 0.14cm). Same plot is displayed in three dimensions in Figure 4.17 (b).

In an analogous way, Figure 4.18 (a) shows the corresponding POE(CNR) value of robust collimator parameters on the contour plot of CNR with respect to hole length and hole size. Finally, Figure 4.18 (b) shows the same point in a response surface plot of POE(CNR) with respect to hole length and hole size while septal thickness is kept constant at 0.02cm.

a)

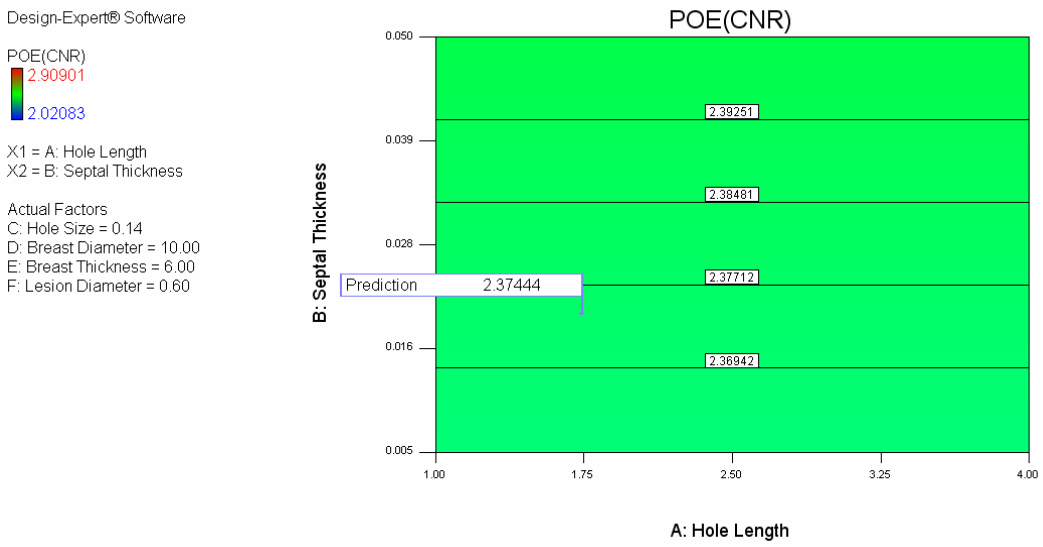

b)

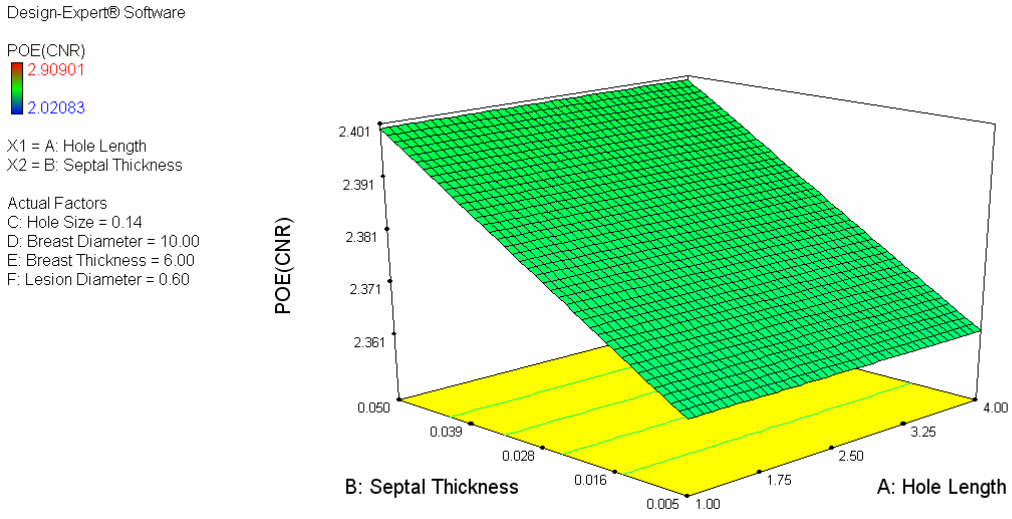

Figure 4.17 POE(CNR) plots of robust problem with respect to hole length and septal thickness. a) Contour plot of optimum POE(CNR) with respect to robust hole length and septal thickness parameters while hole size is kept constant at 0.14. The optimum predicted POE(CNR) value (2.3744) is marked with a flag at the point of average noise parameters. b) Response surface plot of optimum POE(CNR) with respect to robust collimator parameters (Hole size is kept constant).

a)

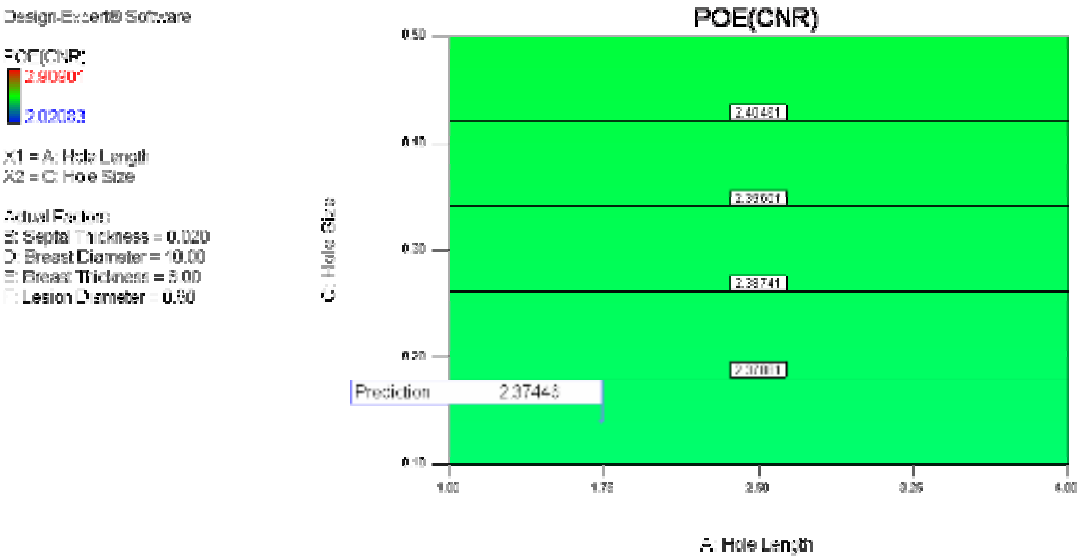

b)

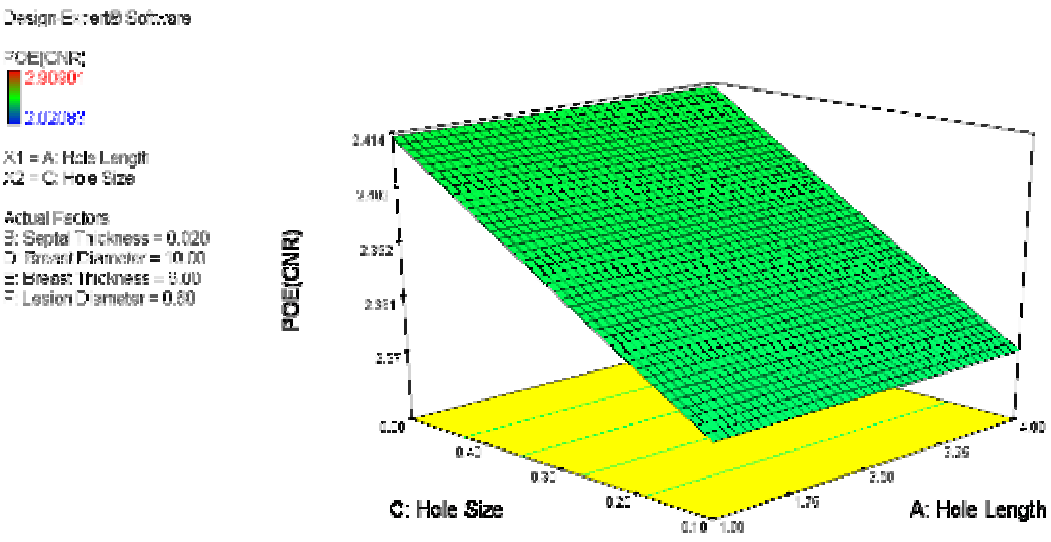

Figure 4.18 POE(CNR) plots of robust problem with respect to hole length and hole size. a) Contour plot of optimum POE(CNR) with respect to robust hole length and hole size parameters while septal thickness is kept constant at 0.02cm. The optimum predicted POE(CNR) value (2.3744) is marked with a flag at the point of average noise parameters. b) Response surface plot of optimum POE(CNR) with respect to robust collimator parameters (Septal thickness is kept constant).

In Figure 4.19 (a), the contour plot of CNR with respect to hole length and septal thickness (hole size is kept constant at its optimum value of 0.14cm) and the contour plot of POE(CNR) are superimposed. In an analogous way, Figure 4.19 (b) shows the superimposed contour plot of CNR and POE(CNR) with respect to hole length and hole size. The optimum point is shown with flags on both graphs. The red lines indicate POE contours and black lines represent CNR contours. The maximum of CNR does not coincide with the minimum of POE. From the graph, it is shown that POE gets smaller with decreasing septal thickness. However, CNR ascends and creates a peak point above the minimum POE contour. In order to find the robust collimator parameter set, a compromise between them is made.

a)

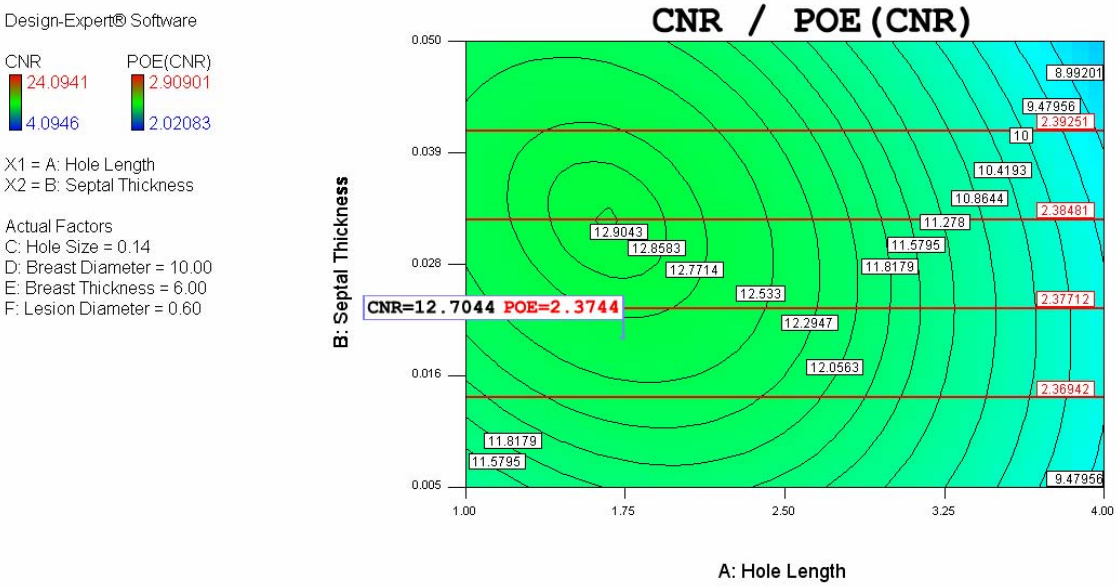

b)

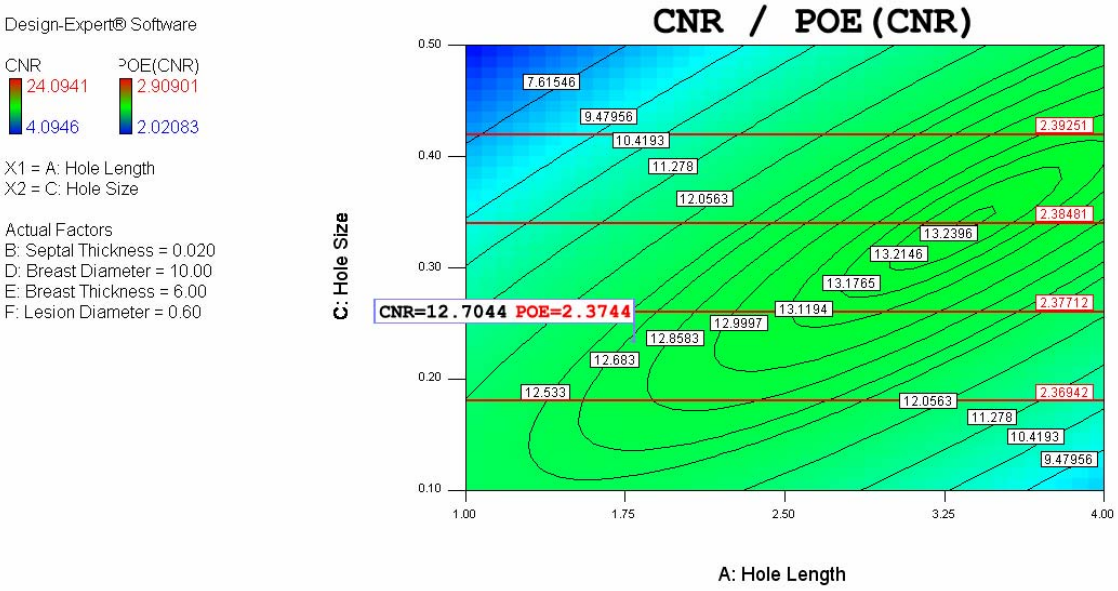

Figure 4.19 Superimposed plots of CNR and POE(CNR) graphs a) Contour plot of optimum CNR and POE(CNR) with respect to robust hole length and septal thickness parameters. The optimum predicted POE(CNR) value (2.3744) and the optimum CNR value (12.7044) are marked with a flag in the design space. b) Contour plot of optimum CNR and POE(CNR) with respect to robust hole length and hole size parameters. The optimum predicted POE(CNR) value (2.3744) and the optimum CNR value (12.7044) are showed by a flag in the design space.

4.2.3 Comparison of Results with Commercial collimators

The results of robust optimization operation are compared with the commercial collimator parameters in light of performance measures CNR and relative improvement (Table 4.5, Table 4.6, and Table 4.7) in three particular parameter sets.

4.2.3.1 <u>Comparison with commercial collimators - the worst case.</u> The first set, named as “the worst case” consists of largest breast dimensions and the smallest lesion size in which lesion detection is at its most difficult state. Since breast diameter varies between 8cm to 12cm, 12cm is chosen to define this state. Breast thickness is in its largest value of 7cm. Lesion size is selected as 0.5cm from the [0.5cm, 0.7cm] interval used in this study.

Table 4.5 shows the typical and commercially operated collimator configurations and their simulated performances in the worst case conditions. The robust collimator, whose parameters are derived in this study, is compared with these commercial collimators in terms of CNR and relative improvement. Relative improvement describes the performance between an individual collimator with respect to the robust collimator.

Table 4.5
Comparison of robust collimator with commercial collimators in the worst case. The worst case is defined as the case where lesion detectability is in its hardest state. Breast dimensions take the largest and lesion dimensions take its smallest value.

Collimator	Hole Size (cm)	Septa (cm)	Hole Length (cm)	Breast Dia. (cm)	Breast Thick. (cm)	Lesion Dia. (cm)	CNR	Relative Improvement
A	0.250	0.030	4.100	12	7	0.5	6.929	19.16%
B	0.140	0.018	2.920	12	7	0.5	7.671	7.64%
C	0.140	0.020	2.540	12	7	0.5	7.914	4.33%
D	0.170	0.020	3.500	12	7	0.5	7.370	12.02%
E	0.130	0.020	3.500	12	7	0.5	6.723	22.80%
F	0.111	0.016	2.360	12	7	0.5	7.871	4.90%
G	0.145	0.020	2.410	12	7	0.5	8.035	2.76%
ROBUST	0.140	0.020	1.740	12	7	0.5	8.2563	

Figure 4.20 summarizes the results of Table 4.5 and shows the collimators' performances by means of CNR in a column graph in the worst case.

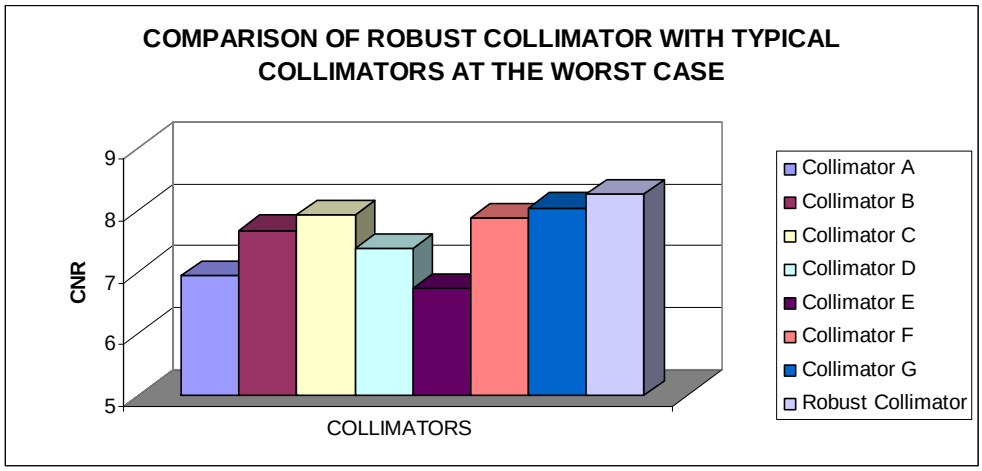

Figure 4.20 Performances of commercial collimators and the robust collimator at worst case, where breast is large and lesion is small. The performance of robust collimator is compared with commercial collimators in the worst case of lesion detectability.

4.2.3.2 <u>Comparison with commercial collimators - typical case.</u> The second set, named as “the typical case” or “the average case” consists of average breast and lesion dimensions of the design space. Since breast diameter varies between 8cm to 12cm, 10cm is chosen to define this state. Breast thickness is in its mean value of 6cm. Lesion size is selected as 0.6cm from the center of the [0.5cm, 0.7cm] interval used in this study.

Table 4.6 shows the typical and commercially operated collimator configurations and their simulated performances in the average case conditions. The robust collimator, whose parameters are derived in this study, is compared with these commercial collimators in terms of CNR and relative improvement.

Table 4.6
Comparison of robust collimator with commercial collimators in the average case. The average case is defined as the case where lesion detectability is in its moderate state.

Collimator	Hole Size (cm)	Septa(cm)	Hole Length (cm)	Breast Dia. (cm)	Breast Thick. (cm)	Lesion Dia. (cm)	CNR	Relative Improvement
A	0.25	0.03	4.1	10	6	0.6	12.717	22.62%
B	0.14	0.018	2.92	10	6	0.6	13.121	18.84%
C	0.14	0.02	2.54	10	6	0.6	13.915	12.06%
D	0.17	0.02	3.5	10	6	0.6	12.792	21.90%
E	0.13	0.02	3.5	10	6	0.6	11.036	41.30%
F	0.111	0.016	2.36	10	6	0.6	13.288	17.35%
G	0.145	0.02	2.41	10	6	0.6	14.11	10.51%
ROBUST	0.14	0.02	1.74	10	6	0.6	15.593	

Figure 4.21 summarizes the results of Table 4.6 and shows the collimators’ performances by means of CNR in a column graph in the average case.

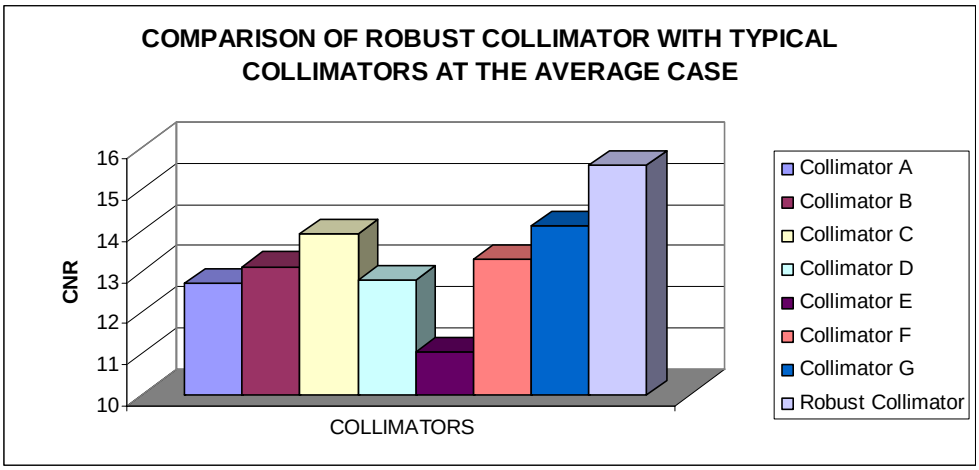

Figure 4.21 Performances of commercial collimators and the robust collimator at average case, where breast and lesion dimensions are at their mean values. The performance of robust collimator is compared with commercial collimators at the moderate case of lesion detectability.

4.2.3.3 <u>Comparison with commercial collimators - the best case.</u> The third set, named as "the best case" consists of smallest breast dimensions and the largest lesion size in which lesion detection is at its easiest state in the design space of the study. Since breast diameter varies between 8cm to 12cm, 8cm is chosen to define this state. Breast thickness is in its smallest value of 5cm. Lesion size is selected as 0.7cm from the maximum of the [0.5cm, 0.7cm] interval used in this study.

Table 4.7 shows the typical and commercially operated collimator configurations and their simulated performances in the best case conditions. The robust collimator, whose parameters are derived in this study, is compared with these commercial collimators in terms of CNR and relative improvement.

Table 4.7
Comparison of robust collimator with commercial collimators in the best case. The best case is defined as the case where lesion detectability is in its easiest state.

Collimator	Hole Size (cm)	Septal Thick. (cm)	Hole Length (cm)	Breast Dia. (cm)	Breast Thick. (cm)	Lesion Dia. (cm)	CNR	Relative Improvement
A	0.25	0.03	4.1	8	5	0.7	23.395	25.33%
B	0.14	0.018	2.92	8	5	0.7	23.462	24.97%
C	0.14	0.02	2.54	8	5	0.7	25.203	16.34%
D	0.17	0.02	3.5	8	5	0.7	23.026	27.34%
E	0.13	0.02	3.5	8	5	0.7	19.452	50.73%
F	0.111	0.016	2.36	8	5	0.7	23.734	23.54%
G	0.145	0.02	2.41	8	5	0.7	26.344	10.15%
ROBUST	0.14	0.02	1.74	8	5	0.7	29.321	

Figure 4.22 summarizes the results of Table 4.7 and shows the collimators' performances by means of CNR in a column graph in the best case.

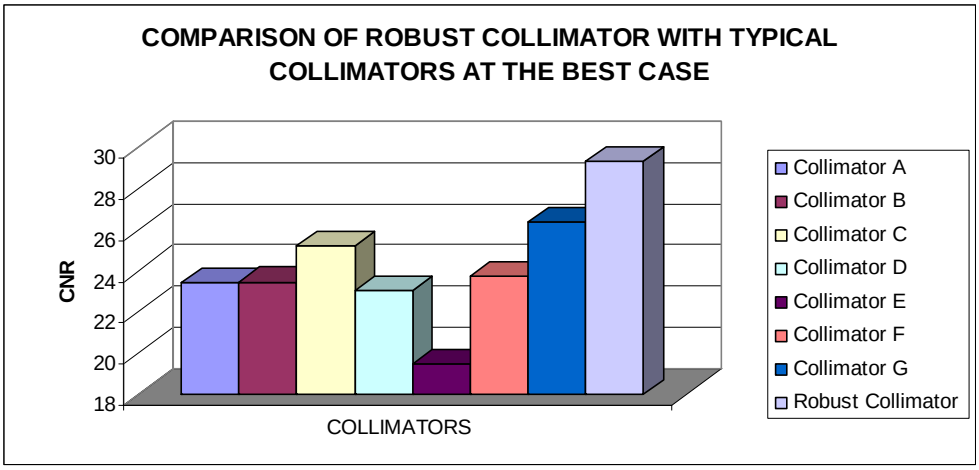

Figure 4.22 Performances of commercial collimators and the robust collimator in the best case, where breast is small and lesion is large. The performance of robust collimator is compared with commercial collimators at the best state of lesion detectability.

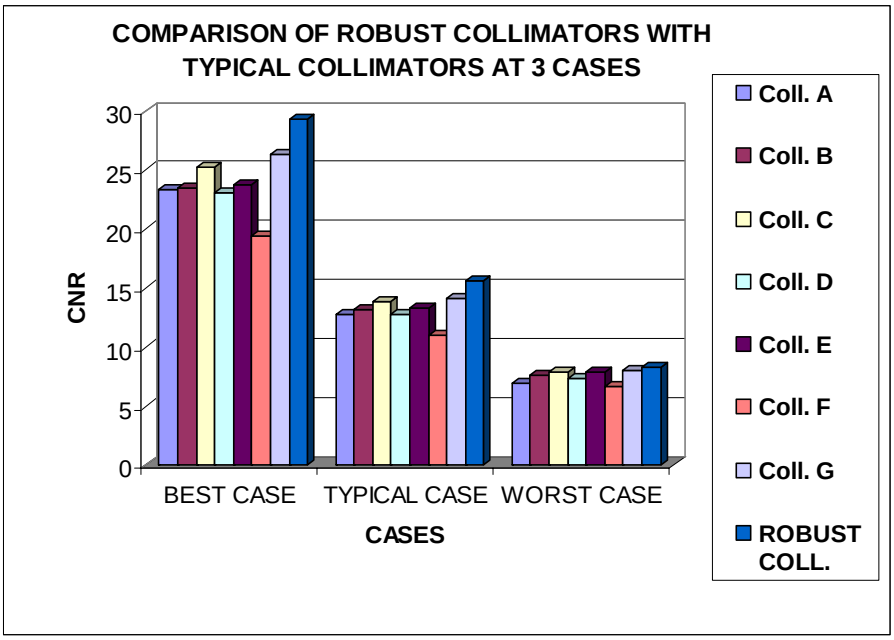

Figure 4.23 Comparison of the robust collimator with commercial collimators at three cases of breast and lesion parameter sets.

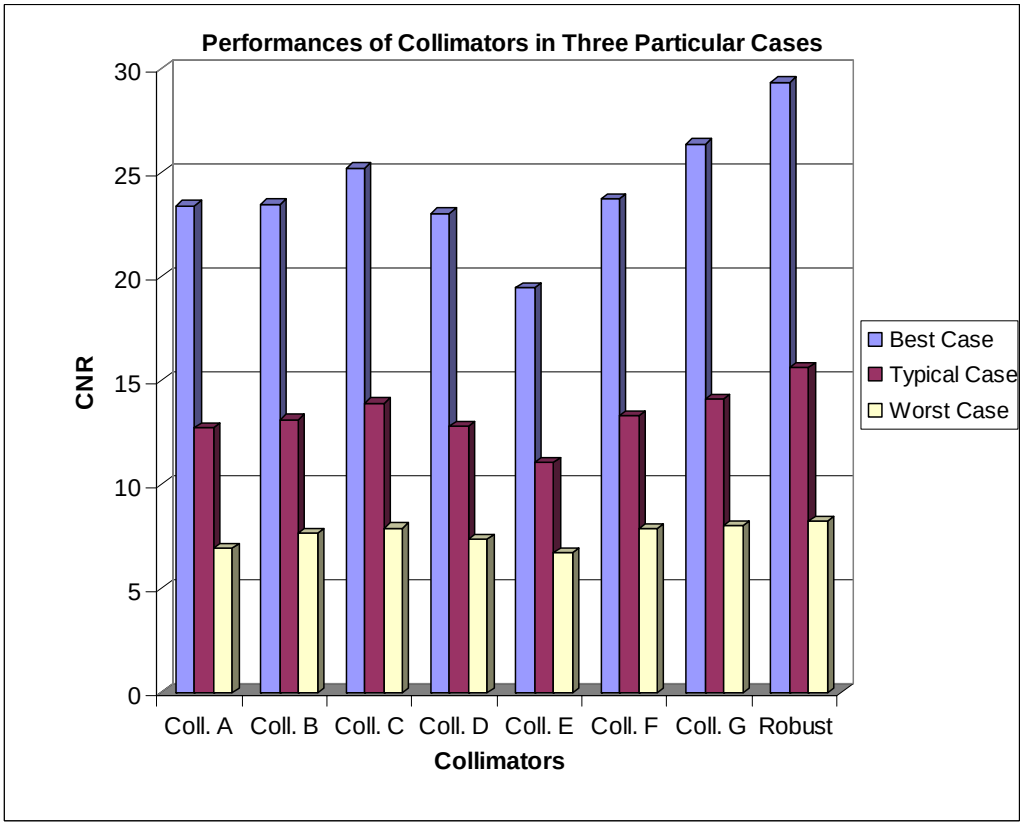

Figure 4.24 The performances of collimators at the best, at the typical, and the worst cases.

4.2.3.4 <u>Results at the three particular cases with simulated images.</u> In order to see if the numerical results in Table 4.5 coincide with simulation results, SIMIND is utilized. The images in Figure 4.25 are achieved by the simulations of our phantom model in SIMIND by using commercial collimators A, B, C, D, E, F, G and the robust collimator derived in this study in the worst case. Last image, which is the resultant image of the robust collimator simulation, gives the best lesion detectability with a CNR of 8.256.

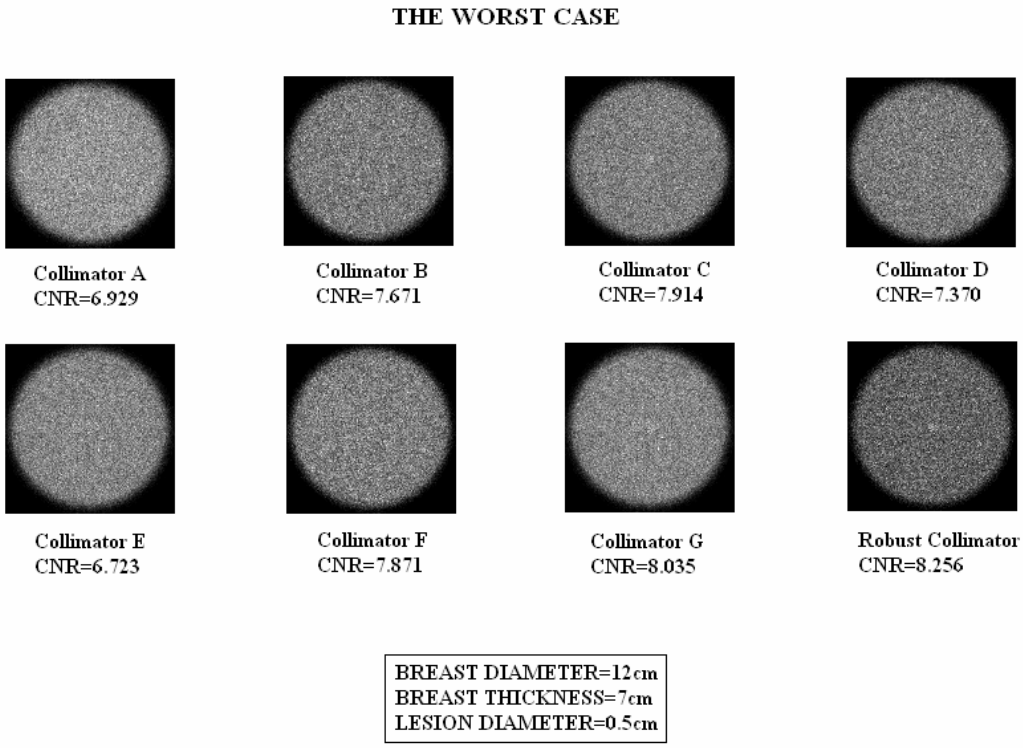

Figure 4.25 Simulation results of the commercial collimators and the robust collimator in the worst case. The breast parameters are at their largest values and lesion diameter is at its smallest grade inside the design interval of the study.

The compatibility of numerical results in Table 4.6 and the simulated images' quality is tested via SIMIND. The images in Figure 4.26 are achieved by the simulations of our phantom model in SIMIND by using commercial collimators A, B, C, D, E, F, G and optimum collimator derived in this study in the typical case. Last image, which is the resultant image of the robust collimator simulation, gives the best lesion detectability with a CNR of 15.593.

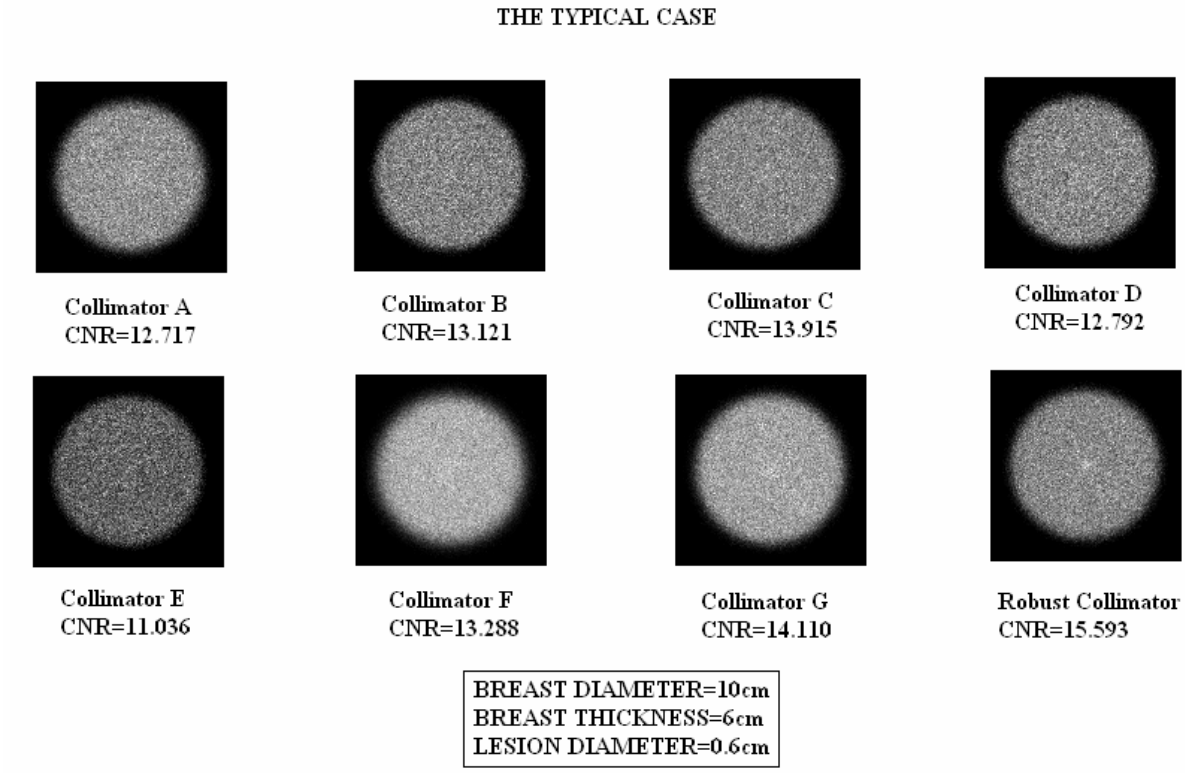

Figure 4.26 Simulation results of the commercial collimators and the robust collimator in the typical case. The breast parameters and lesion diameter are at their average values inside the design interval of the study.

The collimators in Table 4.7 are simulated and the resultant images are displayed in Figure 4.27. The simulations are achieved in the best case where breast diameter is 8cm, breast thickness is 5cm and lesion diameter is 0.7cm. The final image in Figure 4.27 represents the result of the robust collimator simulation which gives the best lesion detectability with a CNR of 29.321.

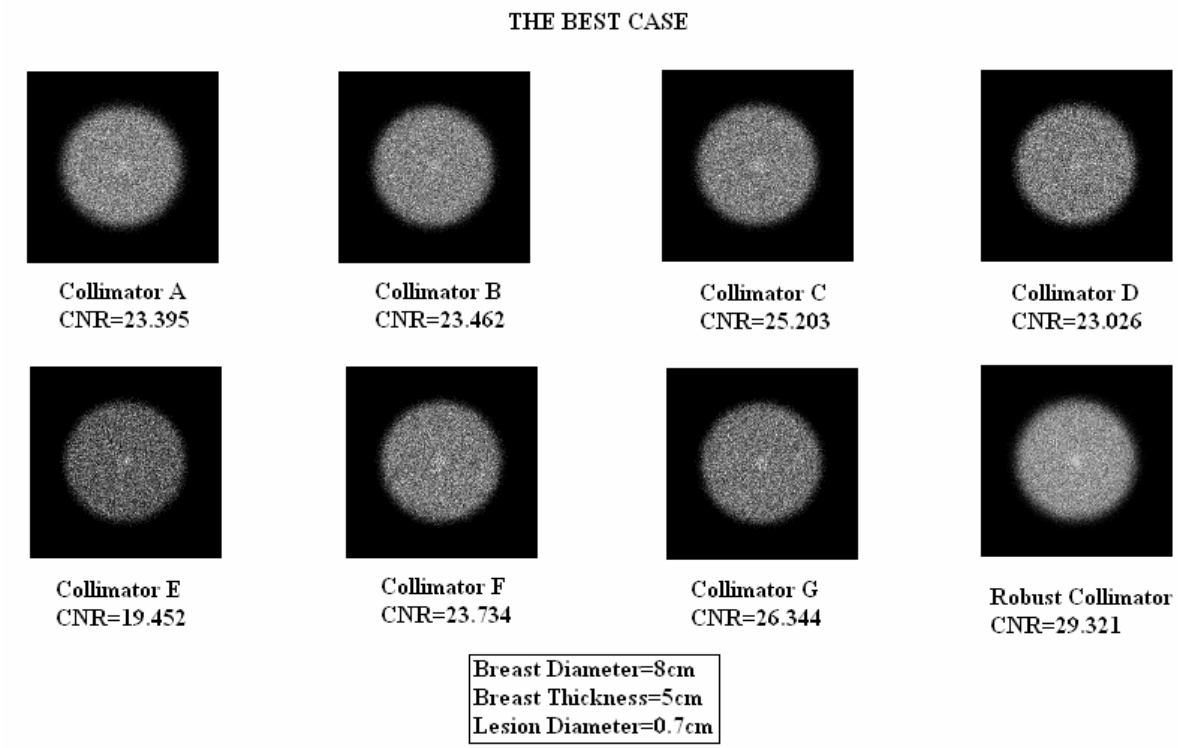

Figure 4.27 Simulation results of the commercial collimators and the robust collimator in the best case. The breast parameters are at their smallest values and lesion diameter is at its largest grade inside the design interval of the study.

5. CONCLUSION

The goal of this thesis was to design a parallel hole collimator for breast scintigraphy for the improvement of the system's lesion detection capability especially for the diagnosis of lesions smaller than 1cm. Since both sensitivity and resolution are severely affected from the changes in lesion and breast dimension parameters, the design was aimed to be robust in order to make the breast scintigraphy procedure less susceptible to the patient variation. Particularly, improvement in the robustness of the collimator was studied thoroughly in order to reduce the variance stemmed from the differences in lesion size.

The configuration of the collimator, described by three variables (hole length, hole size and septal thickness) was optimized by Response Surface Methodology via a statistical Design of Experiments software Design Expert. Considering that realization of the experiments in the clinic would take long time and labor, the experiments was conducted by utilizing Monte Carlo simulation software, SIMIND, which gave the chance of modifying both the collimator parameters and patient parameters in an unlimited way. Contrast-to-noise ratio was used as the lesion detectability, as well as the response of the system.

The study was divided into two related parts named as typical optimization problem and robust optimization problem. In the typical optimization problem, the objective was to find the optimum collimator parameter set that defines the maximum response of the system with a constant patient parameter set. For this purpose, the breast was modeled as a cylinder with a diameter of 10cm and a thickness of 6cm. Lesion was a sphere with a 0.6cm diameter. A hole length of 2.444cm, a hole size of 0.259cm and a septal thickness of 0.024cm were obtained as the solution set of the typical optimization problem. These results were compared with the performances of commercial collimators in Table 4.2 and Figure 4.9 and it was clear that optimum collimator set provide an improvement varies from 2% to 30.41% in lesion detectability relative to them. In Figure 4.10, the images

achieved by these collimators and the optimum collimator are compared. The lesion detectability index, CNR had the highest value of 14.393 after the simulation of optimum collimator and the image quality was better than the others in accordance.

In the second part of the study, called the robust optimization problem, the variances of breast and lesion dimensions were taken into account in order to simulate the clinical conditions in a more realistic way. To do this, breast diameter and breast thickness were varied between 8cm and 12cm with a standard variation of 0.67cm and 5cm and 7cm with a standard deviation of 0.34cm, respectively. Lesion diameter was alteration was 0.5cm to 0.7cm with a standard deviation of 0.034cm. A hole length of 1.74cm, a hole size of 0.14cm and a septal thickness of 0.02cm were obtained as the solution set of the robust optimization problem. These results were compared with commercial collimators in three particular states of patient variables. In the first case, which was called as the worst case in the study, the lesion detectability had the lowest grade where breast had the largest and the lesion had the smallest values inside the design space (breast diameter=12cm, breast thickness=7cm, lesion diameter=0.5cm). This case was significant for this study because the robustness of the system mostly affects the lesion detection performance in this situation. Table 4.5 and Figure 4.20 demonstrated the difference in the quality of the images achieved by simulation. The robust collimator set provided an enhancement in a range between 2.76% to 22.80% when the simulation results were compared. The simulated images were displayed in Figure 4.25, where robust collimator had its highest value of CNR (8.2563) among others. In the second part, which was called as the typical case, the breast and lesion parameters were at their average values of their design intervals. The best lesion detectability has been achieved from the simulation of the robust collimator with an improvement of 10.51% to 41.30% with respect to the commercial collimators. The last section which dealt with the case which is the easiest situation of lesion detection (Breast was the biggest and lesion was the smallest) was called as the best case. An enhancement of 10.15% to 25.33% was obtained by using the robust collimator relative to the commercial collimators' performances. The CNR achieved from the simulation was 29.321. The results are shown in Table 4.7 and Figure 4.22. In Figure 4.27, although all of

the collimators have sufficient performances for lesion detection, the resultant image of the simulation with robust collimator gave the clearest image.

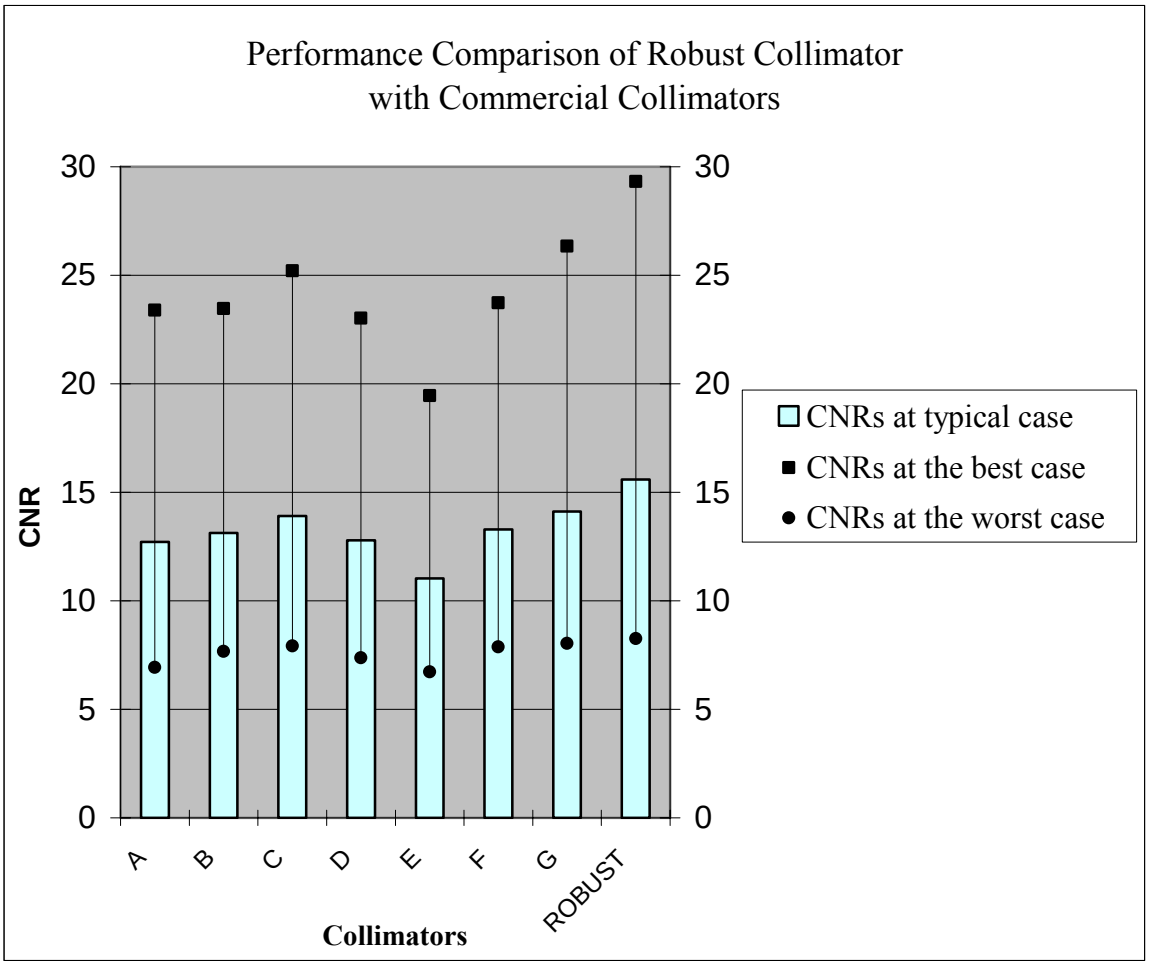

Figure 5.1 Performances of the commercial collimators A, B, C, D, E, F, G and the robust collimator at three cases. Blue bars indicate the CNRs at typical case. For each collimator, CNRs follow the black lines in the design space where black round dots indicate their maxima and black square dots are the minima.

Table 5.1
Performances of designed collimators are compared with the commercial collimators. Relative improvement in lesion detectability at different cases named as “worst”, “typical” and “best” are shown.

Collimator	Case	Breast Diameter	Breast Thickness	Lesion Size	Relative Improvement
OPTIMUM	TYPICAL	10cm	6cm	0.6cm	2% - 30.41%
ROBUST	WORST	12cm	7cm	0.5cm	2.76% - 22.80%
	TYPICAL	10cm	6cm	0.6cm	10.51% - 41.30%
	BEST	8cm	5cm	0.7cm	10.15% - 25.33%

In general, the aims of the study are realized. Table 5.1 sums up the designed collimators and their relative performance improvements according to three different patient parameter sets including the hardest, the easiest and the moderate situations of lesion detectability. Since robust collimator has the largest CNR values at all of the cases in the design space, the objective of making the system less susceptible to the changes in patient parameters while keeping the lesion detectability as high as possible is accomplished.

In literature, collimator of a gamma camera system is designed by a few methods that basically try to define an analytical relation between the system’s resolution or efficiency and collimator parameters. Then, these relations are utilized to find the solution set that makes the system’s performance maximum [13, 15]. However, each design parameter is studied individually holding all other parameters fixed. G.H. Simmons introduced a frequency dependent statistical figure of merit and combined with a weighted object distribution frequency spectrum to obtain an objective function which, when maximized, yields the optimum collimator design according to the chosen criteria. The response was fixed to find the optimum collimator parameters [16]. Sensitivity and resolution functions were combined to generate the collimator characteristics plots [19]. Generally one or two parameters are selected for collimator design as is the case with Zeng investigated a task based technique which optimized only hole diameter. Parametric survey calculation is another way of studying the optimum collimator characteristics [20, 21]. In addition, model observers, which have been successfully used to predict human observer performance and to empirically evaluate image quality for detection tasks on various backgrounds, are utilized for the collimator design process [22]. The articles have a

common feature that all of them deal with the object (the abnormality) as it is constant and does not change from patient to patient. As provided here in, this is the first study in nuclear medicine imaging area where patient variance is taken into account and Response Surface Methodology, a very common method in different industries (microchip industry, electrical device industry, pharmaceutical industry etc.), is applied for robust design of the collimator.

Furthermore, Monte Carlo Method, which is applied to the study from the perspective of the collimator realization by running simulations, is a novel tool in evaluating collimator design in addition to its quantitative clinical applications.

For future work, other uncontrollable patient parameters like lesion activity, lesion-to-collimator distance, etc can be included in the robust design procedure. Besides, the design spaces might be extended according to a clinical study that investigates the distribution of breast and lesion dimensions more accurately. In addition to that, the results of this study may be supported by a ROC analysis which provides tools to select possibly optimal models and is related in a direct and natural way to analysis of diagnostic decision making. Furthermore, the designed collimator might be manufactured and tested in a real gamma camera environment. Separately, Taguchi's Loss Function of the imaging system, which establishes a measure of the dissatisfaction with the collimator's performance as it deviates from a target value can be derived and utilized to get the robust collimator parameters.

APPENDIX A. OUTPUT FILES OF SIMULATION

A.1 OUTPUT FILE OF LESION SIMULATION

```
---------------------- SIMIND  Monte Carlo Program v4.4 ----------------------
--------------------------------------------------------------------------------
  INPUT FILE...c:\simind\si COVER........al.cr3       SOURCE FILE..smap.fso
  OUTPUT FILE..c:\simind\si CRYSTAL......nai.cr3      SOURCE MAP...
  PHANTOM (S)..h2o.cr3      BACK-SCATT...lucite.cr3   DENSITY MAP..
  PHANTOM (B)..h2o.cr3                                SCORE FILE...
---------------------------------- FLAGS ---------------------------------------
  Photon Energy             140.00   Matrix    Photons/Proj         10000000.
  Source  Type               Sphere   Spectra   Activity                 2.36
  Phantom Type       Vert Cylinder   vg-legp   Detector Radius         20.000
  Detector Width             25.000   B-Scatt   Detector Height          0.935
  Upper Window Tresh        154.000   Random    Distance to Det          7.000
  Lower Window Tresh        126.000   Phantom   X-Shift Source           0.000
  Pixel Size (I)              0.100   Resolut   Y-Shift Source           0.000
  Pixel Size (J)              0.100   Forced    Z-Shift Source           0.000
  S:Half Length               0.300             P:Half Length            5.000
  S:Half  Width               0.300             P:Half Width             5.000
  S:Half Height               0.300             P:Half Height            3.000
  Energy  Resolution         10.600             Max Scatter Ord              3
--------------------------------------------------------------------------------
  GENERAL DATA
  keV/channel                 2.000             Compiler        Windows LF95
  Photons/Bq                  0.891             Starting Angle          0.000
  Camera Offset X             0.000             Cover Thickness         0.000
  Camera Offset Y             0.000             Backscatt Thick         3.000
  Matrix Size    (I)            128             Intrinsic Res           0.380
  Matrix Size    (J)            128             Acceptance Angle  0.29769E-02
  Emission Type               2.000             Initial Weight    0.21010E+00
  "NN" Scaling Factor             1             Energy Channels           512
  Photon Exit Phantom             1

--------------------------------------------------------------------------------
  COLLIMATOR DATA FOR CODE: New M Ljungberg
  Collimator Code           vg-legp             Collimator Type      Parallel
  X:Hole Size                 0.300             X:Distance              0.021
  Y:Hole Size                 0.346             Y:Distance              0.191
  X:Center Shift              0.161             Penetration             1.000
  Y:Center Shift              0.278             Hole Length             3.060
  Focal Len/SH Angle          0.000             Coll X-section  pb.cr3
  Collimator Effic       0.298E-02              Hole Shape           Hexagonal
  Movement flag               1.000             X-Ray Flag                  0

--------------------------------------------------------------------------------
  Simulation began 2007:05:31 at 12:25:27
  Simulation ended 2007:05:31 at 12:37:04
  Elapsed time 0 h 11 min and 37 sec
--------------------------------------------------------------------------------
  INTERACTIONS IN THE CRYSTAL
  Detector Hits           8191724
  Hits/sec             11834.8115
  Maximum in Spectra      98.8911
  Maximum in Images        5.3118
  Count Rate [Total]    1370.4305
  Count Rate [Window]    829.0620

--------------------------------------------------------------------------------
  PHOTONS AFTER COLLIMATOR AND WITHIN E-WINDOW
  Geometric         95.29%              94.93%
  Penetration        3.29%               3.83%
  Scatter in coll    1.42%               1.24%
```

```
  No X-rays in collimator simulated
--------------------------------------------------------------------------------
  RESULTS FROM ENERGY SPECTRUM
  Compton Area in Spectrum   0.5317E+03     0.17%
  Photo   Area in Spectrum   0.8291E+03     0.09%
  Pileup  Area in Spectrum   0.9658E+01     1.38%
  Fraction Photo in Window       0.9703     0.09%
  Fraction Compt in Window       0.0297     1.51%

--------------------------------------------------------------------------------
  SCATTER RESULTS
  Scatter-to-Primary Ratio   0.1971E+00     0.48%
  Scatter-to-Total Ratio     0.1647E+00

  Scatter in Window by order  1   92.63%
  Scatter in Window by order  2    7.06%
  Scatter in Window by order  3    0.32%
--------------------------------------------------------------------------------
  CALCULATED DETECTOR PARAMETERS
  Efficiency   [Peak]            0.5689  0.94%
  Efficiency   [Detector]        0.0904
  Sensitivity  [Cps/MBq]       351.5954
  Sensitivity  [Cpm/uCi]       780.5418
  Peak/Compton [Peak]           82.4038
  Peak/Compton [Area]            1.5592
  Peak/Total                     0.6050
  Comment Simulation of 511 keV
  Command  C:\SIMIND\simindWeb\data\ROB_l C:\SIMIND\simindWeb\data\ROB_l
```

A.2 OUTPUT FILE OF LESION SIMULATION

```
---------------------- SIMIND  Monte Carlo Program v4.4 ----------------------
--------------------------------------------------------------------------------
  INPUT FILE...c:\simind\si COVER........al.cr3       SOURCE FILE..smap.fso
  OUTPUT FILE..c:\simind\si CRYSTAL......nai.cr3      SOURCE MAP...
  PHANTOM (S)..h2o.cr3      BACK-SCATT...lucite.cr3   DENSITY MAP..
  PHANTOM (B)..h2o.cr3                                SCORE FILE...
---------------------------------- FLAGS ---------------------------------------
  Photon Energy             140.00   Matrix    Photons/Proj         10000000.
  Source  Type       Vert Cylinder   Spectra   Activity              1742.70
  Phantom Type       Vert Cylinder   vg-legp   Detector Radius         20.000
  Detector Width            25.000   B-Scatt   Detector Height          0.935
  Upper Window Tresh       154.000   Random    Distance to Det          7.000
  Lower Window Tresh       126.000   Phantom   X-Shift Source           0.000
  Pixel Size (I)             0.100   Resolut   Y-Shift Source           0.000
  Pixel Size (J)             0.100   Forced    Z-Shift Source           0.000
  S:Half Length              4.950             P:Half Length            5.000
  S:Half  Width              4.950             P:Half Width             5.000
  S:Half Height              2.970             P:Half Height            3.000
  Energy  Resolution        10.600             Max Scatter Ord              3
--------------------------------------------------------------------------------
  GENERAL DATA
  keV/channel                2.000             Compiler        Windows LF95
  Photons/Bq                 0.891             Starting Angle           0.000
  Camera Offset X            0.000             Cover Thickness          0.000
  Camera Offset Y            0.000             Backscatt Thick          3.000
  Matrix Size    (I)           128             Intrinsic Res            0.380
  Matrix Size    (J)           128             Acceptance Angle  0.29769E-02
  Emission Type              2.000             Initial Weight    0.15527E+03
  "NN" Scaling Factor            1             Energy Channels           512
  Photon Exit Phantom            1

--------------------------------------------------------------------------------
  COLLIMATOR DATA FOR CODE: New M Ljungberg
  Collimator Code          vg-legp             Collimator Type      Parallel
```

```
  X:Hole Size               0.300            X:Distance              0.021
  Y:Hole Size               0.346            Y:Distance              0.191
  X:Center Shift            0.161            Penetration             1.000
  Y:Center Shift            0.278            Hole Length             3.060
  Focal Len/SH Angle        0.000            Coll X-section  pb.cr3
  Collimator Effic       0.298E-02           Hole Shape          Hexagonal
  Movement flag             1.000            X-Ray Flag                 0

--------------------------------------------------------------------------------
  Simulation began 2007:05:31 at 12:37:04
  Simulation ended 2007:05:31 at 12:48:31
  Elapsed time 0 h 11 min and 27 sec
--------------------------------------------------------------------------------
  INTERACTIONS IN THE CRYSTAL
  Detector Hits           8188998
  Hits/sec             11959.1064
  Maximum in Spectra   74103.1719
  Maximum in Images       97.0016
  Count Rate [Total]  900827.6880
  Count Rate [Window] 605046.0620

--------------------------------------------------------------------------------
  PHOTONS AFTER COLLIMATOR AND WITHIN E-WINDOW
  Geometric         95.23%             94.89%
  Penetration        3.40%              3.86%
  Scatter in coll    1.37%              1.25%

  No X-rays in collimator simulated
--------------------------------------------------------------------------------
  RESULTS FROM ENERGY SPECTRUM
  Compton Area in Spectrum   0.2884E+06     0.29%
  Photo   Area in Spectrum   0.6050E+06     0.25%
  Pileup  Area in Spectrum   0.7405E+04     3.65%
  Fraction Photo in Window       0.9809     0.25%
  Fraction Compt in Window       0.0191     0.61%

--------------------------------------------------------------------------------
  SCATTER RESULTS
  Scatter-to-Primary Ratio   0.1384E+00     0.70%
  Scatter-to-Total Ratio     0.1215E+00

  Scatter in Window by order  1   92.55%
  Scatter in Window by order  2    7.06%
  Scatter in Window by order  3    0.39%
--------------------------------------------------------------------------------
  CALCULATED DETECTOR PARAMETERS
  Efficiency   [Peak]            0.6278  0.93%
  Efficiency   [Detector]        0.2541
  Sensitivity  [Cps/MBq]       347.1889
  Sensitivity  [Cpm/uCi]       770.7593
  Peak/Compton [Peak]           84.3145
  Peak/Compton [Area]            2.0981
  Peak/Total                     0.6717
  Comment Simulation of 511 keV
  Command  C:\SIMIND\simindWeb\data\ROB_b C:\SIMIND\simindWeb\data\ROB_b
```

APPENDIX B. MATLAB CODE CNR AND IMAGE GENERATION

```
clear;
close all;

% Read the matrices
% Read the breast matrix from .bim file
fid=fopen('deneme8_robust_b.BIM');
[BB]=fread(fid,[128,128],'single');
status = fclose(fid);
% Read the lesion matrix from .bim file
fid=fopen('deneme8_robust_l.BIM');
[LL]=fread(fid,[128,128],'single');
status = fclose(fid);

% Correction constant for 1sec to 10min scan duration scaling
cons = 600;
[Bd] = double(cons*BB);
[Ld] = double(cons*LL);

% addition of Poisson noise and resultant image creation
RRwithNoise = imnoise(uint16(BB)+uint16(LL),'poisson');
figure, imshow(RRwithNoise,[])

% The mean value of the elements which form
% the breast region on the image is calculated here.

PbSum = 0;  a=0;
breastradius=6
for i=1:128
   for j=1:128
       if(((i-64.5)^2)+ ((j-64.5)^2) <= (breastradius*10)^2)
           PbSum = PbSum + Bd(i,j);
           a = a+1;
        end
    end
end
Pb = PbSum / a;

% The mean value of the elements which form
% the lesion region on the image is calculated here.

PlSum=0;    PlbSum=0;    b=0;
lesionradius=0.25
for i=1:128
   for j=1:128
       if(((i-64.5)^2)+ ((j-64.5)^2) <= (lesionradius*10)^2)
           PlSum = PlSum + Ld(i,j);
           b = b+1;
       end
   end
end
Pl = PlSum / b;

% Contrast calculation
contrast = Pl / Pb;

% Coise calculation
percentageSd = (1 / sqrt(Pb));

% CNR calculation
CNR= contrast/ percentageSd
```

APPENDIX C. DEFINITIONS OF ANOVA TABLE TERMS

Some statistics are only given under certain conditions or for certain designs. The ANOVA is built entirely on the premise that the factors are fixed, not random and the design is crossed, not nested. Note that you can choose View, Annotated ANOVA to provide assistance with interpretation of the results.

Block: Removes any variation attributed to the blocks prior to computing the ANOVA for the factor effects.

Sum of Squares: Sum of the squared differences between the average values for the blocks and the overall mean.

DF: Degrees of freedom attributed to the blocks, generally equal to one less than the number of blocks.

Mean Square: Estimate of the block variance, calculated by the block sum of squares divided by block degrees of freedom.

Model: Terms estimating factor effects. For 2-level factorials: those that "fall off" the normal probability line of the effects plot.

Sum of Squares: Total of the sum of squares for the terms in the model, as reported in the Effects List for factorials and on the Model screen for RSM, MIX and Crossed designs.

DF: Degrees of freedom for the model. It is the number of model terms, including the intercept, minus one.

Mean Square: Estimate of the model variance, calculated by the model sum of squares divided by model degrees of freedom.

F Value: Test for comparing model variance with residual (error) variance. If the variances are close to the same, the ratio will be close to one and it is less likely that any of the factors have a significant effect on the response. F-Value is calculated by Model Mean Square divided by Residual Mean Square.

Prob > F: Probability of seeing the observed F value if the null hypothesis is true (there is no factor effect). Small probability values call for rejection of the null hypothesis. The probability equals the proportion of the area under the curve of the F-distribution that lies beyond the observed F value. The F distribution itself is determined by the degrees of freedom associated with the variances being compared.

(In "plain English", if the Prob>F value is very small (less than 0.05) then the terms in the model have a significant effect on the response.)

Term: Each of the listed terms is currently in the model and individual statistics are calculated for them.

Sum of Squares: For factorial terms the sum of squares equation reduces to: the number of factorial experiments divided by 4 times the squared factor effect.

DF: Degrees of freedom for the term. It is the number of levels for the term, minus one.

Mean Square: Estimate of the term variance, calculated by the term sum of squares divided by term degrees of freedom.

F Value: Test for comparing term variance with residual (error) variance. If the variances are close to the same, the ratio will be close to one and it is less likely that the term has a significant effect on the response. Calculated by term Mean Square divided by Residual Mean Square.

Prob > F: Probability of seeing the observed F value if the null hypothesis is true (there is no factor effect). Small probability values call for rejection of the null hypothesis. The probability equals the proportion of the area under the curve of the F-distribution that lies beyond the observed F value. The F distribution itself is determined by the degrees of freedom associated with the variances being compared.

(In "plain English", if the Prob>F value is very small (less than 0.05) then the individual terms in the model have a significant effect on the response.)

Curvature: (2-level Factorials Only) Compares the average response of the factorial points to the average response of the center points to test for non-linearity between the factorial points.

Sum of Squares: Sum of squares for the weighted difference between the center and factorial point averages.

DF: (Degrees of freedom) Represents the amount of information used up to estimate curvature.

Mean Square: Estimate of the curvature variance, calculated by the curvature sum of squares divided by curvature degrees of freedom.

F Value: Test for comparing curvature variance with residual (error) variance. If the variances are close to the same, the ratio will be close to one and it is less likely that

curvature is significant. Calculated by curvature Mean Square divided by Residual Mean Square.

Prob > F: Probability of seeing the observed F value if the null hypothesis is true (there is no curvature). Small probability values call for rejection of the null hypothesis that curvature is not significant.

(In "plain English", if the Prob>F value is very small (less than 0.05) then curvature is significant. This means that the predicted value at the center point is significantly different than the value that is obtained when actually running the center point conditions. Generally you want the Prob>F value for curvature to be greater then 0.10.)

Residual: Consists of terms used to estimate experimental error (for 2-level factorials, the insignificant factors and interactions that fall ON the normal probability line on the Effects plot.)

Sum of Squares: This equals the sum of squares for all the terms not included in the model.

DF: The corrected total DF minus the model DF.

Mean Square: The estimate of process variance. The square root of this provides an estimate of the process standard deviation.

Lack of Fit (LOF): This is the variation of the data around the fitted model. If the model does not fit the data well, this will be significant.

Sum of Squares: Residual sum of squares after removing the pure error sum of squares.

DF: The amount of information available after accounting for blocking, model terms, curvature, and pure error.

Mean Square: Estimate of lack of fit.

F Value: Test for comparing lack of fit variance with pure error variance. If the variances are close to the same, the ratio will be close to one and it is less likely that lack of fit is significant.

Prob>F: Probability of seeing the observed F value if the null hypothesis is true. Small probability values call for rejection of the null hypothesis that lack of fit is not significant.

(In "plain English", if the Prob>F value is very small (less than 0.05) then lack of fit is significant. In other words the variation in the model points significantly differs from the variation in the replicated points. Consider adding more terms to this model. You want the Prob>F value for lack of fit to be greater then 0.10.)

Pure Error: Amount of variation in the response in replicated design points.

Sum of Squares: Pure error sum of squares from replicated points.

DF: The amount of information available from replicated points.

Mean Square: Estimate of pure error variance.

Cor Total: Totals of all information corrected for the mean.

Sum of Squares: Sum of the squared deviations of each point from the mean.

DF: Total degrees of freedom for the experiment, minus one for the mean.

Next you see a collection of summary statistics for the model:

Std Dev: (Root MSE) Square root of the residual mean square. Consider this to be an estimate of the standard deviation associated with the experiment.

Mean: Overall average of all the response data.

C.V.: Coefficient of Variation, the standard deviation expressed as a percentage of the mean. C.V. is calculated by dividing the standard deviation by the mean and multiplying by 100.

PRESS: Predicted Residual Error Sum of Squares – A measure of how the model fits each point in the design. The PRESS is computed by first predicting where each point should be from a model that contains all other points except the one in question. The squared residuals (difference between actual and predicted values) are then summed.

$$e_{i,-i} = y_i - \hat{y}_{i,-i}$$

$$e_{i,-i} = \frac{e_i}{1-h_{ii}}$$

$$\text{PRESS} = \sum_{i=1}^{n}\left(e_{i,-i}\right)^2 = \sum_{i=1}^{n}\left(\frac{e_i}{1-h_{ii}}\right)^2$$

R-Squared: A measure of the amount of variation around the mean explained by the model.

$$R^2 = 1 - \left[\frac{SS_{residual}}{(SS_{residual} + SS_{model})}\right]$$

$$= 1 - \left[\frac{SS_{residual}}{(SS_{total} - SS_{curvature} - SS_{block})}\right]$$

Adj R-Squared: A measure of the amount of variation around the mean explained by the model, adjusted for the number of terms in the model. The adjusted R-squared decreases as the number of terms in the model increases if those additional terms don't add value to the model.

$$\text{Adj } R^2 = 1 - \left[\left(\frac{SS_{residual}}{df_{residual}}\right) \Big/ \left(\frac{SS_{residual} + SS_{model}}{df_{residual} + df_{model}}\right)\right]$$

$$= 1 - \left[\left(\frac{SS_{residual}}{df_{residual}}\right) \Big/ \left(\frac{SS_{total} - SS_{curvature} - SS_{block}}{df_{total} - df_{curvature} - df_{block}}\right)\right]$$

Pred R-Squared: A measure of the amount of variation in new data explained by the model.

$$\text{Pred } R^2 = 1 - \left[\frac{PRESS}{SS_{residual} + SS_{model}}\right]$$

$$= 1 - \left[\frac{PRESS}{SS_{total} - SS_{curvature} - SS_{block}}\right]$$

The predicted R-squared and the adjusted R-squared should be within 0.20 of each other. Otherwise there may be a problem with either the data or the model. Look for outliers, consider transformations, or consider a different order polynomial.

Adequate Precision: This is a signal to noise ratio. It compares the range of the predicted values at the design points to the average prediction error. Ratios greater than 4 indicate adequate model discrimination.

$$\left[\frac{\max(\hat{Y}) - \min(\hat{Y})}{\sqrt{\bar{V}(\hat{Y})}}\right] > 4 \qquad \bar{V}(\hat{Y}) = \frac{1}{n}\sum_{i=1}^{n} V(\hat{Y}) = \frac{p\sigma^2}{n}$$

p = number of model parameters (including intercept (b0) and any block coefficients)

s2 = residual MS from ANOVA table

n = number of experiments

REFERENCES

1. Jemal, A., Tiwari, R. C., Murray, T., Ghafoor, A., Samuels, A., Ward, E., Feuer, E. J., Thun, M. J., and Society, A. C., "Cancer statistics, 2004," CA Cancer J Clin, Vol. 54(1), pp. 8–29, 2004.

2. Kadınlarda en cok gorulen 10 kanser turu,
Available: http://www.saglik.gov.tr/extras/istatistikler/apk2001/092.htm

3. Fırat, D., and Çelik, İ., "Cancer Statistics in Turkey and in the World 1993-1995," *Turkish Association For the Cancer Research and Control*, Ankara, 1998.

4. Schillaci, O., Danieli, R., Romano, P., Cossu, E., and Simonetti, G., "Clinical utility of scintimammography: From the Anger-camera to new dedicated devices," *Nuclear Instruments and Methods in Physics Research*, Vol. 569, pp. 281–285, 2006.

5. Tabár, L., Vitak, B., Chen, H. H., Yen, M. F., Duffy, S. W., and Smith, R. A., "Beyond randomized controlled trials: organized mammographic screening substantially reduces breast carcinoma mortality.", *Cancer,* Vol. 91(9), pp. 1724–1731, 2001.

6. Birdwell, R. L., Ikeda, D. M., O"Shaughnessy, K. F. & Sickles, E. A., "Mammographic characteristics of 115 missed cancers later detected with screening mammography and the potential utility of computer-aided detection," *Radiology,* Vol. 219(1), pp. 192–202, 2001.

7. Adler, D. D., and Wahl, R. L., "New methods for imaging the breast: techniques, findings, and potential," *AJR Am J Roentgenol,* Vol. 164(1), pp. 19–30, 1995.

8. Kopans, D. B., "The positive predictive value of mammography," *AJR Am J Roentgenol,* Vol. 158(3), pp. 521–526, 1992.

9. Scopinaro, F., Schillaci, O., Ussof, W., Nordling, K., Capoferro, R., Vincentis, G. D., Danieli, R., Ierardi, M., Picardi, V., Tavolaro, R., and Colella, A. C., "A three center study on the diagnostic accuracy of 99mTc-MIBI scintimammography," *Anticancer Res*, Vol. 17(3B), pp. 1631–1634, 1997.

10. Waxman, A., Nagaraj, N., Kovalevsky, M., et al., "Detection of primary breast malignancy with Tc-99m methoxyisobutylisonitrile (MIBI) in patients with nonpalpable primary malignancies: the importance of lesion size [abstract]," J Nucl Med., Vol. 36(suppl), 194P, 1995.

11. Bombardieri, E., Aktolun, C., Baum, R. P., Bishof-Delaloye, A., Buscombe, J., Chatal, J. F., Maffioli, L., Moncayo, R., Mortelmans, L., and Reske, S. N., "Breast scintigraphy: procedure guidelines for tumour imaging," *Eur J Nucl Med Mol Imaging,* Vol. 30(12), pp. 107–114, 2003.

12. Mettler, F. A., and Guiberteau, M. J., *Essentials of nuclear medicine imaging,* Philadelphia: Saunders, 1998.

13. Anger, H. O., "Scintillation camera with multichannel collimators," *J Nucl Med*, Vol. 5, pp. 515–531, 1964.

14. Keller, E. L., "Optimum dimensions of parallel-hole, multi-aperture collimators for gamma-ray cameras.", *J Nucl Med*., Vol. 9(6), pp. 233–235, 1968.

15. Walker, W. G., "Design and analysis of scintillation-camera lead collimators using a digital computer," *Medical Radioisotope Scintigraphy,* Vol. 1, pp. 545–60, 1969.

16. Simmons, G. H., Christenson, J. M., Kereiakes, J. G., and Bahr, G. K. "A non-linear programming method for optimizing parallel-hole collimator design," *Phys Med Biol.,* Vol. 20(3), pp. 771–788, 1975.

17. Zeng, G. L., and Gullberg, G. T., "A channelized-hotelling-trace collimator design method based on reconstruction rather than pojections," *IEEE Transactions on Nuclear Science,* Vol. 2, pp. 1171–1174, 2002.

18. Zeitler, G., Anton, G., Bock, A., Helbing, K., Michel T., Naumann, J., Sauer, M., and Speckner, T., "An active collimator system for a high-energy photon beam," *Nuclear Instruments and Methods in Physics Research*, Vol. 459, pp. 6–15, 2001.

19. Lowe, D., Truman, A., Kwok, H., and Bergman, A., "Optimisation of the design of round-hole parallel collimators for ultra-compact nuclear medicine imaging," *Nuclear Instruments and Methods in Physics Research,* Vol. 488 pp. 428–440, 2002.

20. Yamamuraa, N., Uritanib, A., Watanabea, K., Kawarabayashia, J., and Iguchia, T., "Development of three-dimensional gamma camera with imaging plates and multi-pinhole collimators," *Nuclear Instruments and Methods in Physics Research,* Vol. 505, pp. 577–581, 2003.

21. Giokaris, N., Loudos, G., Maintas, D., Karabarbounis, A., Spanoudaki, V., Stiliaris, E., Boukis, S., Gektin, A., Boyarintsev, A., Pedash, V., and Gayshan, V., "Crystal and collimator optimization studies of a high-resolution γ-camera based on a position sensitive photomultiplier," *Nuclear Instruments and Methods in Physics Research,* Vol. 527, pp. 134–139, 2004.

22. Moore, S. C., Kijewski, M. F., and Fakhri, G. E., "Collimator optimization for detection and quantitation tasks: application to gallium-67 imaging," *IEEE Trans Med Imaging,* vol. 24(10), pp. 1347–1356, 2005.

23. Moré, M. J., Goodale, P. J., Majewski, S., and Williams, M. B., "Evaluation of gamma cameras for use in dedicated breast imaging," *IEEE Transactions on Nuclear Science,* Vol. 53(5), pp. 2675–2679, 2006.

24. Hruska, C.B., and O'Connor, M. K., "Effect of Collimator Selection on Tumor Detection for Dedicated Nuclear Breast Imaging Systems," *IEEE Transactions on Nuclear Science,* Vol. 53(5), pp. 2680–2689, 2006.

25. Ciatto, S., Turco, M. R. D., and Bravetti, P., "Nonpalpable breast lesions: stereotaxic fine-needle aspiration cytology," *Radiology,* Vol. 173(1), pp. 57–59, 1989.

26. Fajardo, L. L., Davis, J. R., Wiens, J. L., and Trego, D. C., "Mammography-guided stereotactic fine-needle aspiration cytology of nonpalpable breast lesions: prospective comparison with surgical biopsy results," *AJR Am J Roentgenol,* Vol. 155(5), pp. 977–981, 1990.

27. Tulusan, A.H., "Mammographic-pathological correlations," *Friedrich, M., Sickles, E. A., eds. Radiological diagnosis of breast diseases*, pp. 13–32, Berlin Heidelberg New York: Springer, 1997.

28. Schreer, I., and Frischbier, J., "Breast cancer screening projects: results," *Friedrich, M., Sickles, E. A., eds. Radiological diagnosis of breast diseases*, pp. 333–346, Berlin Heidelberg New York: Springer; 1997.

29. Teubner, J., "Echomammography: technique and results," *Friedrich, M., Sickles, E. A., eds. Radiological diagnosis of breast diseases*, pp.181–220, 1997.

30. Bauer, M., Tontsch, P., and Schulz-Wendtland, R., "Fine-needle aspiration and core biopsy," *Friedrich, M., Sickles, E. A., eds. Radiological diagnosis of breast diseases*, pp. 291–298, Berlin Heidelberg New York: Springer, 1997.

31. Oestmann, JW., "Digital mammography," *Friedrich, M., Sickles, E. A., eds. Radiological diagnosis of breast diseases*, Berlin Heidelberg New York: Springer, pp. 65–74, 1997.

32. Heywang-Kobrunner, S. H., and Beck, R., "Clinical application of contrast- enhanced MRI," *eds. Contrast-enhanced MRI of the breast,* Berlin Heidelberg New York: Springer, pp. 157–204, 1996.

33. Bombardieri, E., Crippa, F., Maffioli, L., and Greco, M., "Nuclear medicine techniques for the study of breast cancer," *Eur J Nucl Med*, Vol. 24(7), pp. 809–824, 1997.

34. Fajardo, L. L., "Screening Mammography," *Imaging Decisions MRI,* Vol. 9(2), pp. 23–34, 2005.

35. Den Outer, A. J., Pauwels, E. K., Zwavelig, A., Puylaert, J. B., Hermans, J., and De Lange, E. E., "Breast scintigraphy with 99mTc diethylene triamine penta-acetic acid for the detection of malignant diseases," Br J Surgery, Vol. 73, pp. 613–614, 1986.

36. Schillaci, O., and Buscombe, J. R., "Breast scintigraphy today: indications and limitations," *Eur J Nucl Med Mol Imaging,* Vol. 31, pp.35–45, 2004.

37. Mankoff, D. A., Dunnwald, L. K., and Kinahan, P., "Are we ready for dedicated breast imaging approaches?," *J Nucl Med,* Vol. 44(4), pp. 594–595, 2003.

38. Brem, R. F., Schoonjans, J. M., Kieper, D. A., Majewski, S., Goodman, S., and Civelek, C., "High-resolution scintimammography: a pilot study," *J Nucl Med,* Vol. 43(7), pp. 909–91, 2002.

39. Gupta, P., Waxman, A., and Nguyen. K., et al., "Correlation of Tc-99m sestamibi uptake with histopathologic characteristics in patients with breast diseases [abstract]," *J Nucl Med,* Vol. 37, 250P, 1996.

40. Buscombe, J. R., Cwikla, J. B., Thakrar, D. S., and Hilson, A. J., "Scintigraphic imaging of breast cancer: a review," *Nucl Med Commun.,* Vol. 18(8), pp. 698–709, 1997.

41. Schillaci, O., and Scopinaro, F.,"Tc-99m sestamibi scintimammography: where is it now?," *Cancer Biother Radiopharm,* Vol. 14(6), pp. 417–422, 1999.

42. Schomäcker, K., and Schicha, H., "Use of myocardial imaging agents for tumour diagnosis--a success story?," *Eur J Nucl Med,* Vol. 27(12), pp. 1845–1863, 2000.

43. Maffioli, L., Steens, J., Pauwels, E., and Bombardieri, E., "Applications of 99mTc-sestamibi in oncology," *Tumori,* Vol. 82(1), pp. 12–21, 1996.

44. Carvalho, P. A., Chiu, M. L., Kronauge, J. F., Kawamura, M., Jones, A. G., Holman, B. L., and Piwnica-Worms, D., "Subcellular distribution and analysis of technetium-99m-MIBI in isolated perfused rat hearts," *J Nucl Med,* Vol. 33(8), pp. 1516–1522, 1992.

45. Delmon-Moingeon, L. I., Piwnica-Worms, D., den Abbeele, A. D. V., Holman, B. L., Davison, A., and Jones, A. G., "Uptake of the cation hexakis(2-methoxyisobutylisonitrile)-technetium-99m by human carcinoma cell lines in vitro," *Cancer Res,* Vol. 50(7), pp. 2198–2202, 1990.

46. Maublant, J. C., Zhang, Z., Rapp, M., Ollier, M., Michelot, and J., Veyre, A., "In vitro uptake of technetium-99m-teboroxime in carcinoma cell lines and normal cells: comparison with technetium-99m-sestamibi and thallium-201," *J Nucl Med,* Vol. 34(11), pp. 1949–1952, 1993.

47. Scopinaro, F., Schillaci, O., Scarpini, M., Mingazzini, P. L., Macio, L. D., Banci, M., Danieli, R., Zerilli, M., Limiti, M. R., and Colella, A. C., "Technetium-99m sestamibi: an indicator of breast cancer invasiveness," *Eur J Nucl Med.,* Vol. 21(9), pp. 984–987, 1994.

48. Piwnica-Worms, D., Chiu, M. L., Budding, M., Kronauge, J. F., Kramer, R. A., and Croop, J. M., "Functional imaging of multidrug-resistant P-glycoprotein with an organotechnetium complex," *Cancer Res.,* Vol. 53(5), pp. 977–984, 1993.

49. Arbab, A. S., Koizumi, K., Toyama, K., and Araki, T., "Uptake of technetium-99m-tetrofosmin, technetium-99m-MIBI and thallium-201 in tumor cell lines," *J Nucl Med.,* Vol. 37(9), pp. 1551–1556, 1996.

50. Ballinger, J. R., "99mTc-tetrofosmin for functional imaging of P-glycoprotein modulation in vivo," *J Clin Pharmacol Suppl*, pp. 39–47, 2001.

51. de Wiele, C. V., Rottey, S., Goethals, I., Buscombe, J., Belle, S. V., Vos, F. D., and Dierckx, R. A., "99mTc sestamibi and 99mTc tetrofosmin scintigraphy for predicting resistance to chemotherapy: a critical review of clinical data," *Nucl Med Commun,* Vol. 24(9), pp. 945–950, 2003.

52. Waxman, A. D., Ramanna, L., Memsic, L. D., Foster, C. E., Silberman, A. W., Gleischman, S. H., Brenner, R. J., Brachman, M. B., Kuhar, C. J., and Yadegar, J., "Thallium scintigraphy in the evaluation of mass abnormalities of the breast," *J Nucl Med,* Vol. 34(1), pp.18–23, 1993.

53. Scopinaro, F., Schillaci, O., Ussof, W., Nordling, K., Capoferro, R., Vincentis, G. D., Danieli, R., Ierardi, M., Picardi, V., Tavolaro, R., and Colella, A. C., "A three center study on the diagnostic accuracy of 99mTc-MIBI scintimammography," *Anticancer Res.* Vol. 17(3B), pp.1631–1634, 1997.

54. Lumachi, F., Ferretti, G., Povolato, M., Marzola, M. C., Zucchetta, P., Geatti, O., Bui, F., and Brandes, A. A., "Sestamibi scintimammography in pT1 breast cancer: alternative or

complementary to X-ray mammography?," *Anticancer Res,* Vol. 21(3C), pp. 2201–2205, 2001.

55. Bender, H., Kirst, J., Palmedo, H., Schomburg, A., Wagner, U., Ruhlmann, J., Biersack, and H. J., "Value of 18fluoro-deoxyglucose positron emission tomography in the staging of recurrent breast carcinoma," *Anticancer Res,* Vol. 17(3B), pp. 1687–1692, 1997.

56. Khalkhali, I., Villanueva-Meyer, J., Edell, S. L., Connolly, J. L., Schnitt, S. J., Baum, J. K., Houlihan, M. J., Jenkins, R. M., and Haber, S. B., "Diagnostic accuracy of 99mTc-sestamibi breast imaging: multicenter trial results," *J Nucl Med,* Vol. 41(12), pp. 1973–1979, 2000.

57. Murray, A. D., and Brooks, M. E., "Nuclear medicine in oncology," *J R Coll Surg Edinb,* Vol. 45(2), pp. 110–119, 2000.

58. Khalkhali, I., Cutrone, J. A., Mena, I. G., Diggles, L. E., Venegas, R. J., Vargas, H. I., Jackson, B. L., Khalkhali, S., Moss, J. F., and Klein, S. R., "Scintimammography: the complementary role of Tc-99m sestamibi prone breast imaging for the diagnosis of breast carcinoma,", *Radiology,* Vol. 196(2), pp. 421–426, 1995.

59. Burak, Z., Argon, M., Memis, A., Erdem, S., Balkan, Z., Duman, Y., Ustün, E. E., Erhan, Y., and Ozkiliç, H., "Evaluation of palpable breast masses with 99Tcm-MIBI: a comparative study with mammography and ultrasonography," *Nucl Med Commun,* Vol. 15(8), pp. 604–612, 1994.

60. Taillefer, R., Robidoux, A., Lambert, R., Turpin, S., and Laperrière, J., "Technetium-99m-sestamibi prone scintimammography to detect primary breast cancer and axillary lymph node involvement," *J Nucl Med,* Vol. 36(10), pp. 1758–1765, 1995.

61. Lam, W. W., Yang, W. T., Chan, Y. L., Stewart, I. E., Metreweli, C., and King, W., "Detection of axillary lymph node metastases in breast carcinoma by technetium-99m sestamibi breast scintigraphy, ultrasound and conventional mammography," *Eur J Nucl Med,* Vol. 23(5), pp. 498–503, 1996.

62. Schillaci, O., "Is there a clinical role for scintimammography in breast cancer diagnosis?," *J Nucl Med,* Vol. 46(10), pp. 1571–1573, 2005.

63. Khalkhali, I., Baum, J. K., Villanueva-Meyer, J., Edell, S. L., Hanelin, L. G., Lugo, C. E., Taillefer, R., Freeman, L. M., Neal, C. E., Scheff, A. M., Connolly, J. L., Schnitt, S. J., Houlihan, M. J., Sampalis, J. S., and Haber, S. B., "(99m)Tc sestamibi breast imaging for the examination of patients with dense and fatty breasts: multicenter study," *Radiology,* Vol. 222(1), pp. 149–155, 2002.

64. Schillaci, O., and Buscombe, J. R., "Breast scintigraphy today: indications and limitations," *Eur J Nucl Med Mol Imaging,* Vol. 31, pp. 35–45, 2004.

65. Cwikla, J. B., Buscombe, J. R., Holloway, B., Parbhoo, S. P., Davidson, T., McDermott, N., and Hilson, A. J., "Can scintimammography with (99m)Tc-MIBI identify multifocal and multicentric primary breast cancer?," *Nucl Med Commun,* Vol. 22(12), pp. 1287–1293, 2001.

66. Vargas, H. I., Agbunag, R. V., Kalinowski, A., Tolmos, J., Klein, S. R., Diggles, L., and Khalkhali, I., "The clinical utility of Tc-99m sestamibi scintimammography in detecting multicentric breast cancer," *Am Surg,* Vol. 67(12), pp. 1204–1208, 2001.

67. Mezi, S., Primi, F., Capoccetti, F., Scopinaro, F., Modesti, M., and Schillaci, O., "In vivo detection of resistance to anthracycline based neoadjuvant chemotherapy in locally advanced and inflammatory breast cancer with technetium-99m sestamibi scintimammography," *Int J Oncol,* Vol. 22(6), pp. 1233–1240, 2003.

68. Schillaci, O., Danieli, R., Romano, P., Cossu, E., and Simonetti, G., "Clinical utility of scintimammography: From the Anger-camera to new dedicated devices," *Nuclear Instruments and Methods in Physics Research*, Vol. 569, pp. 281–285, 2006.

69. Khalkhali, I., Cutrone, I., Mena, I., Diggles, L., Khalkhali, S., Venegas, R., and Klein, S., "The usefulness of scintimammography in patients with dense breast on mammogram [abstract]," *J Nucl Med,* Vol. 36, 52P, 1995.

70. Khalkhali, I., Mena, I., and Diggles, L., "Review of imaging techniques for the diagnosis of breast cancer: a new role of prone scintimammography using technetium-99m sestamibi," *Eur J Nucl Med,* Vol. 21(4), pp. 357–362, 1994.

71. Andersson, I., Aspegren, K., Janzon, L., Landberg, T., Lindholm, K., Linell, F., Ljungberg, O., Ranstam, J., and Sigfússon, B., "Mammographic screening and mortality from breast cancer: the Malmö mammographic screening trial," *BMJ,* Vol. 297(6654), pp. 943–948, 1988.

72. Bombardieri, E., Aktolun, C., Baum, R. P., Bishof-Delaloye, A., Buscombe, J., Chatal, J. F., Maffioli, L., Moncayo, R., Mortelmans, L., and Reske, S. N., "Breast scintigraphy: procedure guidelines for tumour imaging," *Eur J Nucl Med Mol Imaging,* Vol. 30(12), pp. 107–114, 2003.

73. Cherry, S. R., Sorenson, J. A., and Phelps, M. E., *Physics in Nuclear Medicine,* Philadelphia, PA: Saunders, 3rd ed., 2003.

74. Mettler, F. A., and Guiberteau, M. J., *Essentials of Nuclear Medicine Imaging*, Philadelphia: Saunders, 4th ed., 1998.

75. Sprawls, P., *Physical Principles of Medical Imaging*, Rockville, Md.: Aspen Publishers, 1987.

76. Yilmaz, O., "Virtual gamma camera for educational purposes," Master's thesis, Bogazici University, Istanbul, Turkey, 2003.

77. Zaidi, H., "Relevance of accurate Monte Carlo modeling in nuclear medical imaging," *Med Phys,* Vol. 26(4), pp. 574–608, 1999.

78. Zaidi, H., "Monte Carlo techniques in diagnostic and therapeutic nuclear medicine," in *Standards and Codes of Practice in Medical Radiation Dosimetry*, Vol. 2, pp. 29–44, International Vienna: International Atomic Energy Agency Symposium, 2002.

79. Andreo, P., "Monte Carlo techniques in medical radiation physics," *Phys Med Biol,* Vol. 36(7), pp. 861–920, 1991.

80. Pllana S., "History of Monte Carlo Method",
Available: http://www.geocities.com/CollegePark/Quad/2435/history.html

81. Morin, R. L., *Monte Carlo Simulation in the Radiological Sciences*, Boca Raton, Fla.: CRC Press, 1988, pp. 54–55

82. Ho, S., "Introduction to Monte Carlo,"
Available: www.astro.princeton.edu/~gk/A542/shirley.pdf

83. Marsaglia, G., and Zaman. A., ''Some portable very-long-period random number generators,'' *Comput. Phys.,* Vol. 8, pp. 117–121, 1994.

84. Vattulainen, I., Kankaala, K., Saarinen, J., and Ala-Nissila, T., ''A comparative study of some pseudorandom number generators,'' *Comput. Phys. Commun.,* Vol. 86, pp. 209–226, 1995.

85. Lehmer, D. H.,''Mathematical methods in large-scale computing units,'' in *Proceedings of the 2nd Symposium on Large-Scale Digital Calculating Machinery*, pp. 141–146, Cambridge, 1949.

86. Knuth, D. E., *The Art of Computer Programming, Vol. 2: Seminumerical Algorithms*, Massachusetts: Addison-Wesley, 2nd ed., 1997.

87. Press, W. H., *Numerical Recipes in C, The Art of Scientific Computing*, Cambridge: University Press, 1992

88. Marsaglia, G., and Zaman. A., ''Some portable very-long-period random number generators,'' *Comput. Phys.,* Vol. 8, pp. 117–121, 1994.

89. Mascagni, M., Cuccaro, S. A., Pryor, D. V., and Robinson, M. L., ''A fast, high-quality, and reproducible lagged-Fibonacci pseudorandom number generator,'' *J. Comput. Phys.,* Vol. 15, pp. 211–219, 1995.

90. Brent R. P., ''On the periods of generalized Fibonacci recurrences,'' *Math. Comput.,* Vol. 63, pp. 389–401, 1994.

91. Ljunberg, M., Strand S. E., and King M. A., *Monte Carlo Calculations in Nuclear Medicine: Applications in Diagnostic Imaging*, Philadelphia: Institute of Physics Pub., 1998.

92. Kahn, H., "Use of different Monte Carlo sampling techniques,'' *in Monte Carlo Methods, edited by H. A. Meyer*, New York: Wiley, 1956.

93. Bielajew, A. F., and Rogers, D. W. O., ''Variance-reduction techniques,'' *in Monte Carlo Transport of Electrons and Photons, edited by Jenkins, T., Nelson,W., Rindi, A., Nahum, A., Rogers, D.,* pp. 407–419, New York: Plenum, 1989.

94. Haynor, D. R., Harrison, R. L., and Lewellen, T. K., ''Improving the efficiency of emission tomography using variance reduction techniques,'' *IEEE Trans. Nucl. Sci.,* Vol. 37, pp. 749–753, 1990.

95. Zubal, I. G., and Harell, C. R., ''Voxel-based Monte Carlo calculations of nuclear medicine images and applied variance reduction techniques,'' *Image Vis. Comput.,* Vol. 10, pp. 342–348, 1992.

96. Haynor, D. R., Harrison, R. L., and Lewellen, T. K., ‘‘The use of importance sampling techniques to improve the efficiency of photon tracking in emission tomography simulations,’’ *Med. Phys.,* Vol. 18, pp. 990–1001, 1991.

97. Zaidi, H., Scheurer, and A. H., Morel, C., “An object-oriented Monte Carlo simulator for 3D cylindrical positron tomographs,” *Comput. Methods Programs Biomed.,* Vol. 58, pp. 133–145, 1999.

98. Hahn, L. J., Jaszczak, R. J., Gullberg, G. T., Floyd, C. E., Manglos, S. H., Greer, K. L., and Coleman, R. E., ‘‘Noise characteristics for cone beam collimators: a comparison with parallel hole collimator,’’ *Phys. Med. Biol.,* Vol. 33, pp. 541–555, 1988.

99. Dye, R. E. A., ‘‘Simulation of clinical scitingrams for nuclear medicine imaging devices,’’ *Phys. Med. Biol.,* Vol. 33, pp. 1329–1334, 1988.

100. Gantet, P., Esquerré, J. P., Danet, B., and Guiraud, R., “A simulation method for studying scintillation camera collimators,” *Phys Med Biol,* Vol. 35(5), pp. 659–669, 1990.

101. Rosenthal, M. S., Cullom, J., Hawkins, W., Moore, S. C., Tsui, B. M., and Yester, M., “Quantitative SPECT imaging: a review and recommendations by the Focus Committee of the Society of Nuclear Medicine Computer and Instrumentation Council,” *J Nucl Med,* Vol. 36(8), pp. 1489–1513, 1995.

102. Zaidi, H., ‘‘Quantitative SPECT: Recent developments in detector response, attenuation and scatter correction techniques,’’ Phys. Medica, Vol. 12, pp. 101–117, 1996.

103. Floyd, C. E., Jaszczak, R. J., and Coleman, R. E., “Scatter detection in SPECT imaging: dependence on source depth, energy, and energy window,” *Phys Med Biol,* Vol. 33(9), 1075–1081, 1988.

104. Lowry, C. A., and Cooper, M. J., “The problem of Compton scattering in emission tomography: a measurement of its spatial distribution,” *Phys Med Biol,* Vol. 32(9), pp. 1187–1191, 1987.

105. Kojima, A., Matsumoto, M., Takahashi, M., and Uehara, S., “Effect of energy resolution on scatter fraction in scintigraphic imaging: Monte Carlo study,” *Med Phys,* Vol. 20(4), pp. 1107–1113, 1993.

106. Andreo, P., “Monte Carlo techniques in medical radiation physics,” *Phys Med Biol,* Vol. 36(7), pp.861–920, 1991.

107. Berger, M. J., ‘‘MIRD pamphlet 2: energy deposition in water by photons from point isotropic sources,’’ J. Nucl. Med., Vol. 9, pp. 15–25, 1968.

108. Berger, M. J., ‘‘MIRD pamphlet 7: distribution of absorbed doses around point sources of electrons and beta particles in water and other media,’’ J. Nucl. Med., Vol. 12, pp. 5–23, 1971.

109. Snyder, W., Ford, M. R., and Warner, G., ‘‘Estimates of specific absorbed fractions for photon sources uniformly distributed in various organs of a heterogeneous phantom,” *in NM/MIRD Pamphlet No. 5*, New York: Society of Nuclear Medicine Publication, 1978.

110. Wang, H., Jaszczak, R. J., and Coleman, R. E., ‘‘Solid geometry-based object model for Monte Carlo simulated emission and transmission tomographic imaging systems,’’ *IEEE Trans. Med. Imaging,* Vol. 11, pp. 361–372, 1992.

111. Wang, H., Jaszczak, R. J., and Coleman, R. E., “A new composite model of objects for Monte Carlo simulation of radiological imaging,” *Phys Med Biol,* Vol. 38(9), pp. 1235–1262, 1993.

112 Nelson, W. R., Hirayama, H., Rogers, D. W. O., ‘‘The EGS4 code system,’’ *in SLAC-256*, Stanford, CA: Stanford Linear Accelerator Center, 1985.

113. Halbleib, J. A., Kensek, R. P., Valdez, G. D., Seltzer, S. M., and Berger, M. J., ‘‘ITS: The Integrated TIGER Series of electron/photon transport codes—version 3.0,’’ IEEE Trans. Nucl. Sci., Vol. 39, pp. 1025–1030, 1992.

114. Briesmeister, J. F., ‘‘MCNP—A general Monte Carlo code for neutron and photon transport,’’ Version 3A, Los Alamos, NM, Los Alamos National Laboratory, LA-12625-M, 1997.

115. Brun, R., Bruyant, F., Maire, M., McPherson, A. C., and Zanarini, P., "GEANT 3", CERN DD/EE/84–1, 1987.

116. Harrison, R. L., Vannoy, S. D., Haynor, D. R., Gillispie, S. B., Kaplan, M. S., and Lewellen, T. K., *Preliminary experience with the photon history generator module for a public-domain simulation system for emission tomography,* pp. 1154–1158, New York: IEEE, , 1994.

117. Ljungberg, M., and Strand, S. E., “A Monte Carlo program for the simulation of scintillation camera characteristics,” *Comput Methods Programs Biomed,* Vol. 29(4), pp. 257–272, 1989.

118. Yanch, J. C., and Dobrzeniecki, A. B., ‘‘Monte Carlo simulation in SPECT: Complete 3-D modeling of source, collimator and tomographic data acquisition,’’ IEEE Trans. Nucl. Sci., Vol. 40, pp. 198–203, 1993.

119. Smith, M. F., Floyd, C. E., and Jaszczak, R. J., “A vectorized Monte Carlo code for modeling photon transport in SPECT,” *Med Phys,* Vol. 20(4), pp. 1121–1127, 1993.

120. Thompson, C. J., Moreno-Cantu, J., and Picard, Y., “PETSIM: Monte Carlo simulation of all sensitivity and resolution parameters of cylindrical positron imaging systems,” *Phys Med Biol,* Vol. 37(3), pp. 731–749, 1992.

121. Zaidi, H., Scheurer, A. H., and Morel, C., “An object-oriented Monte Carlo simulator for 3D cylindrical positron tomographs,” *Comput Methods Programs Biomed,* Vol. 58(2), pp. 133–145, 1999.

122. Kimiaei, S., Ljungberg, M., and Larsson, S. A., “Evaluation of optimally designed planar-concave collimators in single-photon emission tomography,” *Eur J Nucl Med,* Vol. 24(11), pp. 1398–1404, 1997.

123. Box, G. E. P., and Wilson, K.B., “On the Experimental Attainment of Optimum Conditions (with discussion),” *Journal of the Royal Statistical Society Series B,* Vol. 13(1), pp. 1–45, 1951.

124. Myers R.H., and Montgomery D.C., *Response Surface Methodology Process and Product Optimization Using Designed Experiments*, Wiley-Interscience, 2nd ed., 2002

125. Dependent and independent variables,
Available: http://en.wikipedia.org/wiki/Dependent_and_independent_variables

126. Box, G. E., Hunter, W. G., Hunter, J. S., and Hunter,W. G., *Statistics for Experimenters: Design, Innovation, and Discovery*, Wiley, 2nd ed., 2005.

127. Response Surface Designs, Statistics Toolbox Documentation, The Mathworks Available: http://www.mathworks.com/access/helpdesk/help/helpdesk.html

128. Box, G. E. P., and Draper, N. R., *Empirical Model Building and Response Surfaces*, New York: John Wiley & Sons, 1987

129. Montgomery, D. C., Design and analysis of experiments, New York: Wiley, 1976

130. Taguchi, G., and Wu. Y., *Introduction to offline quality control*, Nagoya, Japan: Central Japan Quality Association, 1980.

131. Taguchi, G., *Introduction to Quality Engineering*, White Plains, New York: UNIPUB/Krauss International, 1986.

132. Taylor, W.A., *Methods and Tools for Process Validation*, Taylor Enterprises, Inc., 1998.

133. Whitcomb, P.J., and Anderson, M.J., "Robust Design-Reducing Transmitted Variation: Finding the Plateaus via Response Surface Methods," Quality Congress, ASQC, 1996.

134. Helseth, T., et al., Design-Expert® Software, Stat-Ease Corporation, 1994.

135. Maublant, J., de Latour, M., Mestas, D., Clemenson, A., Charrier, S., Feillel, V., Bouedec, G. L., Kaufmann, P., Dauplat, J., and Veyre, A., "Technetium-99m-sestamibi uptake in breast tumor and associated lymph nodes," *J Nucl Med* , Vol. 37(6), pp. 922–925, 1996.

136. Boone, J. M., Nelson, T. R., Lindfors, K. K., and Seibert, J. A., "Dedicated breast CT: radiation dose and image quality evaluation," *Radiology,* Vol. 221, pp. 657–667, 2001.

137. Scopinaro, F., Pani, R., Vincentis, G. D., Soluri, A., Pellegrini, R., and Porfiri, L. M., "High-resolution scintimammography improves the accuracy of technetium-99m methoxyisobutylisonitrile scintimammography: use of a new dedicated gamma camera," *Eur J Nucl Med,* Vol. 26(10), pp. 1279–1288, 1999.

138. Brem, R. F., Schoonjans, J. M., Kieper, D. A., Majewski, S., Goodman, S., and Civelek, C., "High-resolution scintimammography: a pilot study," *J Nucl Med,* Vol. 43(7), pp. 909–915, 2002.

139. Rosen, E. L., Turkington, T. G., Soo, M. S., Baker, J. A., and Coleman, R. E., "Detection of primary breast carcinoma with a dedicated, large-field-of-view FDG PET mammography device: initial experience," *Radiology,* Vol. 234(2), pp. 527–534, 2005.

140. Bilgin, B., "Optimal collimator design using Monte Carlo Simulation and RSM for breast scintigraphy," Master's thesis, Bogazici University, Istanbul, Turkey, 2006.

141. Ljungberg, M., The SIMIND Monte Carlo Program Manual, Available: http://www.radfys.lu.se/simind/Manual.html